VILNIUS UNIVERSITY

CENTER FOR PHYSICAL SCIENCES
AND TECHNOLOGY

Aleksandr Alesenkov

MICROMACHINING OF NONTRANSPARENT MATERIALS IN AIR AND WATER WITH FEMTOSECOND LASER PULSES

Doctoral dissertation

Technological Sciences, Material Engineering (08T)

Vilnius, 2016

Research performed in 2011 - 2016 at Vilnius University.

Scientific supervisor:

Prof. Habil. Dr. Valdas Sirutkaitis

(Vilnius University, Technological Sciences, Material Engineering - 08T)

VILNIAUS UNIVERSITETAS

FIZINIŲ IR TECHNOLOGIJOS MOKSLŲ CENTRAS

Aleksandr Alesenkov

NESKAIDRIŲ MEDŽIAGŲ MIKROAPDIRBIMAS ORE IR VANDENYJE FEMTOSEKUNDINIAIS LAZERINIAIS IMPULSAIS

Daktaro disertacija

Technologijos mokslai, Medžiagų inžinerija (08T)

Vilnius, 2016

Disertacija rengta 2011 - 2016 metais Vilniaus Universitete.

Mokslinis vadovas:

Prof. Habil. Dr. Valdas Sirutkaitis (Vilniaus universitetas, Technologijos mokslai, Medžiagų inžinerija - 08T)

Padėka

Noriu nuoširdžiai padėkoti žmonėms, be kurių pagalbos ši disertacija negalėjo būti pabaigta:

- ❖ Prof. Valdui Sirutkaičiui už visapusišką nuoširdžią pagalbą, vadovavimą, idėjas, didelę kantrybę, paramą, gerą ir stiprų gyvenimo pavyzdį. Kartu noriu pasidžiaugti jo sukurtomis, puikiomis darbo sąlygomis ir suburtu nuostabiu Lazerinių tyrimų centro kolektyvu.
- ❖ Recenzentams Dr. Gediminui Račiukaičiui ir Prof. Roaldui Gadonui už geležinius nervus ir kantrybę, taisant darbą, ir begalę pastabų, kurios visos padėjo jį tobulinti.
- ❖ Dokt. Simui Butkui už pagalbą eksperimentuose su vandeniu ir optimizavimu.
- ❖ Dr. Domui Paipului ir Dr. Andriui Melninkaičiui už didelę pagalbą, rašant straipsnius, duotus vertingus patarimus.
- ❖ Dr. Mangirdui Malinauskui ir Dr. Vytautui Purliui už galimybę naudotis surinkta 4f sistema.
- ❖ Dr. Eugenijui Gaižauskui už pagalbą, atliekant teorinį modeliavimą bei pokalbius apie Putiną.
- ❖ Dr. Onai Balachninaitei už palaikymą bei pagalbą, ruošiant literatūros apžvalgą.
- ❖ Visiems tikrinusiems ir taisiusiems lietuvių ir ypač anglų kalbos gramatines ir stiliaus klaidas. Be jūsų redakcinių pastabų bei pagalbos aprašai būtų žymiai prastesnės kokybės.
- ❖ Visam FF VU kvantinės elektronikos katedros kolektyvui, su kuriuo turėjau privilegiją dirbti ir mokytis.
- ❖ LMT fondui, parėmusiam mano vykdytus tyrimus.
- ❖ O svarbiausia, mano Viešpačiui Jėzui Kristui už dvasinę paramą ir mano šeimai šiuo ilgu ir nelengvu disertacijos rašymo metu: mylimai žmonai Marinai, 3 metukų sūnui Viefiliui už tai, kad prieš miegą skatindavo ir įkvėpdavo eiti rašyti, klausdamas: - Tu, tėti, jau parašei disertaciją? Bei mūsų mažyliui, kad neleisdavo užmigti berašant.

Nuoširdžiai dėkoju Jums visiems!

<div align="right">

Aleksandr Alesenkov

Vilnius, 2016

</div>

List of the Abbreviations

AFM	-	atomic force microscopy
AR	-	antireflection
ASE	-	amplified spontaneous emission
CCD	-	charge coupled device
CPA	-	chirped pulse amplification
DC	-	direct current
DLA	-	direct laser ablation
DOE	-	diffractive optical element
DPSS	-	diode pumped solid-state
EDS	-	energy-dispersive x-ray spectroscopy
EFI	-	electric field intensity
Yb:KGW	-	Ytterbium doped Potassium-Gadolinium Tungstate
EM	-	electromagnetic
FPF	-	femtosecond pulse generated light filaments
fs	-	femtosecond (10^{-15} s)
F_{thr}	-	ablation threshold fluence
GRIN	-	gradient-index
GUI	-	guided user interface
HAZ	-	heat affected zone
HG	-	harmonic generation
HR	-	high reflectivity
HT	-	hat top
IDOE	-	intelligent design of experiment
n_2	.	Kerr index of refraction
NPs	-	nanoparticles
NA	-	numerical aperture
ns	-	nanosecond (10^{-9} s)
OPA	-	optical parametric amplifier
ps	-	picosecond (10^{-12} s)
RMS	-	root mean square
SHG	-	second harmonic generation
WYSIWYG	-	an acronym for "what you see is what you get"
XRD	-	x-ray diffraction

Table of content

Introduction

Material processing such as laser cutting is one of the promising potential applications of femtosecond lasers in an industrial context. Femtosecond-laser material microprocessing based on ablation has a universal character. Nearly arbitrary micrometre-size patterns and structures can be fabricated [1-5]. Laser ablation because of its non-contact nature, allows micromachining and surface patterning of materials with minimal mechanical and thermal deformation. It is now well known that the femtosecond regime offers advantages over the nanosecond and picosecond regimes for many of its applications. The advantages lie in its ability to deposit energy into a material in a very short time before thermal diffusion can occur. As a result, the heat-affected zone, where melting and solidification can occur is significantly reduced. Smaller feature sizes, greater spatial resolution, and better aspect ratios can, therefore, be achieved.

Although femtotechnology was still not mature at the beginning of 2010, it offered the possibility of presenting this microfabrication method for performing important operations in the wear sensor development and prototype production according to the FP7 project MesMesh. An important factor in starting this project was access in laboratories of Vilnius University to the Pharos laser, produced by the Lithuanian company Light Conversion. The international project proposal was to fill laser etched microgrooves in a steel mould with an insulating material containing inserted conducting ceramic fibre. Vilnius University had the specific task of developing laser-etching technology to machine the required grooves by femtosecond laser ablation as well as to microstructure ceramic fibre to be inserted. The fibre is electrically isolated from the steel substrate using a glassy component, alternatively by means of a buffer layer of aluminium oxide or titanium dioxide. Fig.1 shows the 3D model and the cross-section view of the steel substrate in which there are parallel grooves filled with an insulating material and a conductive fibre

(i.e. the x-y plane is parallel to the page). Dimensions for the grooves are in the range of 100 - 300 μm in width with an aspect ratio close to unity. The fabrication accuracy should be no worse than ±5 % from intended dimensions with better than 10° wall inclination angle and bottom roughness better than ±5 % of the depth. The dimensions of the conducting fibre are accordingly smaller, in the order of 50 - 200 μm with the same ±5 % fabrication accuracy to completely fit the groove and leave some space for the insulating layer.

Clearly, the modality of the sensing system introduces certain limits to the properties of the material to be used. To realize a reliable system, the conductive material must be chosen to (a) wear at a rate comparable to the steel and (b) have an electrical resistivity which is large enough to realize an easily measurable change in resistance (order of 100 Ω, when the surface is worn down by not more than 5 μm). As the steel, and hence the ceramic fibre is worn down, the cross-sectional area of the fibre decreases and its resistance should increase. It has been calculated that, in order to get a detectable change in resistance, the conductive ceramic materials have to possess a resistivity in the range 10^2 to 10^4 $\mu\Omega \cdot cm$. In addition, the buffer element (the yellow one in Fig. 1) has to possess a resistivity several orders of magnitudes larger ($> 10^{14}$ $\div 10^{15}$ $\mu\Omega \cdot cm$) in order to provide good insulation from the steel substrate.
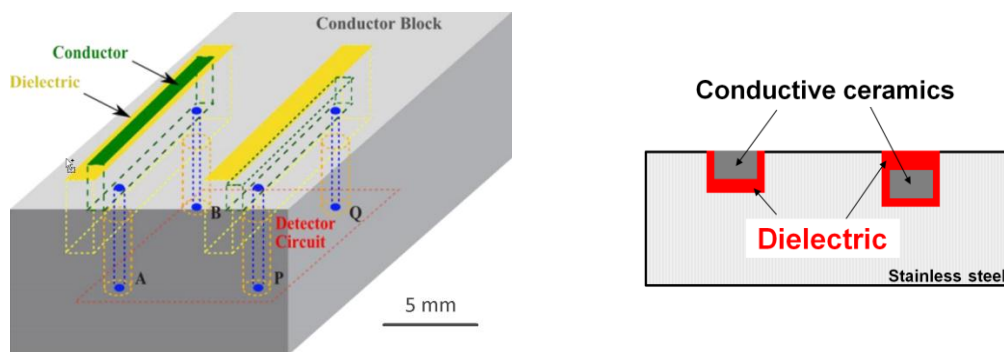
Fig. 1 The prototype of a resistive wear sensor consisting of a steel block with 2 conductive line sensors (measuring and reference) each in its slot. The top surface of the measuring sensor is coincident with the conductor block in which the device is mounted. Wear of the top surface of the structure reduces the sensor and surrounding block, changing the cross-section of the conducting line and therefore its electrical characteristics.

Today, there are no adequate means of measuring the surface damage done to steel surfaces in industrial machinery like driveshaft, gears, brake pads of turbines or wind generators, flanges for fixed drilling and grinding machines, dies for extrusion and moulds for injection moulding machines. It is nearly impossible or very difficult to determine when to change a part or perform maintenance. This results in enormous losses for the European community, due to machines breaking down and causing delays in production and delivery. The aim of the MesMesch project was the development of wear sensor for such surface damage measurements.

The required femtosecond laser processing operations for the wear sensor production were the groove ablation in steel and aluminium alloys, as well as the groove cutting and microhole drilling in conducting ceramic fibres. This project initiated research on these problems and was the initial basis for this dissertation. All femtosecond processing operations were at first only performed in atmospheric conditions. During the six years that this dissertation was being carried out, the femtosecond laser systems used in the experiments underwent considerable development, increasing in average power up to 20 W as well as in repetition rate up to 600 kHz with excellent efficiency and beam quality. In addition, ablation of transparent materials with filamented beams in water was introduced, and this expanded research on metallic materials also in liquids and with higher-average-power high-repetition-rate laser systems. Femtosecond micromachining is now becoming an emerging key technology for various microfabrication tasks.

Main objectives of the dissertation

The aim of the research was to develop micromachining technologies with ultrashort laser pulses for solid-state non-transparent materials that are necessary for wear sensor manufacturing:

a) microgroove of special form cutting in metals;

b) microhole drilling and notch cutting in conductive ceramics;

c) comparison of micromachining process and efficiency in air and water.

Dissertation practical tasks

1. Develop and optimize the micromachining system for non-transparent solid-state material microfabrication with linear direct-drive servomotors positioning stages and galvanometer scanner utilizing both "moving sample" and "moving beam" concepts.

2. Utilizing high-repetition-rate CPA femtosecond laser pulses perform unique microfabrication tasks on non-transparent solid-state materials (stainless steel, aluminium, titanium sub-oxide ceramics).

3. Fabricate functional wear sensor parts.

4. Conduct a research on femtosecond beam ablation of non-transparent solid-state materials in liquids.

During the implementation of these tasks unique experimental equipment was developed and necessary experiments including some process modelling were conducted.

Novelty

- It was experimentally verified that laser-ablation micromachining of small width grooves (width in the range of $30 - 300$ μm with an aspect ratio close to unity) could be optimized through the choice of appropriate laser beam scanning algorithms.

- The optimal parameter space was defined for the above-mentioned groove fabrication in stainless steel and aluminium by femtosecond pulse ablation.

- The optimal parameter space was defined for micromachining of notches (~120 μm width) and blind holes (~80 μm in diameter) in conductive titanium suboxide (Ti_4O_7) ceramics with femtosecond pulse ablation without the alteration of material conductivity.

- A filamented-beam ablation technique was adopted for non-transparent solid-state bulk materials, which considerably broadened the applicability of femtosecond ablation micromachining, up to several

times increasing the cutting speeds for and improving the quality of the process.

- It was shown that femtosecond micromachining could be successfully utilized for fabrication of wear-sensor parts.

Practical value

- Yb:KGW femtosecond laser with harmonic generators, 2 axis galvanometer laser beam scanner and 3D positioning system composed of linear stages, was adapted and optimized for micromachining non-transparent solid-state materials suitable for wear sensors.
- System control algorithms enabling the fabrication of different microstructures of required dimension, such as a groove, blind holes and different cuts were developed.
- Optimal femtosecond fabrication conditions for stainless steel, aluminium, titanium oxide and other light absorbing solid-state materials were determined.
- A unique wear sensor for *in situ* wear measurements of various interacting steel and aluminium parts was developed.
- The developed method for ablation of light absorbing solid-state materials in water shows its superior performance when cutting thick (>0.5 mm; <2.5 mm) metals and semiconductors as well as its quality, when thin metal films are being cut..

Statements for defence

1. Symmetrical 150 – 300 μm wide grooves in stainless steel and aluminium having a depth-to-width aspect ratio close to unity, better than ±5 % accuracy and walls steeper than 80° can be fabricated utilizing special symmetrical sample translation algorithm (spiral from lines) and optimizing the strong ablation regime in a micromachining system comprised of a high-repetition-rate (50 – 200 kHz) femtosecond laser and linear direct-drive servomotors stages for sample movements.

2. The use of a two-axis galvanometer scanner shortens the fabrication time for the ablation of rectangular 150 – 300 μm wide 5 cm long grooves in stainless steel by an order of magnitude, and the quality of the cuts could even be improved by using bidirectional and composite spiral scanning algorithms.

3. Selection of proper ablation parameters and the use of symmetrical scanning algorithm such as bidirectional spiral from lines provide the means for micromachining micronotches and blind microholes in titanium suboxide (Ti_4O_7) ceramics with dimensions in the range of 60 to 150 μm using high-repetition-rate femtosecond pulses without an electro-conductivity change in the material.

4. Optimized thickness (0.3 - 0.6 mm) of the water layer above the metallic materials provides higher efficiency of material removal, better cut quality and broader femtosecond laser ablation applicability for material samples up to 3 mm in thickness.

Approbation

The results of the research, presented in this dissertation, were published in one European Patent, five articles in journals from the ISI WoS list, four conference proceedings not from the ISI WoS list, and presented at seven international conferences.

Patents

[P1] European Patent EP2637014A1: J. Mueggler, Z. Kancleris, A. Galdikas, M. Yadav, H. Khiroya, A. Melninkaitis, V. Sirutkaitis, D. Paipulas, **A. Alesenkov**, O. Balachninaite, A.C.E. Dent, D. Reginonini, V. Adamaki, *Sensor system for monitoring wear* (2013).

Publication directly related to the topic of the dissertation (ISI WoS)

[A1] A. Baskevicius, **A. Alesenkov**, G. Chozevskis, J. Litvaityte, O. Balachninaite, D. Paipulas, A. Melninkaitis, V. Sirutkaitis, Optimization of Laser-Ablation Micromachining by Choice of Scanning Algorithms and Use of Laser-Induced-Breakdown Spectroscopy, J. Laser Micro/Nanoeng, **8** 24-29 (2013).

[A2] D. Paipulas, **A. Alesenkov**, D. Kaškelytė, G. Chaževskis, P. Ragulis, Z. Kancleris, V. Sirutkaitis, Femtosecond Micromachining of Ceramic Fibers for Electric Contact Soldering, J. Laser Micro/Nanoeng, **8** 304-308 (2013).

[A3] S. Butkus, E. Gaižauskas, D. Paipulas, Ž. Viburys, D. Kaškelyė, M. Barkauskas, **A. Alesenkov**, V. Sirutkaitis, Rapid microfabrication of transparent materials using filamented femtosecond laser pulses, Appl. Phys. A, **114** 81-90 (2014).

[A4] S. Butkus, **A. Alesenkov**, E. Gaižauskas, D. Paipulas, D. Kaškelytė, M. Barkauskas, V. Sirutkaitis, Analysis of the Micromachining Process of Dielectric and Metallic Substrates Immersed in Water with Femtosecond Pulses, Micromachines, **6** 2010-2022 (2015).

[A5] S. Butkus**, A. Alesenkov**, D. Paipulas, D. Kaškelytė, V. Sirutkaitis, Micromachining of Transparent, Semiconducting and Metal Substrates Using Femtosecond Laser Beams, J. Laser Micro/Nanoeng, **11** 81-86 (2016).

Publication directly related to the topic of the dissertation (Non-ISI WoS)

[A6] S. Butkus, D. Paipulas, Z. Viburys, A. Alesenkov, E. Gaizauskas, D. Kaskelyte, M. Barkauskas, V. Sirutkaitis, *Rapid Microfabrication of Transparent Materials Using a Filamented Beam of the IR Femtosecond Laser*, in: A. Heisterkamp, P.R. Herman, M. Meunier, S. Nolte (Eds.) *Frontiers in Ultrafast Optics: Biomedical, Scientific, and Industrial Applications Xiv*, 2014).

(Published international conference proceedings, on a basis of which A1, A2, A5 articles were written)

[A7] A. Baskevicius, **A. Alesenkov**, G. Chozevskis, J. Litvaityte, O. Balachninaite, D. Paipulas, A. Melninkaitis, V. Sirutkaitis, Optimization of laser-ablation micromachining by the choice of scanning algorithms and use of laser-induced-breakdown spectroscopy, Proc. of LPM (2012).

[A8] D. Paipulas, **A. Alesenkov**, D. Kaškelyė, G. Chaževskis, P. Ragulis, Ž. Kancleris, V. Sirutkaitis, Femtosecond micromachining of ceramic fibers for electric contact soldering, Proc. of LAMP (2013).

[A9] S. Butkus, **A. Alesenkov**, D. Paipulas, D. Kaškelyė, V. Sirutkaitis, Micromachining of Transparent, Semiconducting and Metal Substrates Using Femtosecond Laser Beams, Proc. of LAMP (2015).

Conference presentations directly related to the topic of the dissertation

[C1] <u>**A. Alesenkov**</u>, K. Kuršelis, *Micromachining of stainless steel with high repetition rate femtosecond laser pulses*, Laser Applications in Spectroscopy, Industry and Medicine, April 9-12, 2014, Riga, Latvia.

[C2] <u>D. Paipulas</u>, **A. Alesenkov**, K. Kuršelis, A. Melninkaitis, K. Stankevičiutė, O. Balachninaitė, V. Sirutkaitis, *Grooves formation in steel samples with high repetition rate femtosecond pulses*, 7th International Conference on Photo-Excited Processes and Applications, August 16-19, 2010 Copenhagen, Denmark.

[C3] A. Baskevicius, **A. Alesenkov**, G. Chozevskis, J. Litvaityte, O. Balachninaitė, D. Paipulas, A. Melninkaitis, <u>V. Sirutkaitis</u>, *Optimization of laser-ablation micromachining by choice of scanning algorithms and use of laser-induced-breakdown spectroscopy*, 13th International Symposium on Laser Precision Microfabrication (LPM2012), June 12-15, 2012, Washington DC, USA.

[C4] **A. Alesenkov**, L. Mažulė, G. Choževskis, <u>K. Stankevičiutė</u>, D. Paipulas, V. Sirutkaitis, *Microfabrication of notches for electric contacts in the conductive ceramic fiber by femtosecond pulses*, The Conference on Lasers and Electro-Optics/International Quantum Electronics Conference Europe (CLEOEurope/IQEC 2013), May 12-16, 2013 München, Germany.

[C5] <u>**A. Alesenkov**</u>, L. Mažulė, D. Kaškelyė, K. Stankevičiutė, V. Sirutkaitis, *Microincision of titanium dioxide ceramic fiber by femtosecond laser pulses*, 23rd Congress of the International Commission for Optics (ICO 23), August 26-29, 2014, Santiago de Compostela, Spain.

[C6] S. Butkus, **A. Alesenkov**, D. Paipulas, D. Kaškelyė, <u>V. Sirutkaitis</u>, *Micromachining of transparent, semiconducting and metal substrates using femtosecond laser beams*, The 7th International Congress on Laser Advanced Materials Processing (LAMP2015), May 26 – 29, 2015, Kitakyushu, Fukuoka, Japan.

[C7] S. Butkus, **A. Alesenkov**, D. Paipulas, <u>V. Sirutkaitis</u>, *Ablation of transparent and metallic materials immersed in water: process optimization and analysis*, 17th International Symposium on Laser Precision Microfabrication (LPM2016), May 23-27, 2016, Xi'an, China.

* presenting author is underlined.

Publication not directly related to the topic of the dissertation (ISI WoS)

[A10] **A. Alesenkov**, J. Pilipavičius, A. Beganskienė, R. Sirutkaitis, V. Sirutkaitis, Nonlinear properties of silver nanoparticles explored by a femtosecond Z-scan technique, Lith. J. Phys, **55** 100-109 (2015).

Conference presentations not directly related to the topic of this dissertation

[C8] <u>**A. Alesenkov**</u>, K. Steponkevičius, M. Malinauskas, V. Kudriašov, R. Sirutkaitis, V. Sirutkaitis, *Investigation of optical third-order nonlinearity of π-conjugated polymers with different Z-scan methods*

with femtosecond pulses, Northern Optics 2012 (NO2012), November 19 - 21 2012, Snekkersten, Denmark.

[C9] **A. Alesenkov**, M. Adomaitis, J. Pilipavičius, A. Beganskienė, V. Sirutkaitis, *Nanokompozitinių medžiagų netiesinių optinių savybių tyrimas plačiame spektro ruože z-skenavimo metodu su femtosekundiniais lazerio impulsais*, 40th Lithuanian National Conference of Physics 2013 (LNP2013), June 10-12, 2013, Vilnius, Lithuania.

[C10] **A. Alesenkov**, M. Adomaitis, J. Pilipavičius, A. Beganskienė, V. Sirutkaitis, *Linear and nonlinear properties of silver nanoprisms dispersed in water,* 23rd Congress of the International Commission for Optics (ICO23)*,* August 26-29, 2014 Santiago de Compostela, Spain.

[C11] **A. Alesenkov**, J. Pilipavičius, A. Beganskienė, O. Khazanov, V. Sirutkaitis, *Nonlinear properties of triangle silver nanoparticles explored with femtosecond Z-scan*, XVII International Conference Foundations & Advances in Nonlinear Science (FANS & ANPh 2014), September 29 - October 3, 2014, Minsk, Belorussia.

* presenting author is underlined.

Contributions

Author's contribution

All the investigations reported in this dissertation were carried out by the author during the years 2010 - 2016 in the laboratories of the Laser Research Centre of Vilnius University. Professor Valdas Sirutkaitis supervised the entire progress of the doctoral studies and contributed to every step of the preparation of this thesis. He greatly helped by the formulation of the aim, experiments planning, interpreting of the data and providing valuable ideas and advice. The author contribution included:

1. Development and assembly of the experimental setups including the micromachining systems for ablation in air with linear stages, with the

galvoscanner as well as adapting the micromachining system for ablation of metals and conducting ceramics under a thin liquid layer,

2. Experiment planning and realization,

3. Sample characterization after laser micromachining experiments including optical microscopy, scanning electron microscopy, optical confocal microscopy.

4. Experimental data analysis, writing of the parts of scientific publications related to my investigations and presentation of the results at conferences.

Co-authors contribution

- PhD student A. Baškevicius, student J. Litvaitytė, Dr. O. Balachninaitė worked on Laser-Induced-Breakdown Spectroscopy and its applications for micromachining optimization. This separate topic is included in joint publications but not included in this thesis.

- PhD student S. Butkus started the ablation experiments of transparent materials in liquids and water at Vilnius University, and this method was adopted by the author for the ablation of absorbing materials. In joint publications, the results on ablation experiments of transparent materials in liquids and water belong to S. Butkus and are not included in this thesis.

- Dr. D. Paipulas and Dr. A. Melninkaitis aided in planning, data statistical interpretation and organization of femtosecond ablation experiments in air and liquids.

- Dr. E. Gaižauskas provided scripts to perform numerical modelling of the fs beam propagation through the water layer and assisted to the results interpretation.

- Dr. D. Kaškelytė and Dr. M. Barkauskas acted as consultants for the technical aspects of the equipment and its optimization.

- Student G. Čaževskis took part in common experiments with the author on beam profile optimization for fs micromachining.

1. Review of femtosecond micromachining of metals and non-transparent materials

In this chapter of the dissertation, a brief review of the main femtosecond micromachining features of steel and conductive ceramics is presented. The optical and mechanical properties of those materials, as well as the basics of the ultrashort pulse interaction with matter, the influence of the laser and machining parameters on the process efficiency, are described.

1.1 Steel properties

Ferrous alloys are highly competitive due to their acceptable price and technological characteristics. They are listed as world's leading raw metals by annual consumption [1], thus illustrating the importance of iron. The class of iron alloys that is commonly referred to as steel represents the core of iron-based industry; they are the basis of machinery, tools, modern construction and many other areas, when steels are considered as a raw material for multipurpose fabrication, it becomes clear that this building matter rarely comes in the required shape and with the necessary surface properties right after production (founding). Methods of steel machining are used to give a workpiece final shape and finishing. However, due to tighter tolerance requirements for new application areas, conventional techniques may fail in particular cases, and laser ablation is one of the modern technologies that came to replace them. These new approaches mainly share the same idea – to replace the mechanical tooling (cutting, sawing, drilling, milling, grinding, polishing, honing, etc.) by different processing method. For example, this can be achieved electrochemically (etching, plating), directly electrically (discharge), by the multistage process (stamping/moulding). Although these competing technologies are readily available, they possess inherent drawbacks, thus motivating for the experimentation with the laser-based alternatives.

The key process in any type of material shaping, structuring, or machining is the change of its shape at the required scale and precision (e.g. from nanotexturing to saw-cutting). This is generally accomplished by two different approaches, namely (de)formation of solid or softened/molten raw material (moulding, stamping) or by material removal/deposition (milling, drilling, cutting, chemical deposition). The designation for the controllable structuring of micrometre-scale features in steel with the high precision in 2.5D makes photoetching [2] or deposition [3] based techniques scarcely feasible. On the other hand, due to the broadness and high flexibility of laser technology these constraints can be met by direct material removal [4, 5]. From the practical point of view, high-purity elemental metals are difficult and expensive to produce. However, it is a well-known fact that there exists a straightforward way to alter these properties by making various mixtures or to be more precise solid solutions by an embedment of one or more elements into the host metal.

As it is widely known, metals have a low number of electrons next to the outermost closed shell, which are referred to as valence electrons. These electrons are relatively weakly bound, and this results in metallic properties of such elements. One of them is the ability to form metallic bonding which is defined as a system of fixed metal ions and shared electron gas with freely moving constituents [6]. The balance between large radius ions repulsion and attraction through electron gas holds the system stable. Even more, this force ions to arrange themselves in specific patterns thus creating a crystal lattice.

Metallic bonding gives rise to a number of optical properties. In everyday life, metals are most notably distinguished by their highly reflective surface. This feature is also of great importance for various laser applications, ranging from metallic mirrors to laser machining as a characteristic defining how light is effected after reflection and how much energy is stored in the illuminated volume. As an illustration of typical metallic absorption-reflection behaviour, the main constituent of many steel alloys, namely iron, is given for

22

consideration in Fig. 1.1. Highly reflective metal properties at visible EM radiation range were successfully studied by Drude, who proposed a free electron model back in 1900 [7, 8]. This assumes a high number of free electrons present in the material, which leads to a further assumption that plasma absorption relations can be applied, written with further simplifications as follows:

$$\varepsilon_r = 1 - \frac{\varpi_p^2}{\varpi^2},$$ (1.1)

where ϖ is incident radiation frequency and plasma frequency ϖ_p is expressed as:

$$\varpi_p = \left(\frac{Ne^2}{\varepsilon_0 m_0} \right)^{\frac{1}{2}}.$$ (1.2)

Here, by knowing elementary constants such as electron mass m_0 and it's charge e together with the measured/calculated value of volumetric electron density N and dielectric constant ε_0, the relative dielectric constant may be evaluated and spectral reflectance determined. Thus, for the visible spectral region in the vicinity of 10^{15} Hz and plasma frequency lying in UV, high reflectivity should be observed, which is again visible in Fig. 1.1.
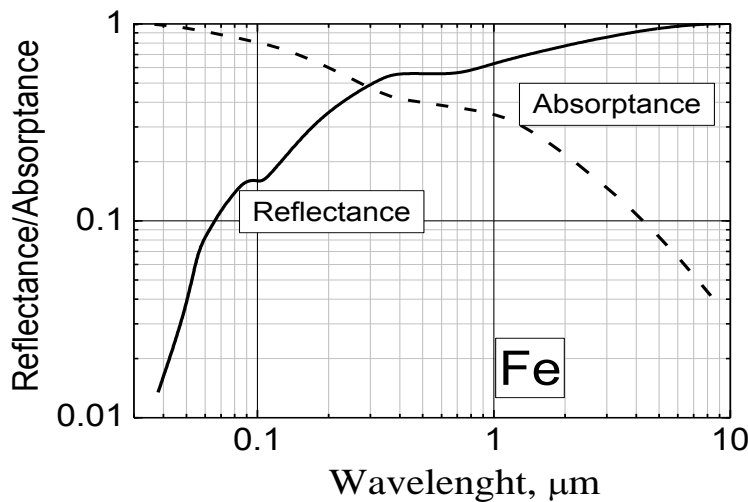
Fig. 1.1 Reflectance (R) and absorbtance (A) of iron [9].

Absorption causes the intensity of the light to decay with depth at a rate determined by the material's absorption coefficient a. In general, a is a

function of wavelength and temperature, but for constant a, intensity I decays exponentially with depth z according to the Beer–Lambert law $I = I_0 e^{-\alpha z}$, where I_0 is the intensity inside the surface after considering reflection loss. Optical penetration or absorption depth is defined as $\delta = \frac{1}{\alpha}$, which is the depth at which the intensity of the transmitted light drops to 1/e of its initial value at the interface. Due to the highly absorptive nature of metal-like materials (in compare with dielectric or isolator materials), initial irradiation energy deposition might occur only in a thin layer, also known as skin depth. Fig. 1.2 shows optical absorption depths as a function of wavelength for a variety of materials (aluminium, copper, gold, crystalline silicium, germanium, chromium and iron). In the case of most metals the depth is on the order of 10 nm.

Fig. 1.2 Optical absorption depths for several materials over a range of wavelength [10].
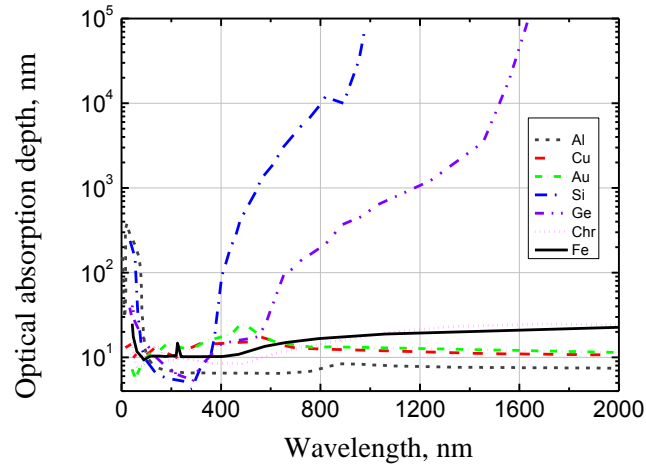
Multiscale texturing of a surface can cause significant deviations in how light is reflected and scattered, leading to enhanced absorption over that of a flat smooth surface. For surface features with dimensions greater than several wavelengths of light, this enhancement can most easily be described using the principles of ray optics. A portion from a ray of light will specularly reflect from a flat surface, as shown in Fig. 1.3a, and have no further interaction with the material. On the other hand, protruding features can reflect and scatter light back onto the surface, as seen in Fig. 1.3b. Light can effectively become trapped in crevices and holes where multiple reflections enhance the coupling

into the material. Once inside these protruded structures, multiple internal reflections can guide the light into the bulk. The degree of enhancement depends on the particular geometry and dimension of the surface features [11].
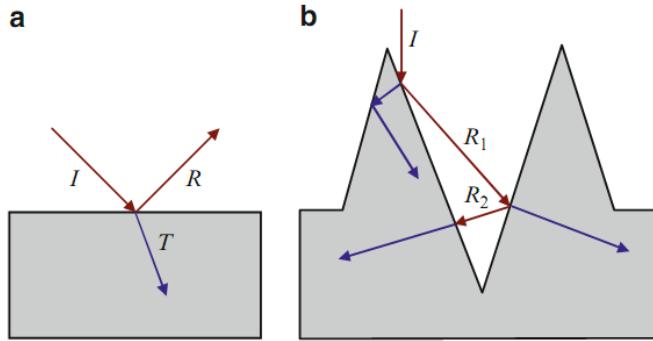
Fig. 1.3 Light specularly reflecting from a flat surface (a). Multiple reflections from protruding structures enhance light coupling into the material, and refraction causes the light to propagate at oblique angles, increasing the optical path length (b) [12].

Moving still smaller, surface features with dimensions much smaller than a wavelength are not individually resolved by the light, yet periodic arrays of sub-wavelength structures can contribute significantly to the optical response. This is commonly known as the "moth-eye effect" [13], which is responsible for the AR camoflauge of a moth's eye. A simple explanation for this phenomenon is that the medium takes on a volumetric average of the optical properties between that of the material and the surrounding medium [14, 15].

Table 1.1 Multiple length scales over which reflectivity and absorption are determined by surface features [12]

Feature size	Influence on reflectivity
$\gg\lambda$	Light trapping due to multiple reflections enhances coupling into the material. Light refracted at oblique angles increases the effective optical path length.
$\sim\lambda$	Small features can successively scatter light, increasing the effective optical path length and enhancing absorption
$\ll\lambda$	Sub-wavelength structures can reduce reflections through the moth-eye effect [13].

The tapered nanostructures, therefore, cause the effective optical properties to change continuously from that of air to that of the material, essentially acting as a GRIN AR layer. The breadth of length scales over which surface texture affects reflectivity, as summarized in Table 1.1, indicates that

surface texturing over multiple length scales can lead to significant reductions in reflectivity and can enhance the absorption of light by the material.

1.2   Properties of titanium oxide ceramics

This section presents an overview of ceramic properties, with a particular focus on electrical properties, which were the key to the realization of the MesMesh project wear sensor [16]. Within this project [17, 18], where a ceramic based sensor had to be produced to detect wear in moulding components, the electrical properties of the material to be used have to be carefully chosen. Within the 'ceramic' category, a very broad range of materials is available. However, the following properties can be considered to be representative of most ceramics: 1) brittleness (low ductility); 2) good resistance to chemicals and harsh condition (i.e. high temperature); 3) poor electrical and heat conduction; 4) high compressive strength and low tensile strength [19]. Some ceramics are good conductors of electricity or semiconductors. The resistivity of ceramics extends over more than 20 orders of magnitude, and ceramics exhibit the full spectrum of electrical properties, ranging from metallic to insulating electronic conductors, and from fast ionic to insulating ionic conductors [20]. The difference in electrical conductivity which spans for many order of magnitude, among metals, semiconductors and isolators can be related to differences in the carrier density in a different type of materials.

Carrier density is the number of charge carriers (which are necessary for conduction) per volume unit. An optimal situation to maximize conductivity is to have a similar number of electrons in occupied sites and unoccupied sites (carriers), which is the case in metals. A common strategy (particularly useful for semiconductors) to modify the electronic conduction of material, is to dope the material with specific impurities, effectively introducing defects into the structure of the material and modifying the ratio between sites occupied by electrons and unoccupied sites, which ultimately act as charge carriers.

As with the case of electronic conductors, the magnitude of ionic conductivity is determined by the ion carrier density and the ion mobility

26

(charge and size dependent). Ionic conduction is, therefore, determined by the ratio of occupied interstitial sites and sites in the rest of the lattice and on their mobility within the lattice.

The main subcategories of ionic conductors are [20, 21]:

i. *Fast Ionic Conductors (FICs)*, which despite being solids exhibit conductivity similar to one of the molten salts (where ions freely move) at temperatures well below the melting point of the material. They are characterized by a highly ordered and immobile sublattice (framework) which provides channels for ion transport and mobile carrier sublattice which are randomly distributed over the structure and move within the framework. In this case, high carrier densities are well coupled with high ion mobility. Hence, the ionic conduction is highest.

ii. *Solid Electrolytes*, which represent an intermediary case, where the charge carriers do not move within the network as freely as in the case of FICs. The reduced ionic conductivity could be associated with larger ions being trapped within the framework.

iii. *Ionic Insulators*, where the density of free ion carriers is very low compared to FICs and Solid Electrolytes and therefore the ionic conduction is small.

As with electronic conductors, where the conductivity can be modified by doping, a high concentration of ionic carriers can be introduced in solids, often by modifying the stoichiometry (i.e. modify the positively charged cation to negatively charged anion ratio), effectively generating a highly defective solid. A common example is represented by stabilized zirconia, where high oxygen ion mobility and conductivity is reached at 1000°C by introducing lower valent (i.e. having a lower charge) cations, such as calcium ions (Ca^{2+}). Particularly relevant to the wear sensor construction is the case of titanium suboxides of the Magneli family (Ti_nO_{2n-1}), where the presence of oxygen vacancies enables an increase in conductivity in comparison with stoichiometric titanium dioxide

TiO_2. Highly conducting ceramics (both electronic and ionic) are particularly desired in applications, where the conductive material has to withstand a corrosive environment and elevated temperature, whereas semi-conducting ceramics are exploited in several types of solar cells, and FICs and solid electrolytes are used in fuel cells and other electrochemical devices.

A wear rate of conductive ceramic of wear sensor must be similar to that of the hardened steel to be used in a moulding apparatus. Measurements indicated that the hardness of steel samples used for mould forms is 780 Vickers, and, therefore, the optimal hardness of both the insulating component and the conductive fibre should be within the range 700-800 Vickers (assumes hardness and wear are inversely proportional). Taking into account all electrical, mechanical and thermal limits, as a conductive fibre in the real-time wear measurement system for the project was selected titanium suboxides (Ti_nO_{2n-1}). The presence of oxygen vacancies in this material sensibly reduces the resistivity of the material (compared to titanium dioxide), which effectively becomes an ionic conductor [22].
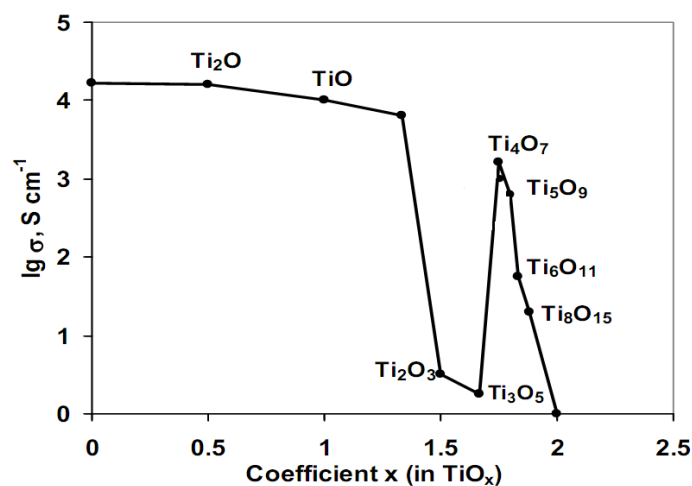
Fig. 1.4 Electrical properties of Magneli family (Ti_nO_{2n-1}) ceramics [22].

Ti_4O_7 is an electrically conductive ceramic material (commercially known as Ebonex™ [23]), which is part of the sub-stoichiometric (oxygen-deficient) "Magneli family" of titanium oxides (see Fig. 1.4). The Magneli family indicates a homologous series, which in the case of titanium can be

represented by the general formula Ti_nO_{2n-1}, with n = 4 - 10. Ti_4O_7 is as made up of three TiO_2 octahedra and one TiO octahedral. Its conductivity, comparable to that of graphite [63] is mostly due to the presence of vacant sites in the TiO lattice, enhancing electric conduction [64]. Because of the presence of oxygen vacancies, electrical conduction is enhanced (ionic type conduction) and therefore several titanium suboxides (or a mixture of them) from the Magneli family are of interested for the development of the conductive ceramics. Ti_4O_7 can be obtained by chemically reducing titanium dioxide (TiO_2) at a high temperature (1000-1500°C), using hydrogen or carbon as reducing agents [24]. However, its formation has also been reported from a composite material based on titanium and ruthenium oxides, prepared from liquid precursors (alkoxides and chlorides) via the sol-gel coating method, when annealed at 500°C in a reducing (hydrogen) atmosphere [25], suggesting a relatively low-temperature synthetic route may be feasible. Since recently (2014) this material is commercially available under Ebonex™ trademark [26] as a powder. The samples of titanium suboxide ceramics were obtained from the project partner from Bath University, England.

1.3   Laser-matter interaction

In this subchapter intence coherent light in form of a ultrashort pulse interaction specifics with the matter will be discussed.

1.3.1   Ultrashort pulse-metal interaction

It was shown experimentally [27] that the process referred to as the inverse *Bremsstrahlung* is the main cause of energy absorption in the skin layer by the electronic gas. This process can be defined as the absorption of photons by electron-ion or electron-electron scattering. When metallic materials, considered as the system of stationary ionic lattice and a surrounding electronic gas, are affected by electric fields of high intensity, the intrasystem interaction is altered. The increased effective electron velocity, which can be expressed as:

$$v_{eff} = \sqrt{v_{te}^2 + (\frac{eE_l}{m_e\varpi_l})^2} ,$$ (1.3)

where the first term v_{te} is electron thermal velocity, and the second is the velocity obtained by electron because of acceleration from EM field. It increases electron-ion collision frequency and consists of the elementary charge e, external electric field E_l, electron mass m_e, and external electric field frequency ϖ_l. As a natural consequence, absorptive material properties change and for the inverse *Bremsstrahlung* process at such conditions can be divided into two regimes with a distinctive spatial absorption rate κ_{ib}^p of the optical energy. In the case when $v_{te}/\frac{eE_l}{m_e\varpi_l} > 1$:

$$\kappa_{ib}^p = \frac{\kappa_{ib}}{1 + \frac{3(\frac{eE_l}{m_e\varpi_l})^2}{2v_{te}}} ,$$ (1.4)

and when $v_{te}/\frac{eE_l}{m_e\varpi_l} < 1$:

$$\kappa_{ib}^p = \frac{\kappa_{ib}}{1 + (\frac{(\frac{eE_l}{m_e\varpi_l})^2}{v_{te}^2})^{\frac{3}{2}}} .$$ (1.5)

Here, κ_{ib} denotes the unperturbed spatial damping rate. It was observed experimentally as low absorption dependence on temporal radiation properties at high intensities and the existence of resonance absorption [28].

Since this initial energy deposition occurs by a system of relatively loosely bound carriers, the following process is the inter-electronic scattering thermalisation to Fermi-Dirac energy distribution. The electronic system of the metals also possesses relatively low heat capacity and this, together with inefficient electron-phonon coupling, leads to lattice thermalisation in the time scale of picoseconds [29] and at the same time allowing heat transport by diffusive mechanisms to occur. The distance of this diffusion can vary and

exceed the skin layer (or optical penetration depth) and is referred as *thermal penetration depth*. Furthermore, as a result of the significant difference between the rate of these two processes, which is estimated to be 1 to 2 orders of magnitude [30], for a defined duration a state of extreme non-equilibrium is created. Intense and short light pulses create highly non-equilibrium conditions and extreme localized heating. To give an explanation of the further evolution of the system of this type, a two-temperature model is widely applied [31-34]. The model accounts for the different temperatures of electrons T_e and lattice T_l, when the laser pulse duration is less than phonon-electron interaction time and describes energy transport by the following expressions for electrons and lattices:

$$C_e \frac{\partial T_e}{\partial t} = -\frac{\partial Q(z)}{\partial z} - \gamma (T_e - T_l) + S(z,t), \qquad (1.6)$$

$$C_l \frac{\partial T_l}{\partial t} = \gamma (T_e - T_l), \qquad (1.7)$$

where

$$Q(z) = -\frac{k_e \partial T_e}{\partial z}. \qquad (1.8)$$

Here, C_e and C_l denote the heat capacities of electron and lattice subsystems, γ is the electron-lattice coupling parameter, k_e is the thermal electron conductivity, and $S(z,t)$ expresses the energy influx from the laser pulse.

1.3.2 Material laser ablation

The electronic system of the metallic material reacts to laser radiation almost immediately and results not only in the relaxation processes but also in the photoemission of electrons [35]. Another relatively fast process is ionic or atomic desorption at local surface excitations or defects (e.g. grain boundaries, dislocations) [36]. Although measurable, these processes contribute only to negligible material transport and are thus of limited application importance for the μm-scale structuring.

In the case, when the amount of energy delivered by laser pulse is sufficient, a different kind of phenomena may be observed. The proceeding heating of the lattice accumulates energy in the heavier ionic system, and this in turn suppresses the bonding. Depending on the pulse energy and duration melting, boiling, vaporization or phase explosion [37] might follow. In contrast to initial material desorption, these all are collective processes, having a controllable extent. In the case, when a removed material plasma plume is generated and a resultant crater created in the substrate, the process is generally referred to as laser ablation.
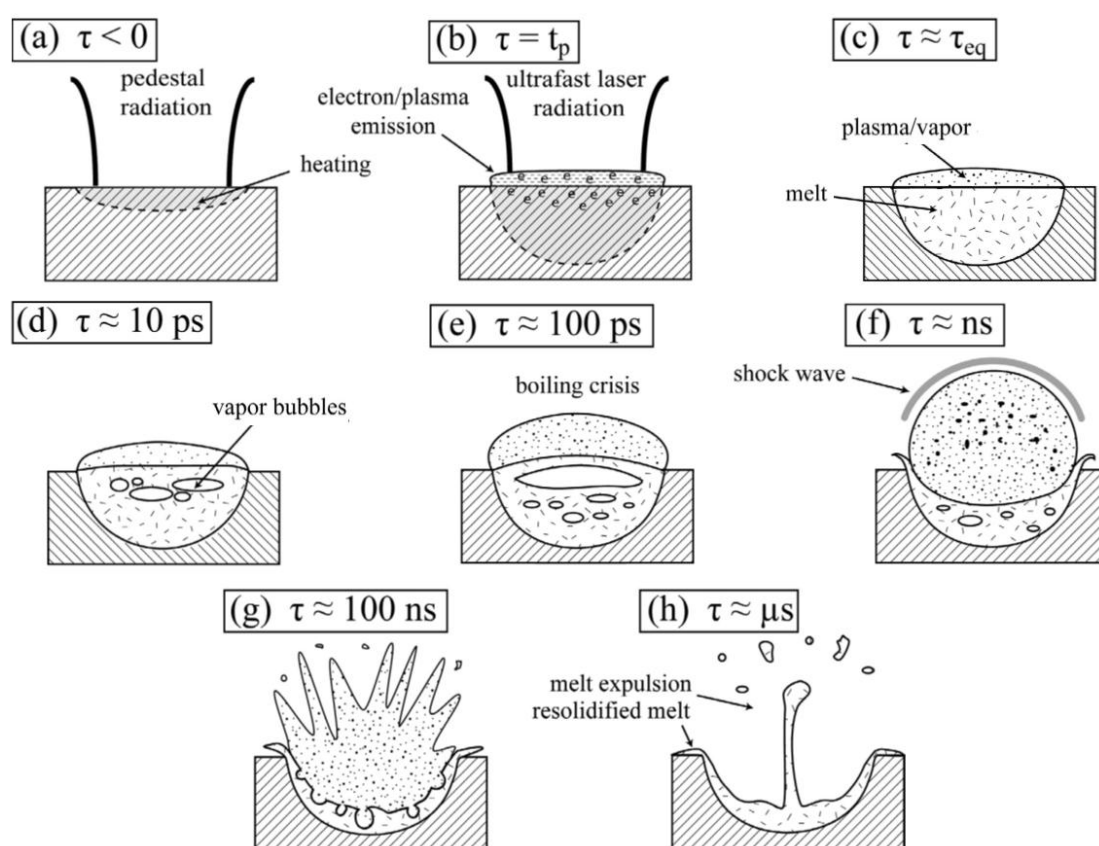
Fig. 1.5 Qualitative model of metal ablation at large intensities [38].

Generally, in dependence on the intensity contrast ratio of the applied ultrafast laser radiation, possible heating of materials induced by the radiation pedestals with durations of several ns before the arrival of the main femtosecond pulse at t < 0 should be considered [38] (Fig. 1.5a). During the interaction of the ultrafast laser radiation with the material, the optical energy

is transferred to the electron system (Fig. 1.5b). At irradiation intensities $I >$ 10^{13} W·cm^{-2}, emission of electrons and generation of a hot plasma from the surface occurs on a time scale comparable to the pulse duration, which can further contribute to surface heating. After thermalization of the electron system and the lattice t ~ t_{eq} (Fig. 1.5c), the material can be ablated in different ways. The material aggregation state can be transferred from solid to either plasma, vapour, liquid or a mixture of all aggregation states. At large intensities, the material is melted mainly by the thermal melting mechanism. Normal vaporization is the major ablation process on this time scale. At low irradiation intensities, the heterogeneous nucleation (normal boiling) is the major mechanism by nucleation on the time scale of several ns. However, if large thermal gradients are induced by the ultrafast laser radiation ($I >$ 10^{13} W·cm^{-2}) homogeneous nucleation (phase explosion) occurs (Fig. 1.5d). The material undergoes a rapid transition from superheated liquid to a mixture of vapour bubbles and liquid droplets. Phase explosion observed experimentally [38] in the time range t = 0.7 - 1 ns is therefore considered as the responsible ablation mechanism. However, another ablation mechanism - called "boiling crisis" - is also proposed to be a considerable mechanism as well (Fig. 1.5e), since the rate of heterogeneous nucleation dramatically increases near T_c. As the vapour bubbles grow and coalesce, a large bubble may be formed below the surface. When the bubble reaches a critical size it will burst, propelling highly pressurized vapor, liquid melt droplets and plasma into the plume. A shock wave is induced as a result of this intense material ejection (Fig. 1.5f). The propagation of shock waves is detectable in the time scale t~ 3 — 100 ns. Ablation on the time scale of several 100 ns is still driven by the nucleation, i.e. phase explosion, and intense vaporization (Fig. 1.5g). An increased ejection of vapor and sub-micrometer scaled particles has been observed at t ~ 200 — 700 ns. Finally, an intense ejection of apparently liquid melt occurs on the time scale t ~ 1 μs (Fig. 1.5h). Either continuous liquid jets or melt droplets with dimensions of several μm are evident. The recoil pressure

is the major mechanism of material ejection here, and it often results in "piston effect". The fact, that liquid melt jets can be observed even during ablation with a single fs pulse [39], indicates that a crater of a significant depth is produced up to the time t~ μs and the melt is still available inside the crater. Continuous liquid melt jets cannot be observed at confined samples and in a vacuum, which confirms the assumption of ablation mechanisms at t ~ μs driven by pressure gradients induced in the adjacent atmosphere.
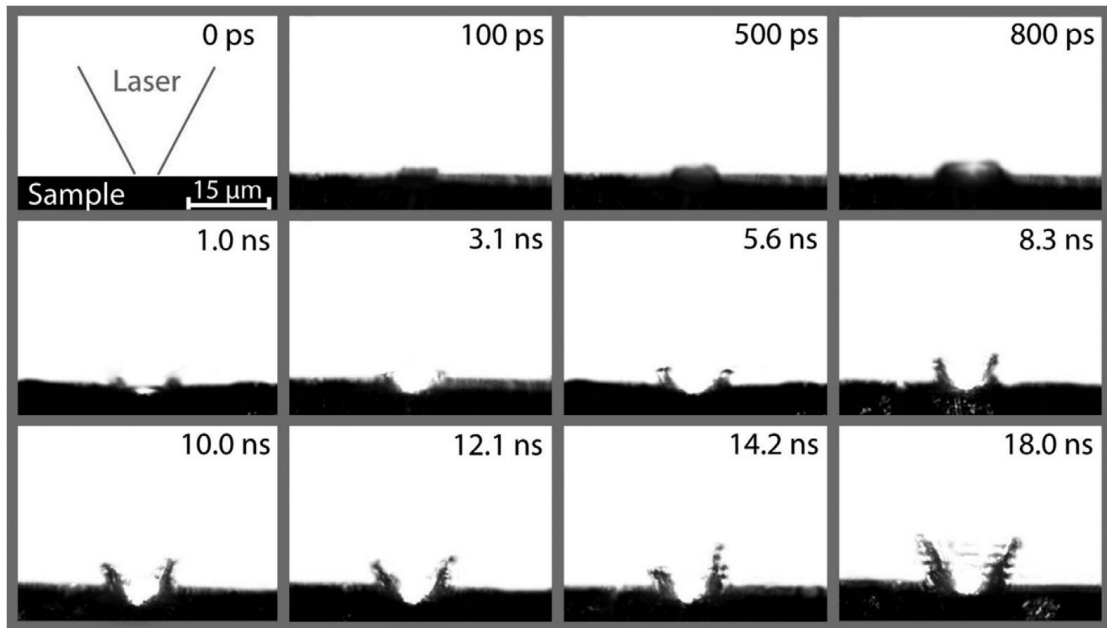
Fig. 1.6 Plasma and melt dynamics on aluminium target up to τ = 18 ns after irradiation with a fs pulse (τ_p = 80 fs, λ = 800 nm, F = 10 J·cm^{-2}), detected by time-resolved shadowgraphy [38].

In [38] the ablation dynamics of bulk aluminium and copper has been detected up to ~20 ns after irradiation with ultrafast laser radiation at fluences F = 10 J·cm^{-2} (~100 F_{thr}) and wavelength λ = 800 nm. A shadow of the ejected material can be detected at the delay τ = 100 ps (Fig. 1.6). At the delays τ = 0.5 and 0.8 ns, there are bright regions in the shadow of the ejected material. These bright regions are not evident at the delays τ > 1 ns anymore. The dynamic process observed in the shadowgraphs at $\tau \gg$ 1 ns may be explained with phase explosion [37]. According to numerical estimations, the target surface of aluminium irradiated with an intense ultrashort laser pulse will be overheated

up to ~ 10^5 K. This temperature is more than an order of magnitude larger than the thermodynamic critical temperature of aluminium $(T_c = 5720$ K), and inevitably leads to an extremely large pressure in the ablated region [37], and such a great pressure will be released through the adiabatic expansion. Shadowgraphs at delays smaller than 3.1 ns only exhibit the outward expansion of the laser heated area. The corresponding inward expansion compresses the interior of the target and transforms thermal energy into mechanical, which induces a thermoelastic wave and causes material ejections at larger delays. The thermal phase explosion and non-thermal thermoelastic wave mechanisms are combined at this point. In fact, the existence of a thermoelastic wave directly underneath the surface layer at which phase explosion takes place has been predicted by molecular dynamics simulations [40, 41]. As the material expands, it cools close to the critical temperature, around which the material will undergo a transition from a superheated metal liquid to a dielectric liquid which is nearly transparent. Thus, in this experiment, the formation of the material extrusion with bright inner regions at delays $\tau = 0.5$ and 0.8 ns presumably represents the cooling process of the ejected material, and the outer edge of the material ejections is the result of diffraction of the ejected plume. When the plume further cools to reach the metastable state the density and refractive index of the plume decrease due to the transition from a liquid to a mixture of vapour and liquid, which leads to the blurring of the interface between the ambient air and the ejected material, and consequently the dark edge with the bright inner regions disappear (delays $\tau \gg 1$ ns). The same behaviour has also been observed on copper samples. At larger fluences $F > 100$ F_{thr}, thermoelastic waves are not the prevailing ablation mechanism at $\tau \sim 1$ ns, as no plumes with bright inner regions have been detected.

Further experimental and theoretical investigation lead to the discovery of two separate ablation regimes [42]. The regime of the *gentle* ablation is written as:

$$L \approx \alpha^{-1} \ln(\frac{F}{F_{th}^{\alpha}}) \qquad (1.9)$$

35

and similarly *strong* ablation:

$$L \approx l \ln(\frac{F}{F_{th}^{l}}). \tag{1.10}$$

Here, L is the depth ablated per single pulse, α^{-1} is the optical penetration depth, l is accordingly the thermal penetration depth, F_{th}^{α} and F_{th}^{l} express the threshold values for both distinctive regimes. These expressions clarify the nonlinear nature of the energy dissipation: while electronic heat capacity stays constant, thermal conductivity is growing with the increased temperature of the electronic system. This leads to higher conduction, and increased lattice thermalisation durations with the higher values of deposited energy, and ablated volume is defined by thermal penetration depth: the onset of strong ablation is being observed. On the other hand, the gentle ablation reaches optically excited depths (Fig. 1.7).
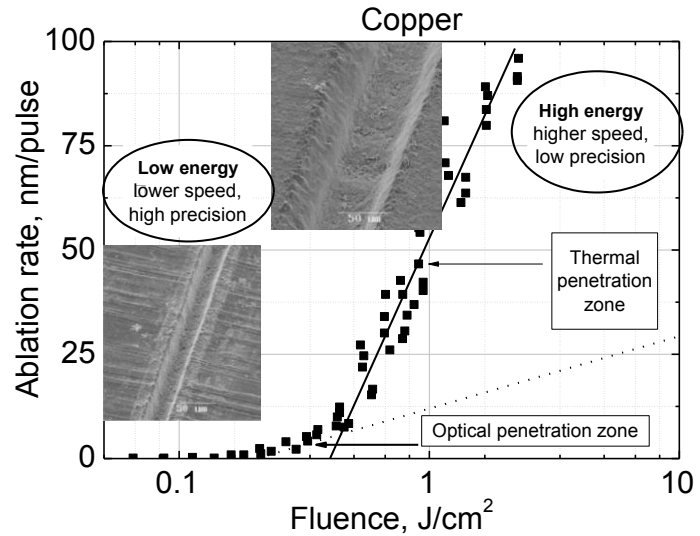
Fig. 1.7 Sketch of ablation rate dependence on the fluence at pulse durations of 45 fs for copper [43].

Thus, by proper choice of laser fluence (energy density) lasers can be used as a versatile tool of extreme precision, flexibility, omitting excessive heating and negative processes such as melting, chemical structure altering and other. Numerous experimental works with various materials, including but not limited to metallic substances [44-46] testify that.

36

Two lines related to the optical penetration zone and thermal penetration zone have been observed in metal ablation experiments for pulse durations from 50 fs to ~10 ps [42, 47]. Two ablation regimes for different metals for fs and ps-pulses are: first at low fluences up to 1–1.5 J/cm^2 and second at high fluences beginning from 3-5 J/cm^2. Ablation thresholds and penetration depths are deduced as functions of the pulse duration. Increasing the pulse duration, the threshold fluence increases, and the effective energy penetration depth is reduced. While in the low fluence regime, the penetration depth is close to the theoretical optical penetration depth, at higher fluences, the effective heat penetration depth is 10–20 times bigger. The best results in terms of micromachining quality are obtained in the low fluence regime but associated with significantly lower ablation rates.

1.3.3 Altering material optical properties during ablation process

In [48] it was shown that at laser fluences above the ablation threshold up to 70 % of the incident pulse energy can be retained in the metallic sample following single-pulse fs-laser ablation in 1-atm air. A calorimetric technique which detected the temperature rise due to residual energy that remains in the sample following ablation was used for the measurements. It was shown that the major factors governing thermal energy coupling to the sample are the laser fluence and ambient gas pressure. The coupling in case of Al sample raised from initial 35 % to 70 % when the single laser pulse fluence was increased from 0.9 J/cm^2 to 4 J/cm^2. A Ti:sapphire laser producing 60 fs pulses with pulse energy of 1.5 mJ was used in experiments. The residual thermal energy coefficient can decrease to below the absorptance of an undamaged surface when the ambient gas pressure is reduced. Laser ablation in a vacuum appears to be advantageous to reduce residual load by 3-4 times compared to that in air.

In [49] was reported direct measurement of the thermal energy remaining in the bulk of Cu, Mg, Au and Si samples following multi-pulse femtosecond laser ablation. The same calorimetric technique and Ti:sapphire laser only in burst mode as in [48] were used for measurements. It was shown

that with a sufficiently large number of pulses at high fluence, virtually all the incident laser energy could be retained in the sample. In experiments bursts with 500 femtosecond pulses were used. As can be seen in Fig. 1.8 in the case of Cu the residual energy coefficient (REC) defined as the ratio of residual energy to total incident laser energy in each burst increases abruptly when the samples are exposed with laser fluence above the certain threshold fluence, which is 2.5 - 4 times higher than ablation threshold. The REC value increase was from 0.13 to 0.44. It also depends on the total number of pulses applied to the same spot on a sample. Fig. 1.8 shows that seven identical bursts of 500 pulses/burst (3500 pulses in total) at F = 0.9 J/cm^2 cause REC to reach a value of 0.9 in air. Following laser ablation, surface roughing, and the formation of surface structures and craters can all change the sample absorptivity and thus induce a change in residual energy.
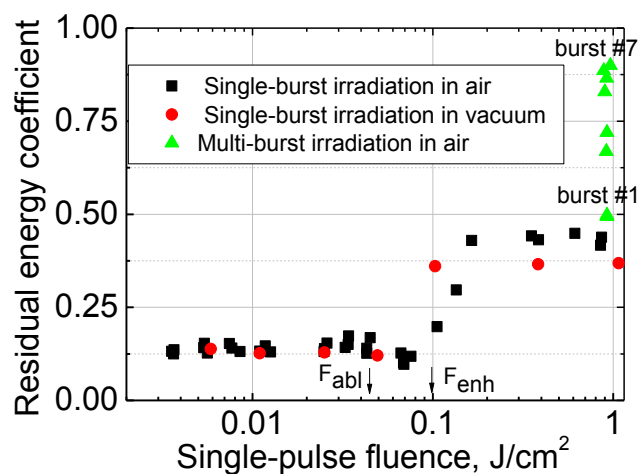
Fig. 1.8 Residual energy coefficient for Cu as a function of single-pulse fluence in air and vacuum. The number of femtosecond laser pulses in a single burst is 500 [49].

In [50] ablation thresholds of copper, titanium, niobium and stainless steel were measured for different numbers of the pulses, and it was shown that the threshold fluence depends on the number of pulses applied to the same spot. The laser pulses used for the study were 775 nm in wavelength, 150 fs in pulse duration, and the repetition rate used was 100 Hz. The accumulation behaviour results from the build-up of plastic deformation induced by the laser pulses, clearly seen in Fig. 1.9 a-c, also called ripples. They were observed on metals [44, 50, 51], dielectrics [52] and transparent materials [53, 54]. During

the stronger ablation phase much rougher structures occurred (Fig. 1.9d). The observed morphologies seem to suggest that normal vaporisation and phase explosion are the most probable physical mechanisms responsible for material removal during ablation. Surface structure modifications can change the hydrophilic properties. Steel can be made hydrophobic by microstructuring its surface laser [55, 56].
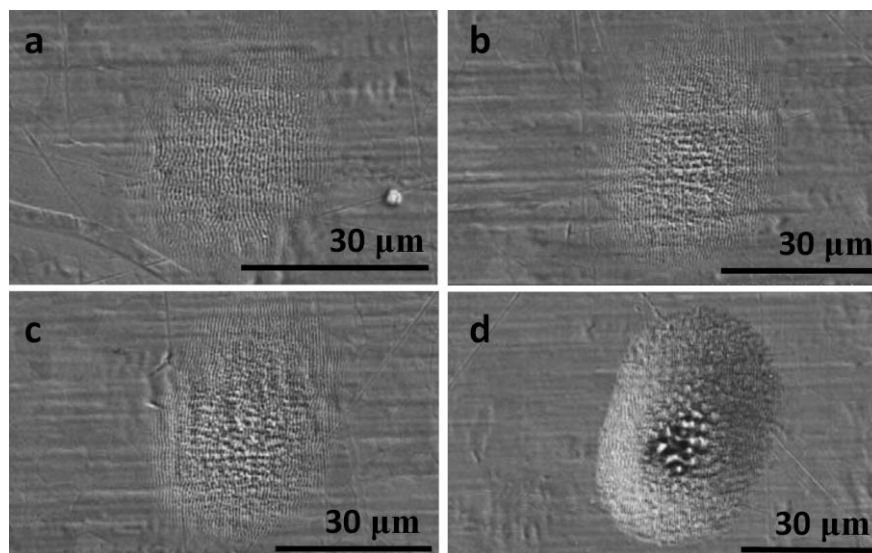
Fig. 1.9 SEM images of craters produced in stainless steel, grade 316L, at 1.53 J·cm-2: (a) 5 shots, (b) 10 shots, (c) 15 shots, and (d) 100 shots. The onset of the strong ablation phase is clearly visible at the centre of the crater in (d) [50].

Laser ablation of solids in liquids is an efficient way for the generation of a large variety of self-organized metallic nanostructures. Under sufficient high laser fluence, the surface of target melts and the melt is subsequently dispersed into the surrounding liquids under the recoil pressure of its vapor. At fluencies close to the melting threshold of the material, short laser pulses melt only the microprotrusions on the target surface giving rise to the efficient formation of nanostructures [57]. These nanostructures are self-assembled since their period is several orders of magnitude smaller than the laser spot size ranging from 50 to 1000 nm, depending on the target material and laser wavelength.

1.3.4 Experimental determination of ablation threshold

There are several methods to determine material ablation threshold [58-60]. The threshold energy fluence for single or multiple pulses has been determined using standard method proposed by Liu [59], which assumes a Gaussian profile for the spatial energy distribution of the laser beam. This method has been formerly developed to estimate the laser spot size and successively used to calculate material threshold fluence [2,10-15][50, 61, 62]. It is based on the following equation:

$$D^2 = 2\omega_0^2 \ln\left(\frac{F_0}{F_{th}(N_{tot})}\right),\tag{1.11}$$

which relates the squared diameter of the ablation crater D^2 to the laser spot radius ω_0 on the target surface and the ablation threshold fluence $F_{th}(N_{tot})$ when N_{tot} pulses are applied. The peak laser fluence F_0 is related to the total energy E_0 by:

$$F_0 = \frac{2E_0}{\pi\omega^2}.\tag{1.12}$$

Therefore, by combining these two equations, it is possible to find a relation between the squared crater diameters and the pulse energy, which can be directly measured. A logarithmic fit of the experimental data when the curve is extrapolated to cross the abscissa axis (that is, where $D = 0$) fluence threshold is determined. Practically, the experimental data are represented on a graph with the logarithmic abscissa scale and fitted to linear regression of the form $D^2 \sim a \cdot \ln(F_0) + b$. Fluence threshold is determined as a line cross with the abscissa axis (-b/a) and the radius of the focused laser beam on the surface estimated as the curve slope $2\omega_0^2$.

1.3.5 Laser ablation influencing factors

There exist many techniques for precise machining, however, laser-based in the certain application can offer either best results or are the only means to achieve the task [63, 64]. There are several reasons for this. First of all, competing techniques have inherent drawbacks, e.g., Electro-Discharge Machining (EDM) [65] is a robust method for precise fabrication. However,

when the steel is machined, a melted and re-solidified layer experiencing undesired quenching and tempering resulting in surface brittleness is formed [66]. The second point is that only a few methods can offer the machining with resolution down to several microns. The third, the laser can fabricate materials directly, without mechanical contact. Actually, laser micromachining is not bound to a group of materials. It can handle virtually any substance.

However, laser machining techniques also possess some disadvantages. One of the biggest flaws is the inverse relation between precision and structuring performance, which, however, is the cornerstone for all techniques. In order to sustain flexibility, direct laser ablation (DLA) is chosen in most cases; therefore, the area ablated during a given time is decreased with tighter focusing (higher resolution). Furthermore, with small ablated volumes per single pulse, instabilities due to poor debris removal begin to form thus limiting structure depth (cumulative exposure) and precision [67].

To concentrate existing experimental data, the most important laser ablation influencing parameters (apart from the sample itself) are listed below:

Pulse duration [68-71] - t[s] is the duration of light pulses emitted by the laser.

Pulse energy [72] - E_p[J] is the energy carried by the optical pulse.

Pulse fluence [73, 74] – F[J/cm^2] is an areal density of radiant energy incident on a surface.

Peak power – P_{peak} [W] is the maximum instantaneous optical power during the laser pulse. For example, with $t = 300$ fs (Gaussian-shaped in time), $E_p = 200$ μJ, the peak pulse power is $P_{peak} = 0.94 \cdot \frac{E_p}{t} = 626$ MW.

Peak intensity - I_p [W/cm^2] is the peak power per unit area.

Repetition rate [75, 76] – f [Hz] is a frequency at which a laser generates light pulses.

Polarization [77] – is a property of light describing the orientation of the EM field vector oscillations. In laser micromachining linear, circular or elliptical states of polarization are common.

Wavelength [78] – λ [nm] is spatial EM wave period, determined by the gain medium used in the laser. However, this fundamental wavelength can be discretely shifted to the desired part of the spectrum through harmonic generation processes.

Focused spot size [79] or beam waist d_0 [m] is the minimal beam diameter to which the focused beam converges. For a Gaussian beam, the focused spot size can be approximately estimated:

$$d_0 = \frac{f\lambda}{\pi d} M^2, \tag{1.13}$$

where f is the focal length, d is the collimated beam diameter at the objective entrance; M^2 is the beam quality parameter.

Rayleigh length - z_R [m] is the distance along the propagation direction of a beam from the waist to the point, where the intensity is halved. It can be estimated using the formula:

$$z_R = \frac{\pi \omega_0^2}{\lambda}. \tag{1.14}$$

All these parameters must be taken into account.

As a brief conclusion, insight can be given here that fs fabrication of extended 2.5D structures is not a straightforward task, and there exist apparent limitations on the most essential characteristics of the machined microstructure. Next subchapters will cover some of the important micromachining factors in more details.

1.3.6 Reducing structure processing time by increasing the power and pulse repetition rate

The progress of micromachining with ultrashort-pulsed lasers is inextricably connected with the progress of lasers [80]. During the last decade, the first steps in researching the feasibility of ultrashort pulses for micromachining were made. Numerous investigations using low repetition rate (1-15 kHz) high pulse energy (>200-300 µJ) lasers, such as Ti:sapphire, were carried out [81-85]. It was assumed that the ablation rate is mainly constant and the reduction in processing time is proportional to the increase in the repetition rate (Fig.

1.10). However, it was found that an optimal fluence exists for which good quality and high ablation speed can be obtained [88].
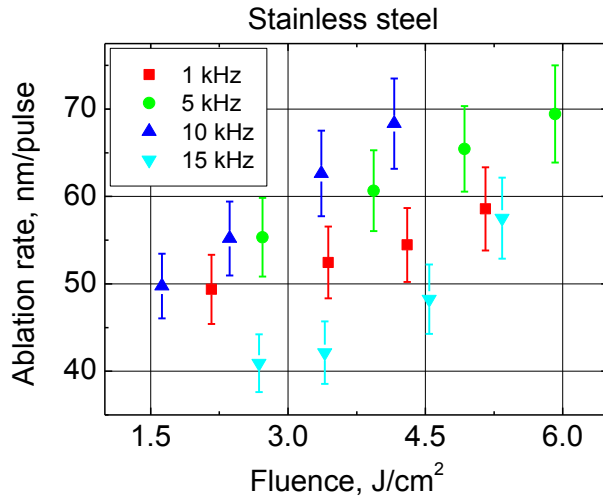
Fig. 1.10 Ablation rates of stainless steel in function of the fluence at 1, 5, 10 and 15 kHz [84].

Ablation efficiency can definitely be increased by laser power. Power scaling in the last decade has led to lasers generating average power levels well above 50 W for applications like structuring turbine blades, micro moulds, and solar cells. However, high average laser powers (~100 W, 6 ps, 800 kHz) can have a serious adverse impact on the ablation quality in ultrashort pulsed laser material processing of metals. With respect to the scanning speed, two ablation regimes exist differing significantly in ablation quality. A sharp transition between a smooth, reflective and an uneven, dark ablated surface is observed when the scanning speed is changed [86]. The surface of stainless steel in the low-quality regime not only has a much lower reflectance, but is also covered with small bumps of about 10 μm and is oxidized. The study [86] claimed that a minimal scanning speed exists yielding a high-quality ablated surface. It increases for higher fluences and sample offset temperatures, which depend on the deposited heat remaining in the laser-irradiated area after each pulse, as well as on the temporal and spatial displacement of the subsequent pulses in the micromachining algorithm. Heat accumulation leads to a saturation state of the surface temperature depending on the processing parameters. When the threshold temperature of ~600 °C is reached for stainless steel (1.4301), detrimental effects appear.

Micromachining with bursts of ultrashort (1 ps) pulses was first published in 1999 [87]. Using bursts of ps-pulses with high pulse-repetition frequency for micromachining can improve the ablation rates when the pulse energy of each single pulse is in the regime of "optimal-fluence-efficiency" [88, 89].

The increase in the specific removal rate with bursts is mainly caused by the smaller energy in a single pulse of the burst, which is nearer the optimum value for a maximum specific removal rate. However, the burst mode itself has an influence on the specific removal rate and the surface quality. For steel, the burst mode never led to a higher specific removal rate than single pulses with optimum fluence. If one is forced to work at fluences exceeding the optimum value, the maximum possible removal rate will never be attained [88, 90]. It is in this situation that the burst mode may lead to higher (but always below the maximum) efficiencies, due to the possibility of generating slightly molten surfaces with high optical quality where single pulses would lead to cavity formation destroying the surface quality. Furthermore, it is assumed that the state of the surface during the burst (solid, melting, liquid, boiling and vapor) strongly influences the surface quality. For copper, the burst even decreased specific removal rate [90]. Experiments confirm that too many pulses in a burst generate excessive heating of the sample so that the maximum usable number of pulses for non-thermal ablation is in the range of 5 to 10.
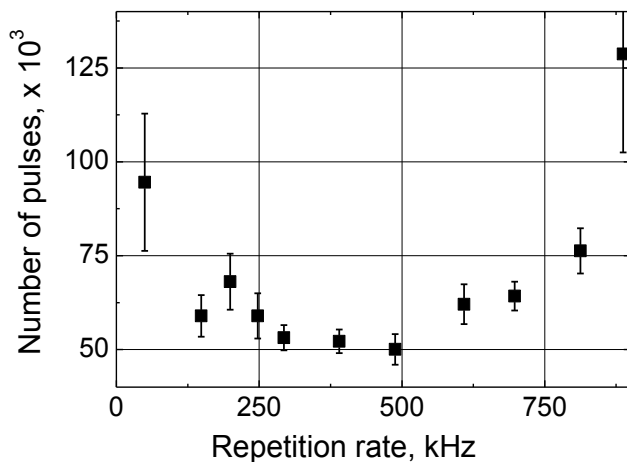
Fig. 1.11 An average number of pulses to breakthrough for 0.5 mm thick stainless steel (Fe/$Cr_{18}Ni_{10}$) sheets at various repetition rates, for 20 µJ of pulse energy and 800 fs pulse duration [75].

Fig. 1.11 In [75] an experimental study on the drilling of metal targets with ultrashort laser pulses at high repetition rates (from 50 kHz up to 975 kHz) and high average power (up to 68 W), using ytterbium-doped fiber CPA system was performed. The number of pulses drilled through steel and copper sheets with thicknesses up to 1 mm were measured as a function of the repetition rate and the pulse energy. Percussion drilling experiments were performed in order to determine how the perforation time for a constant thickness of 0.5 mm of stainless steel relates to the repetition rate for low laser pulse energies. Therefore, an 11-mm focal length lens and pulse energies of 10 and 20 μJ were used, while the repetition rate was systematically varied in the range from 50 kHz to 975 kHz. For each parameter, the number of pulses required to drill through was determined. Both pulse energies yielded similar results except for the expected lower drilling times at higher pulse energies. Therefore, Fig. 1.11 shows the example results for 20 μJ pulse energy. If neither particle shielding nor heat accumulation has a role, a constant number of pulses required for drilling through should be expected independently of the repetition rate. Apart from some deviations below 150 kHz, which is related with mistakes in the detection system, this is observed for repetition rates below 500 kHz, yielding a roughly steady value between 50 and 70 kilopulses. However, completely different behaviour was found for repetition rates larger than 500 kHz. Here, the number of pulses required for drilling through increases with increasing the repetition rates. This can be ascribed to the perturbation of the drilling efficiency caused by particle shielding. Indeed, previous experiments showed that several tens of ns after ps-laser pulse impinged on a metal target, large particles and clusters are ejected from the surface and expand in an explosive way. This expanding particle plume is assumed to be generated by phase explosion after homogeneous or heterogeneous nucleation [7]. All this conglomerating material for some time stay in the atmosphere above the target surface, and incident light is absorbed, scattered and reflected. Studies of the particle evolution, carried out by

45

measurements of light attenuation in a pump-probe set-up, showed that this particle plume is extinguished after several 100 ns to few microseconds, depending on the laser fluence and the target material. In agreement with those results observed, at this energy level of 20 μJ, an increase in the drilling time due to particle shielding for repetition rates higher than 500 kHz was observed, corresponding to a time separation between consecutive laser pulses of 2 μs or lower. Analogous results were found for different material thicknesses. The thicker the sheet, the longer the time to drill through but the particle shielding effect occurred in the same range of repetition rate, independently of the sample thickness.
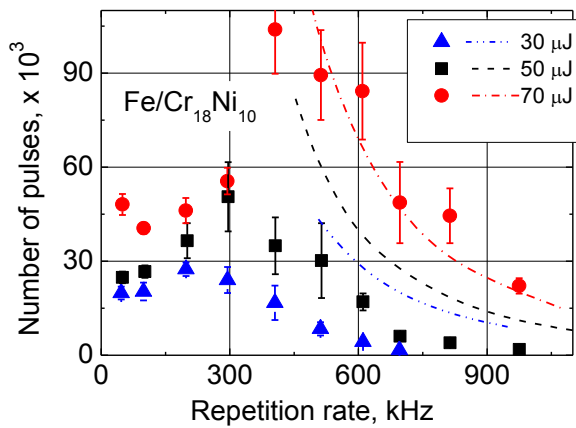
Fig. 1.12 Number of pulses required to break through steel sheets at various repetition rates. Experimental data are plotted in dots, while the respective lines represent the estimated melting threshold due to the heat accumulation effect [75].

Results obtained for stainless steel at larger pulse energy are depicted in Fig. 1.12. The experimental data reveal that by increasing the pulse energy, the particle shielding effect occurs already at lower repetition rates. For 70 μJ it is, in fact, already evident at 200 kHz. The second and most interesting feature is that, after the increase due to particle shielding, an abrupt drop in the number of pulses required to drill through is observed when further increasing the repetition rate. As far as the pulse energy increases, the number of pulses starts to drop at lower repetition rates (400 kHz for 30 μJ, down to 200 kHz for 70 μJ). Therefore, this mechanism seems to be energy-dependent as well.

A possible explanation for this effect is heat accumulation. A significant fraction of laser energy remains in the irradiated region and is diffused into the

surrounding material. For high repetition rates, the time between successive pulses may not be long enough for the heat to diffuse away from the focal volume before the next pulse arrives. Consequently, the energy accumulates in and around the focal volume. The temperature of the substrate increases and lower ablation threshold can be anticipated.

Two distinctive effects influencing the drilling efficiency at high repetition rates have been experimentally found and studied: particle shielding and heat accumulation. While the shielding of subsequent pulses due to the ejected particles leads to reduced ablation efficiency, this effect is counteracted by heat accumulation. At 400 kHz and 30 μJ pulse energy, smoother surfaces are present inside the hole, and a tall rim of molten material is formed all around the hole rim. This confirms that heat accumulation has an important role already at this repetition rate, at least in the case of stainless steel. Unfortunately, in this case, the quality of the hole is not suitable or useful for precise machining applications due to a large amount of molten material. For materials with high thermal conductivity such as copper, both effects are negligible for the investigated processing parameters. Therefore, the full power of the fiber CPA system can be exploited, which allows for trepanning high-quality holes in 0.5 mm-thick copper samples with breakthrough times as low as 75 ms.

Some investigations have been done on the influence of the repetition rate by using a Ti:sapphire regenerative amplifier laser with typical energies of 2 to 5 μJ/pulse at repetition rates of 100 kHz to 250 kHz [91]. Results comparing the micromachining of grooves machined at atmospheric pressure at 1 and 200 kHz showed the difference in quality. By using high fluence, in this case, 30 J/cm^2 at 1 kHz, the structure becomes irregular, and the grooves can be filled with a recast. Burr heights are also observable at the edges. This is not the case using a higher repetition rate of 200 kHz and a lower fluence of about 2 J/cm^2. With this parameters, micro machined structures are of better quality.

1.3.7 Influence of pulse duration and polarization on steel micromachining

A systematic study of the influence of laser pulse duration in ultrafast laser micromachining of stainless steel was carried out in [69]. Experiments were performed using a Ti:sapphire laser first and second harmonic in an air environment with an 110 fs - 10 ps pulse duration and repetition rate of 1 kHz. Holes and grooves were characterized using optical microscopy, atomic force microscopy and stylus profilometry. Melting was observed at >2.5 ps for stainless steel. The single-pass cut width of stainless steel is plotted as a function of pulse duration and laser pulse energy in Fig. 1.13. The cut width starts to increase at a pulse width longer than 2.5 ps with a laser pulse energy of 10 μJ. Melting can be avoided if the pulse duration for processing of stainless steel is less than 2.5 ps.
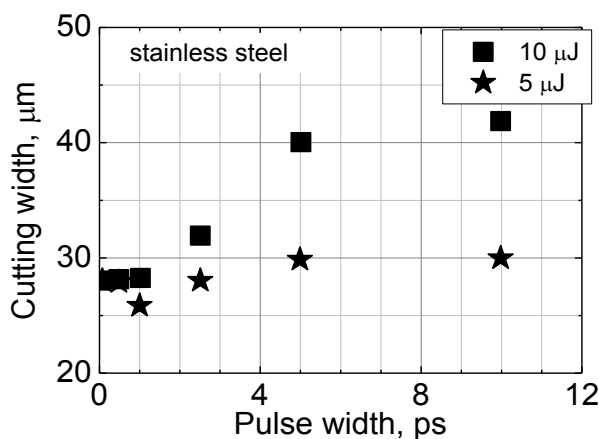
Fig. 1.13 Cutting width as a function of pulse width for stainless steel at the energy of 5 μJ/shot (*stars*), and 10 μJ/shot (*squares*). The measurement uncertainty was ±10 % [69].

In [92], a range of pulse durations between 10 ps and 1.4 ns at a wavelength of 532 nm was investigated for copper and steel with regard to the removal rate and surface quality. The trend of a decreasing removal rate with increasing pulse duration was confirmed up to a range of several 100 ps. In the pulse-duration range from 100 fs to 10 ps, the removal rate was also found to decrease for stainless steel [93]. The behaviour of the threshold fluence and the penetration depth indicates that heat conduction begins to dominate the energy transfer into the material when pulse duration is increased. The lowest surface

quality is always observed for ns pulse duration, where strong melting effects are observed.

Laser polarization also has an important role in micromachining quality [94-97]. It is well known that reflectivity from the surface depends on the light polarization if the incident angle is not perpendicular to the metallic surface (e.g. see Fig. 1.14). As a result, *p*-type polarized light can be absorbed much more at the metal surface if the incidence angle is in the range of 75-90 degrees. The absolute values of reflectivity versus different angles for both polarizations can be calculated using well-known Fresnel equations. For a typical hole drilling configurations, the reflectivity for the *p*-polarized light was found to be two times smaller than that of the *s*-polarized light due to the light reflected from the walls.
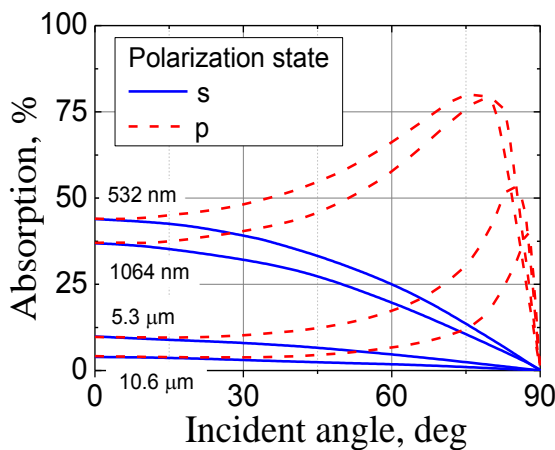
Fig. 1.14 Stainless steel absorption dependence on the beam incident angle [9].

Fig. 1.15 Optical microscope images of the machined silicon for differing numbers of passes and laser polarization (parallel and perpendicular) [69].
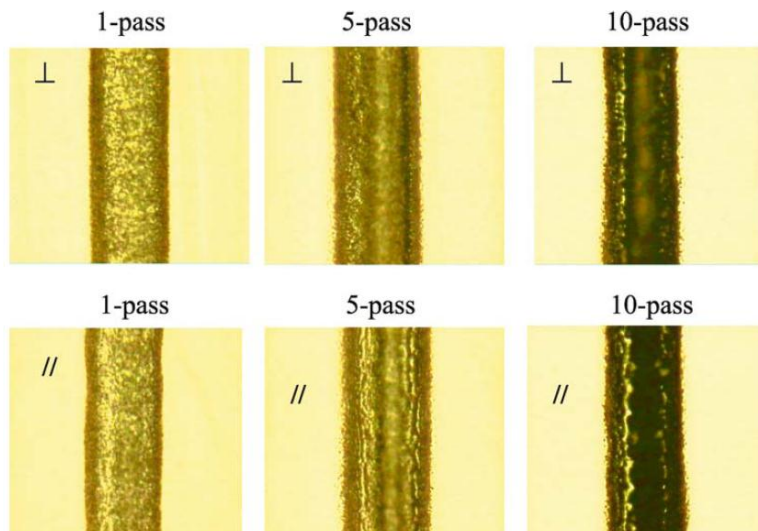
Fig. 1.15 shows optical microscope pictures of the entrance of the machined with a fs-laser (110 fs, 800 nm, 10 μJ) steel areas as a function of the number of passes and state of polarization [69]. Irregular cut edges appear if the polarization is parallel to the cutting motion and the irregularities are increased with a number of passes. Also, the data for cut depth as a function of the number of passes were examined. At a 10-pass laser cut, the cut depth drops about 25 %–30 % for laser polarization parallel to the cutting direction. These results show the important impact of polarization effects on edge roughness and cutting efficiency.

1.3.8 Improving surface quality of microcuts and grooves

For the generation of microscopic cuts and grooves, several basic parameters are mainly responsible for the achievable resolutions, for the processing speed, and for the quality of the results [98]. The pulse energy is, together with the focusing optics, responsible for the fluence in the ablation plane. The other main parameters are the cutting velocity, the number of cutting repetitions, and the focusing technique. Static focusing with achromatic or cylindrical lenses are used, which, in combination with a precise workpiece movement, enables to process large structured areas with constant properties. The line-shaped focus created by cylindrical lens provides an improved pulse overlap and fluence distribution, enabling to process straight cuts with higher quality and efficiency.
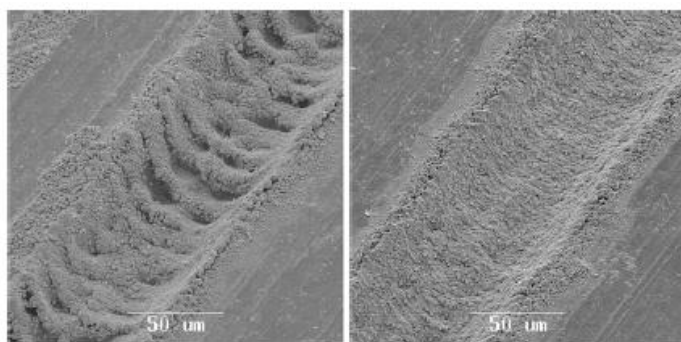
Fig. 1.16 Steel, processed with different pulse densities: left – 2 passes at 80 mm/min, right - 8 passes at 320 mm/min. Pulses energy - 800 μJ [98].

To achieve obvious differences in quality while still ablating nearly the same amount of material per time, the velocity of the workpiece movement and the number of these movements (cutting repetitions) can be adapted, when cutting material with short pulses, cuts are usually not made in just one step at low speeds but by cutting the same line several times at higher speeds. The difference is demonstrated in the following samples, all processed by focusing through an achromatic lens with a focal distance of 100 mm. Fig. 1.16 shows two cuts in steel, processed with an overall speed of 40 mm/min using pulses of high fluencies. The first line results from two slow processing steps, while the second one, which looks much smoother, was generated in eight processing steps at a higher feed rate. Although the appearance of the ripples in the first sample suggests a relation to an insufficient pulse overlap, the actual overlap per pulse is in the range of just 1 μm. Comparable periodic structures are often found at different, mostly rather low, feed rates and seem to develop in connection with ablated material that shields the surface from subsequent pulses when working with large overlaps. Due to a reflection behaviour of the material, these irregularities can then even increase during the next few sample movements. So while high feed rates (along with low pulse overlaps) are sometimes supposed to be disadvantageous, the results often prove the opposite − provided that a higher velocity is combined with a larger number of movement repetitions.
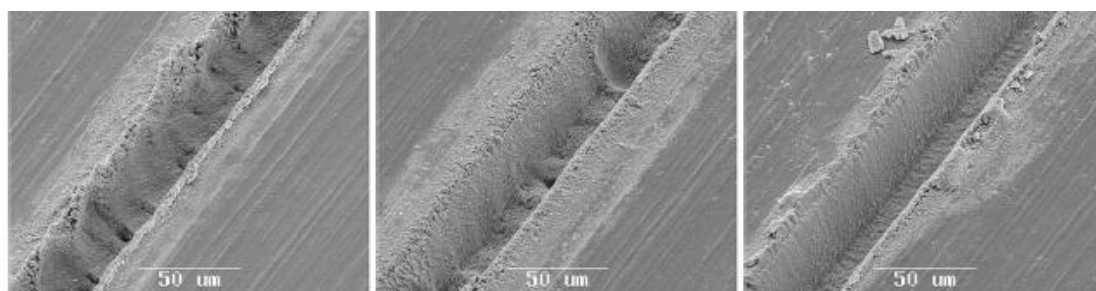
Fig. 1.17 Steel, processed 2x at 20 mm/min (left), 8x at 80 mm/min (middle), and 32x at 320 mm/min (right), using pulses of 100 μJ [98].

The next pictures demonstrate the same effect on deeper grooves. Fig. 1.17 shows samples processed with an overall speed of 10 mm/min using a low

laser fluence. When making 32 rapid workpiece movements, the kerf walls become much smoother than applying only a few slow processing steps. For straight cuts in metal, this behaviour is typical when working with ultrashort laser pulses.

It was reported [99-101] that gas injection changed the LIBS signal, the ejected material size distribution in an ablation plume as well as the ablation rate of steel.

1.4   Nanoparticle formation during femtosecond laser ablation

Various species are emitted by the target during fs-laser irradiation. As shown in Fig. 1.18, the images recorded by a CCD camera from the ablation of a Ti target indicate the presence of species with different velocities [102, 103]. First, at a very short time delay (Fig. 1.18a) a plume expanding along the normal to the target with a low angular distribution is observed. This plume is composed only of ions and neutrals. Their velocity reaches 3×10^4 m/s for atoms and 6×10^4 m/s for ions [104]. This plume is observed on any target material (insulating, semiconducting or metallic), and only weak differences are observed in the species velocity for different material. The classical explanation of this ion-neutral emission is based on the Coulomb explosion phenomenon [105, 106]. In the case of metallic targets, the ambipolar diffusion is proposed as a possible mechanism giving rise to the observed high-energy plasma plume component [107].

A second plume can be observed after a few µs delay (Fig. 1.18b) with a significantly higher angular distribution and lower velocity (a few 10^3 m/s). The nature of the species present in this plume was studied by optical emission spectroscopy, and the observed typical blackbody signal leads to the conclusion that this plume is mainly composed of clusters [76, 108]. SEM analyses of the film surface show the presence of a random stacking of NPs, whose size depends on upon the material and laser irradiation conditions [76]. Such SEM images are observed from any target material (metal, semiconductor or insulator), indicating that NPs emission is a characteristic

phenomenon resulting from the fs ablation. Actually, the major part of the matter emitted by the target during the fs ablation corresponds to the clusters, i.e. the atomic species represent a negligible amount of the emitted matter, in agreement with previous observations [48]. This conclusion has been checked by a careful examination of the angular distribution of film thickness (in the process of thin film pulsed laser deposition) and of the various species distributions deduced from the CCD images in [109]. A good agreement was found between the angular distribution of the NPs plume deduced from the CCD images and the film thickness spatial distribution. Only a few percent of the matter emitted by the target corresponds to atomic species.
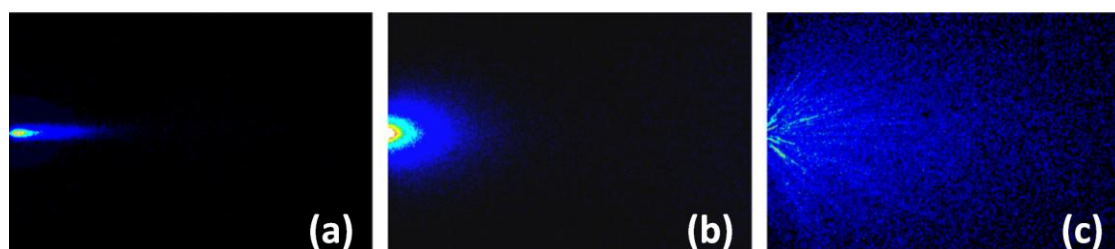
Fig. 1.18 CCD camera images of the plasma plume induced by fs-laser irradiation of a Ti target under vacuum. The images were recorded at 325 ns, 5 μs and 50 μs delays from right to left after the pulse [102].

The third population which can be observed (Fig. 1.18c) at longer delay (a few tens of μs) corresponds to droplets, which are easily recognized because of their luminous trajectories. Due to their low velocity and the high integration time for the image recording (i.e. a few tens of μs) they appear as lines. From such trajectories, an estimation of their velocity can be obtained (a few tens of 10^3 cm/s). Such droplets are only observed at high laser fluences (<15 J/cm^2). The SEM images of the films recorded in these cases show the presence of micrometre size particles at the surface of the films. It is important to note that these droplets do not correspond to 'big' clusters. Indeed, their size and velocities are different; their origin and formation mechanisms should therefore also be different. A possible explanation of the formation of the droplets based on the target stress confinement due to the ultrashort pulse laser

irradiation has been proposed [110]. The influence of the laser fluence on the emission of these various species was studied, and three laser fluence thresholds were determined for the emission of atomic species (E_a), clusters (E_c) and droplets (E_d), with the following relationship which holds whatever the target material:

$$E_a \approx E_c < E_d. \tag{1.15}$$

The generation of NPs during fs ablation has been studied mainly on simple elements and the results lead to the conclusion that their formation and emission occur directly from the target during a very short time (i.e. 50 ps after the laser pulse) [109], without any interactions with the atmosphere of the chamber (residual vacuum or injected gas). Rutherford backscattering spectrometric (RBS) and nuclear reaction analysis (NRA) analyses of the deposited films, however, showed the incorporation of oxygen in the films. These oxygen atoms come from the residual pressure in the chamber (10^{-5} mbar). Such oxygen incorporation could be due to NPs oxidation during the plume expansion. Further analyses on films grown by fs ablation lead to the conclusion that the oxygen atoms could take part in the formation process of NPs. In addition, fs-laser ablation of a polyatomic target does not inevitably lead to the formation of NPs whose composition respects the target composition. It can be concluded that separation of phases, atomic movements and chemical reactions have to occur during NPs, and this cannot be investigated in the framework of an aggregation, homogeneous nucleation or pure fragmentation-based mechanism for fs-laser ablation.

In another study [111] the NPs size fractions emitted during ablation with ps-laser pulses were compared with those released during fs-laser ablation for steel, zirconia and brass. At the same pulse energy, fs-pulses release a similar share of NPs (> 80 %) in the aerosol fraction. Ablation with fs-pulses generates a far higher share of ultra-small (7 nm) sized particles during machining of metals and ceramics (Fig. 1.19). The maximum quantity of NPs corresponds to

the particle size of 50 nm independently of the ablated material and applied pulse duration.
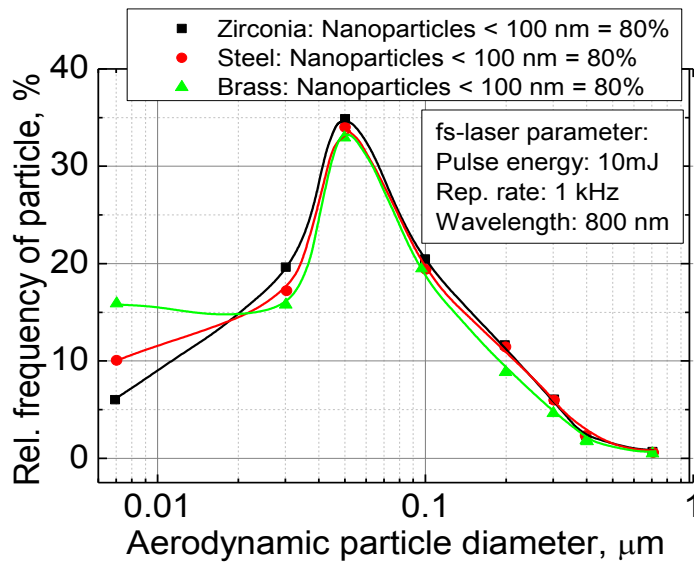
Fig. 1.19 Particle size distribution during fs-laser ablation (10 μJ) of steel, brass and zirconia [111].

1.5   Ablation of absorbing materials in water

Non-transparent materials are typically cut and drilled by front-side direct ablation techniques [75, 98, 112-114] in air or inert gas atmosphere, which often suffer from a lack in fabrication throughput and end-quality of the machined samples.

These problems can be successfully addressed when laser processing under thin transparent liquid layer is used. The first experiments on materials machining under water and other liquids started as early as 1975. At that time lasers with a long pulse duration of 10-100 ns were used. A comprehensive review of those investigations is presented [115, 116]. The effect of the liquid on laser etching depends on the material and processing parameters. When laser etching is done in a liquid, debris is carried away due to liquid flow, bubbles and thermal convection. It was concluded that water-assisted laser processing could be applied to etching, cutting, hole drilling, surface cleaning and laser shock processing. Sano et al. [117] found an improvement in residual stresses from tensile to compressive by underwater laser irradiation. They reported that the formation of high-pressure plasma on the surface of the

sample was due to the impulsive pressure of the laser induced plasma generated by the interaction of the intense but relatively long laser pulse with the material. In [118] is reported that laser ablation rate of silicon using a KrF excimer laser drilling is highly enhanced by water assistance. They proposed that a higher pressure is induced once the plasma is generated in the water confinement region that results in a higher ablation rate. Dupont et al. [119] studied and compared the ablation rate of stainless steel with a broad range of fluences and various wavelengths in air, under an argon atmosphere and under transparent flowing water film with ns-pulses. They found that the efficiency of the ablation in water increased by a factor of 2 - 15 for a certain incident power densities. Peripheral oxide redeposition was absent using the water film. He speculated that the ablation yield increase was caused by the confinement of the plasma within a transparent water layer. Water prevents the expansion of the plasma upstream of the target and intense pressure pulse is reflected back to the ablation area. Similar ablation yield increase have been found for alumina and silica. These works show that underwater laser processing has the cooling effect, which effectively reduce the size of HAZ. Both the efficiency and quality of the laser machining can be greatly improved.
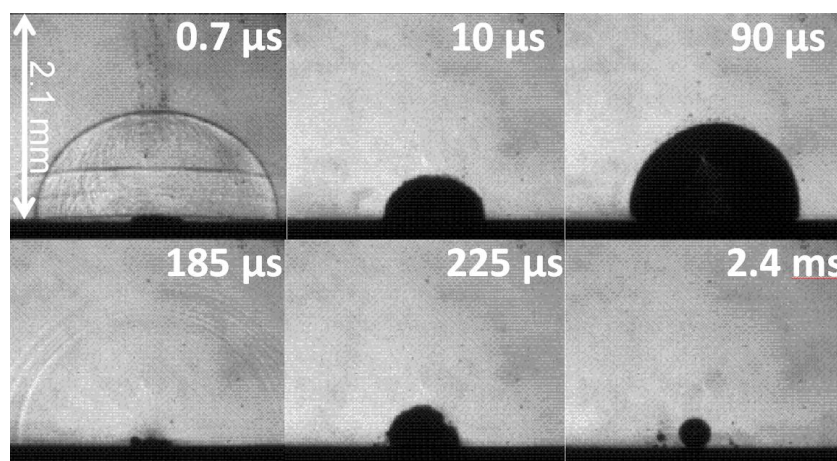
Fig. 1.20 Snapshots of cavitation bubbles at various delay times after the irradiation of a laser pulse onto a Ti target (black bottom line) immersed in water at an ambient pressure [120, 121].

The behavior of a cavitation bubble induced by laser ablation of titanium target in water have been investigated with shadowgraphy in [120-122]. Fig. 1.20 shows images observed at various delay times after the irradiation of the laser pulse (10 ns, 22 mJ/pulse). The origin of the delay time is defined as the moment of plasma detection by CCD camera. At 0.7 μs delay a spherical shock wave originated from the ablation point is seen, which propagated with the sound velocity in water. In the case of Al target, this spherical wave additionally has cone-like wings. Another wave, which had parallel wavefront to the target surface, was excited by mechanical vibration of the target. The birth of a cavitation bubble is also seen. The cavitation bubble expanded at next delay time (10 μs), and the maximum bubble size was observed 90 μs. The shape of the cavitation bubble is not a sphere but an oblate spheroid. The bubble shape may be affected by the surface tensions of the interface. After reaching the maximum size, the cavitation bubble shrinks, collapses and the second shock wave is observed at 186 μs delay. Immediately after that, the second cavitation bubble is formed (225 μs). The shape of a second bubble is not spherical as well. The expansion and the shrink of the bubble were irregular. However, the final shape of the stably formed bubble was a perfect sphere as observed at 2.4 ms delay.

Recently [123] Nd:YAG laser based microchanneling technology, which is probably a most widely used process for fabrication of polymer-based microfluidic device, have been adopted to be used with water layer. Underwater laser processing has resulted in minimization of undesirable effects of laser processing like heat affected zone and redeposition around the microchannels resulting in cleaner and finer structure than open air processing. Even CW lasers benefit from the thin water layer impact on the ablation process. Yan et. al. in [124] micromachined alumina with a CO_2 laser under thin water layer and found the promising result in reducing substrate defects such as recast layer, dross, cracking and heat damages that are typically found in machining in air. The microstructures of the machined region were

demonstrated to reveal different heating and cooling processes during laser machining in water and air. The experimental results indicated that the machined kerf width was strongly affected by the water layer thickness, whereas the kerf depth was controlled by both the laser pass number and water layer thickness.

Fs ablation have been studied under sprayed thin water film and its influence and benefits compared with the ablation in the air [125]. It was found that water indeed enhances the ablation rate and in some situations makes possible to ablate the holes in silicon with a higher aspect ratio. While ablating the grooves in stainless steel, the water spray allows using the high fluences without the generation of the self-organized structures, when fs-laser pulses are focused inside the layer of the transparent media, after certain propagation length the laser beam self-focusing and filamentation occurs as a consequence of the dynamic balance between positive Kerr nonlinearity of the material and negative defocusing effects in the electron plasma generated through the ionization process. Nonlinear fs beam transformation in water was studied in [126-128]. Filamentation phenomena are not new and have many applications including beam spatial self-compression and self-stabilization [129], supercontinuum generation [130], lightning control [131], terahertz radiation generation [132] and more [130]. More detailed information regarding light filament formation and propagation theory in liquids, as well as its assisted rapid fabrication, may be found in [128, 130, 133]. However, only recently it was shown that fs light filamentation in a thin water layer gives the new possibility to effective micromachining of fragile, heat-sensitive transparent materials such as glasses with high precision and good quality [134, 135]. The intensity in the filamentary region increases high enough to cause nonlinear multiphoton absorption even in high bandgap materials, such as sapphire, and calcium fluoride. Consequently, ablation process on the surface of sample starts with material removal rates exceeding ablation rates in the air in times, at least in the case of borosilicate glass.

Water-assisted particle removal with the lasers is also employed in the semiconductor industry to clean silicon wafers from submicrometre particles, where the strong adhesion forces make usual cleaning methods such as wet chemical, wiping, scrubbing, gas or fluid jet, ultrasonic and other merely inefficient [116].

The formation of fine particles has been observed by many researchers during laser machining of solids in water by short and ultrashort laser pulses [136]. Laser irradiation of solid targets in water has been used to fabricate Ag, Au, Ni, Cu, C, Si and other nanoparticles [137-141]. Micro particles suspended in water may also be further reduced in size by laser irradiation [136, 142, 143]. This treatment narrows the size distribution because larger particles absorb more light.

The formation of nanoparticles within the laser-induced cavitation bubble is studied in situ using small angle X-ray scattering with high spatiotemporal resolution in [103]. Directly after laser ablation, two different particle fractions consisting of compact primary particles of 8-10 nm size and agglomerates of 40-60 nm size are formed. The abundance of these species is strongly influenced by the dynamics of the oscillating cavitation bubble. Primary particle mass is most abundant during maximal expansion of the first bubble and reappears a little weaker in the rebound. In contrast to this, the mass abundance of agglomerates is relatively low in the first bubble but strongly increases during first bubble collapse and following rebound. Although most of the ablated material is trapped inside the bubble and follows its oscillation, a minor fraction of both species could be detected outside the cavitation bubble even before its final collapse and NPs dispersion in liquid.

In short, water assisted ablation [107-109, 114-120] is advantageous in following ways: e.g. axial translation is not required while several-millimetres deep structures can be fabricated, additional cooling is provided due to the added water layer, which prevents temperature and tensile stress gradient formation, toxic ablation nanoparticles are stopped from diffusing into the air.

Temperature-induced tensile stress is particularly a problem for micromachining brittle materials since absorption of the beam's peripheral region and plasma-material coupling [118] leads to local heat build-up and ultimately to cracking and shattering of the samples. Due to the ablation processes occurring in water, cavitation bubbles emerge and prevent ablated particles to stick to the sample surface and thus diminish debris redeposition on the samples [35]. Moreover, the system is comprised of only a few components, remaining simple, which makes it easy to use. Since a water layer is added on top of the samples, additional degrees of freedom arise in terms of optimization.

1.6   Energy-dispersive X-ray spectroscopy

Energy-dispersive X-ray spectroscopy can be used to characterize elemental composition of laser ablated samples. The essence of this technique relies on the unique atomic structure of every element producing a unique set of peaks in its X-ray emission spectrum. The sample is bombarded with a focused high-energy beam of charged particles (e.g. accelerated with high-voltage thermal electrons), which excite an electron in an inner shell, ejecting it from the shell while creating a vacancy in its place. An electron from an outer higher-energy shell then fills the gap, and the energy difference may be released in the form of an X-ray photon. The number and energy of such photons from a specimen is measured, and from such spectra, the elemental composition is determined. A more detailed information can be found [144-149].

2. Groove fabrication using micromachining system based on high repetition rate femtosecond laser and linear positioning stages

Material related to this part of the dissertation was published in European Patent [P1], articles [A1-A2] and proceedings [C1-C2].

The aim and the first step of this part of the dissertation are the development of a fs-ablation technology for producing well-defined microgrooves in steel that could be used in a prototype of continuous structural health monitoring sensor. The achievement of the stated aim started with the development of the laser micromachining system based on the high (hundreds of kHz) repetition rate fs-laser, beam transportation, manipulation and focusing system capable of producing smooth walled grooves on the surface of the steel.

The works that were done can roughly be split into the following parts:

1. Selection of optical components for beam delivery and focusing systems and their setup, including beam attenuator, beam telescope, adjustments iris, polarization rotator, harmonics module;

2. Selection of appropriate components for the micromachining system (hardware tools, positioning system, software tools);

3. Setup of the real time on-axis observation system to visualize the fabrication process;

4. Setup of the micromachining system ventilation system to get rid of the ablation process waste;

5. Research on different software available for the experiment automation;

6. Beam scanner integration within the micromachining system to implement „moving beam" approach;

7. Numerous experiments to find proper fabrication parameters in terms of focusing optics, beam scanning speed and algorithm, etc, as well as laser parameters such as pulse energy, wavelength and intensity distribution.

The specific scientific objective of this study is centred on research work related to ultrashort laser ablation process with different radiation parameters such as wavelength, pulse energy density, spatial pulse shape and repetition rate in the first place on stainless steel. The technological objective was defined as follows: to find optimal ablation process parameters for forming well depth-controlled grooves in steel and aluminium with a width of 80-300 μm and an aspect ratio in the range of 0.5 – 1.5, a deviation from designed width and depth of no more than 5 %, steepest available wall inclination angle and processing speed and quality suitable for industrial applications.

2.1 Micromachining system based on femtosecond laser and linear direct-drive servomotors stages

This part of the dissertation describes the micromachining system, designed and built by combining the most advanced high-technology solutions to enable the microfabrication of various materials. It integrates a Yb:KGW fs-laser, harmonic generator, motorized optical power attenuator, precise 3-axis object positioning system, galvoscanner, beam analysing subsystems including power meter and CCD camera, beam polarization rotator and machine vision. The main system components and optical scheme are described below.

### 2.1.1 Femtosecond pulse laser

Ultrashort pulse duration, high pulse to pulse energy stability, good beam quality and high repetition rate are the desired laser-beam features for reliable micromachining. The recent development of fs high-average-power and high-repetition-rate DPSS bulk ytterbium doped crystal and fiber-based lasers opened up new opportunities for much faster and precise micromachining. Pharos [150] laser from Lithuanian Light Conversion Ltd. [151] was selected to fulfil the required micromachining tasks. The key features of the Pharos laser are:

- ➢ Pulse duration: 80 fs after oscillator and 270 fs after amplifier;
- ➢ Pulse energy depending on pulse repetition rate can vary from 20 μJ to

400 μJ (2014 year version) with RMS stability of 1 %;

➢ Average power up to 20 W (2014 year version);

➢ Flexibility in repetition rate: from single-pulse to 1 MHz;

➢ Rugged mechanical design with sealed modules replaceable on the field.

"PHAROS" laser is built upon the traditional CPA technique, employing a seed oscillator, regenerative amplifier and pulse stretcher/compressor modules. The Kerr-lens mode-locked oscillator, typically delivers > 700 mW output with sub 80 fs pulse duration. The regenerative amplifier is based on Yb:KGW medium as well, which is non-collinearly pumped by several high-brightness diode bar modules delivering 60 W of pump power each. BBO Pockels cells supported the operation of the amplifier and optional pulse picker in the first models up to 200 kHz, and later extended up to 1 MHz. The stretcher/compressor module is based on a single transmission volume Bragg grating exhibiting high efficiency (~90%) and excellent power handling capability. The timing electronics control the operation of Pockels cells and provide protection against optical damage of the laser crystal by high-intensity pulse. Maximal pulse energy for standard systems is up to 0.3 mJ and can be increased up to 1 mJ using an optimized cavity design. Output pulse duration after regenerative amplifier is typically 270 - 300 fs.
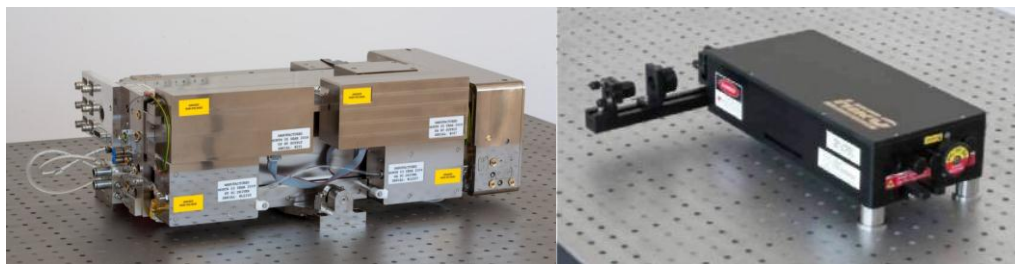
Fig. 2.1 High-power Yb:KGW laser (left) and frequency conversion module (right).

By using SH generation and sum frequency generation phenomena, it is possible to achieve frequency doubling, tripling and quadrupling of the Pharos laser radiation. As a reasonable "single box" solution for harmonics generation at high repetition rate (up to 200 kHz) frequency conversion module "HIRO" [152] (from Light Conversion) was used for second and third harmonic

generation at 515 nm and 343 nm wavelengths. The views of the Pharos laser and frequency conversion module are presented in Fig. 2.1.

2.1.2   3D positioning system based on linear servomotors stages stages

The concept of "moving part" while keeping the laser beam focus at a fixed position was considered to be the first option concept for the micromachining system development as it is suitable for micromachining virtually any structure on a flat as well as on more complicated surfaces. In order to achieve the submicron sized structures by laser micromachining, appropriate resolution of the positioning system must be ensured. To ensure all requirements, the 3D linear stage system from Aerotech Inc, USA [153] was employed for applications in micromachining of samples. The system consists of three linear stages ALS130 and ANT-4V that allow fast and accurate sample positioning. In our case, the accuracy of XY stages was about 300 nm. Also, the maximum travel speed for these tables is 300 mm/s and the travel distance is 150 mm. More details about the specification of the 3D positioning system are provided in [154] for x and y stages and in [155] for z-lift stage.

2.1.3   Controlling software

In order to control hardware devices such as a laser and linear stage systems, the System Control Application (SCA) [156] software (from Workshop of Photonics [157]) was used. The SCA software provides a platform for automating laser micromachining experiments. It is capable of 3-levels of simple-to-complex microfabrication, where, at the basic level, a WYSIWYG equipped GUI is able to convert vector motion paths stored in "*.plt" files as well as raster images stored in "*.bmp" bitmap files into complex positioning trajectory information without the need for G-code programming. Moreover, SCA can be used to program complex multiplex trajectories using user-defined constants, variables, complex mathematical expressions, conditions and code cycles. In this way, various algorithms can be realized, and overall automation of the micromachining laser setup is possible. SCA also gives multiple possibilities to connect and use different hardware, such as CCD camera,

stepper motor, power/energy meter and other equipment to automate the algorithm. At the highest level, microfabrication code may also be written directly in C++ and C# languages. The software supports the Aerotech and Scanlab scanners hardware.
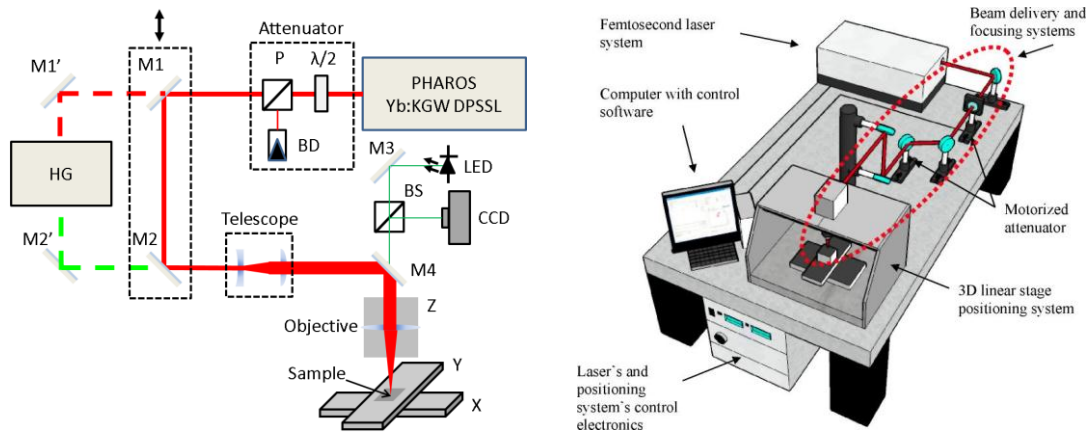
Fig. 2.2 Optical scheme of the experimental setup with the XYZ linear stages (left) and CAD model view of the whole micromachining system based on the femtosecond laser and linear direct-drive servomotors stages (right). λ/2 – zero order half-wave plate, P – thin-film Brewster-type polarizer, BD – beam dump, M1-M4 – dielectric HR mirrors, BS – beam splitter, HG – harmonic generator, LED – illuminating light diode, CCD – process vision CCD camera.

2.1.4   Assembling the optical system

All the above-mentioned components were integrated into a single micromachining system schematically depicted in Fig. 2.2. Note that not all elements are depicted on the CAD model view; however, it represents an overall overview of the micromachining system. Using ultrashort pulses sets additional requirements for the optical system. Known nonlinear effects such as self-phase modulation, nonlinear absorption, filamentation and optical damage may arise in the optical system components during the laser-matter interaction: therefore refractive optical components are avoided if possible. In order to withstand high-intensity, multiple layer dielectric mirrors were selected for delivery of the laser beam towards the sample. The beam diameter of the non-focused beam was about 3.5 - 4 mm and the clear aperture of the optical components was selected to be 1". The third parameter of great importance is the beam diameter on the target plane. For processing of large and

curved samples, as well as for avoiding pollution of the lens by ablated material, a long working distance is also a desired feature for the focusing optics.

The laser beam possess through the optical attenuator consisting of a λ/2 phase wave-plate mounted on a motorized rotation stage in combination with a reflective thin-film Brewster-type polarizer. The laser output is linearly polarized with high contrast, which gives the possibility to use this light characteristic to control its power. The beam is then directed towards the telescope which expands the beam to fill the focusing optics aperture. This assures the minimal spot diameter in the focal region.

2.2   Samples used in experiments

The metallic samples for micromachining experiments were provided by partners from Matrican (Santander, Spain) [158] and Muggler (Denmark) [159]. Matrican functioned as an advisor in the choice of materials and their treatments as it has 35 years of experience in the field of steel manufacture/production. The hardness chosen is the one traditionally used for the manufacturing of various hard work tools. E.g. selected steel is used for the manufacturing of plastic extrusion moulds. These pieces used in injection moulding machines during their everyday work suffer severe abrasion. Used steel (Sverker 21, No. 1.2379 [160]) is a carbon and chromium rich, possessing molybdenum and vanadium tool steel with high surface hardness estimated to be 600-700 Vickers. A chemical composition of the consisting materials is provided in Table 2.1. It was verified with energy-dispersive spectroscopy.

A good wear resistance, dimensional stability and high resistance to tempering effect make this steel suitable for heavy duty work. The following steels were used for experiments in the shape of sheets with dimensions 50x50x10 mm (Fig. 2.3), cylinders and complex shapes (data provided by manufacturer):

- Sverker 21 No. 1.2379 steel tempered at 54-56 HRc;
- Sverker 21 No. 1.2379 steel not tempered, 25 HRc.

A part of characterization work (hardness measurements, SEM, EDS, optical microscopy), has been made in cooperation with partners from University of Bath (Bath, UK).

Table 2.1 Chemical composition of materials used.

Chemical Composition in Weight % of steel No. 1.2379 [160]					
C	Si	Mn	Cr	Mo	V
1.53	0.35	0.40	12.00	1.0	0.85
Chemical Composition in Weight % of aluminium alloy EN AW-5083 [161]					
Al	Mg	Mn			
94.8	4.5	0.7			
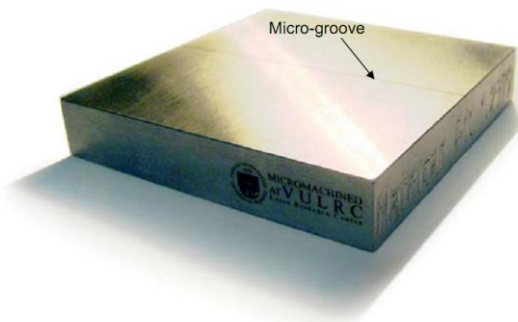
**Fig. 2.3 A steel block micromachined by laser.**

The second material, where the wear measurements are of great importance, is aluminium. The used aluminium alloy was EN AW-5083 [161]. The performance of the laser processing systems was verified on the steel sheets, plates, and rods as one shown in Fig. 2.3.

2.3 Steel ablation threshold

The geometry (width and depth) of an ablated crater produced by laser pulses of a given peak fluence is a function of the ablation threshold of the material. In order to ensure sufficiently effective laser micromachining process, it is necessary to exceed the material ablation threshold. Therefore, the ablation threshold is a very important parameter for the precise control of the geometry of processed structures. In general, the threshold value F_{th} can be interpreted as a value which depends on the particular laser parameters (such as wavelength, pulse duration and density) used.

Fig. 2.4 shows the extrapolation curves and measured threshold values (F_{th}) at various pulse repetition rates and incident pulse numbers. It was found

that the pulse repetition rate does not have an important role on the threshold value, at least in the tested frequency range (25-300 kHz). At low repetition rates (25 kHz), the threshold value was higher (0.35 J/cm^2), while at higher rates the value slightly decreased (~0.25 J/cm^2 at 300 kHz). However, taking into account the measurement accuracy, which was ~ 20 % (arising primarily from the estimation of focal beam diameter), it can be stated that ablation threshold value does not depend on the pulse repetition rate at least up to 300 kHz.
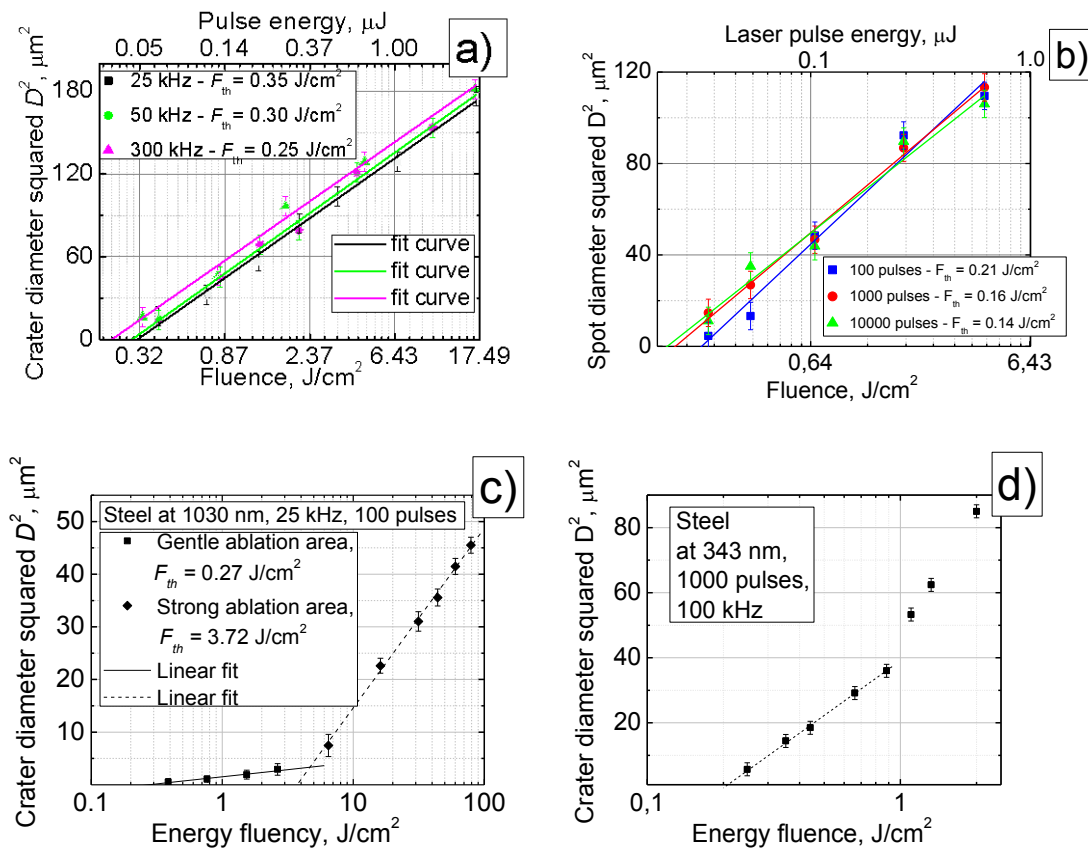

Fig. 2.4 Crater diameter dependence on pulse energy fluence a) at different pulse repetition rates (steel); b) at various incident pulse numbers (aluminium); c) "strong" and "weak" ablation phases (steel at 25 kHz); d) at 343 nm (steel at 100 kHz, 1000 pulses).

This assumption was verified by measuring the ablation threshold on different material, in this case, aluminium. No pulse repetition rate influence on the threshold value was found on aluminium either. However, the incubation effect is present in both materials and by affecting the same spot

68

with a higher number of pulses; the threshold can be slightly reduced (from 0.21 J/cm^2 for 100 pulses to 0.14 J/cm^2 for 10000 pulses at 100 kHz for steel). This decrease though is too small to have a significant impact on the efficient ablation ratio, especially when large areas have to be ablated.

It is known that, depending on the laser fluence, two different ablation phases exist: "gentle" ablation appears at the fluences close to the ablation threshold, while "strong" ablation is prominent at higher fluences. By analysing the ablation rates, these two ablation regimes were determined for the steel sample and are shown in Fig. 2.4c. The threshold for the "weak" ablation is 0.27 J/cm^2 while the "strong" ablation regime begins at fluences above ~5 J/cm^2 with the ablation threshold of 3.7 J/cm^2. The ablation rates in the "strong" regime are higher, and only this regime is suitable for efficiently cutting relatively deep (>50 μm) grooves reasonably quickly. However, it was found that the ablation rates in this phase strongly depend on the laser processing parameters and sample translation speed.
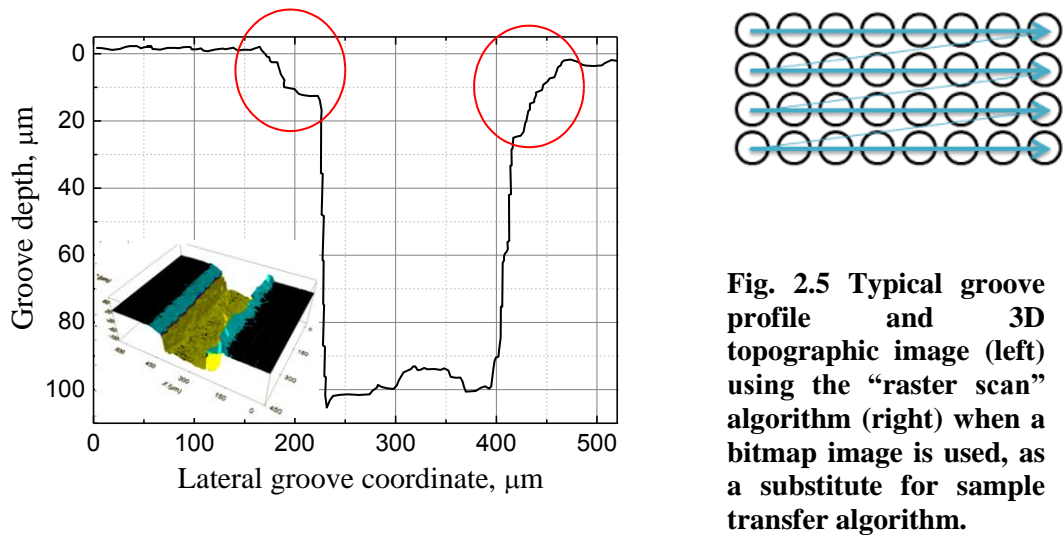
Fig. 2.5 Typical groove profile and 3D topographic image (left) using the "raster scan" algorithm (right) when a bitmap image is used, as a substitute for sample transfer algorithm.
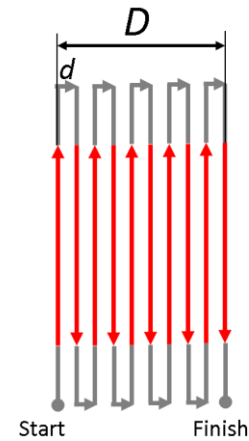
The ablation threshold for the mould steel was also determined for femtosecond pulses at 343 nm wavelength, which is the third harmonics of the fundamental laser wavelength. The conversion was achieved with two BBO crystals, and overall conversion efficiency was approximately 25 %, so 2 W of the fundamental radiation resulted in 500 mW at 343 nm. The maximum power

was reduced due to the cost of the photon energy, conversion inefficiency as well as Fresnel reflection losses. The ablation threshold in the steel sample measured at this wavelength was $0.2 \, \text{J/cm}^2$ and was close to the ablation threshold at 1028 nm. This was important for groove microfabrication with fs-pulses at 343 nm.

2.4   The patterning algorithms

Experiments showed that the rectangular groove with a 200 μm width could not be micromachined in one or several passes using a long focusing distance lens (>0.75 m) with the beam focused down to a diameter of 150 - 200 μm at $1/e^2$ level. In such low NA focusing conditions, the beam lacks the fluence for the strong ablation regime (available fluence was up to $0.3 \, \text{J/cm}^2$, which corresponds to the gentle regime) and produces only 10 - 20 μm deep trenches in one pass with maximum laser energy, which is too shallow. Repeating the exposure multiple times does not solve the problem because the depth saturates under 100 μm with many repetitions, and the resulting groove has a very pronounced unacceptable "V"-shape. For micromachining of rectangular grooves with steep walls, the strong ablation regime must be achieved. This can be accomplished with focused beams when the beam diameter is reduced to values smaller than the required groove width. A beam having 10 to 50 μm at $1/e^2$ intensity level at the focal plane was found to be suitable for forming a groove with a width of 200 μm when some patterning algorithms are used.

Fig. 2.6
Hatch algorithm.

Fig. 2.7
Spiral algorithm.

The so-called "raster scan" (Fig. 2.5) was tried first. The laser beam was focused with 25 mm focal length AR coated fused silica lens. The irradiation resulted in a groove with a relatively good shape. However, this approach
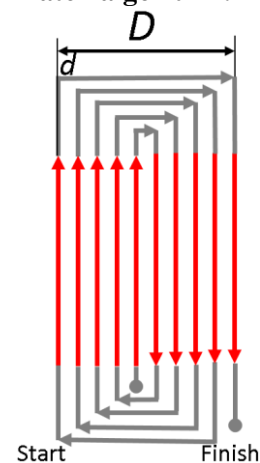
deteriorates the upper edges of the groove (see Fig. 2.5), which become damaged, rounded, and a significant part of the surface near the actual groove is affected. This result may be coming from the sophisticated control software algorithm, which translates and scales the bitmap data (50x1250 pixel) to the actual coordinated linear stages with the sample movements and the laser on and off actions.

Next, the several hatching algorithms were tested. The resulting one line groove (not shown here), made on the surface of polished stainless steel by exposing the sample once resulted in an average 10 μm width at 5 % depth. Focal width was estimated to be not less than 3.4 μm. In those conditions, laser fluence could reach high levels of up to several hundred J/cm^2 with available average laser power. However, such fluence was too high and led to significant melting at the groove bottom. Laser parameters were adjusted for optimization purposes. As groove steepness is essential, tight focusing condition is preferable. In order to fabricate thicker structures, a number of ablation repetitions and special scanning patterns must be applied. The results from conventional hatch algorithm (Fig. 2.6) and the spiral algorithm (Fig. 2.7) are presented. With the hatch pattering, broad grooves are formed by continuously adding new grooves side by side by some separation factor *(d)* in one direction, while with the spiral algorithm new grooves are added in both directions. After proper optimization of parameters, both algorithms resulted in grooves with sufficient depth. As the fabrication was performed at a strong ablation regime ($E = 15$ μJ, $f = 100$ kHz, $F > 80$ J/cm^2), a huge amount of ablated particles was generated. The structure produced with the conventional hatch algorithm was asymmetrical because the majority of the ablated particles tend to stick to one side of the wall (Fig. 2.8 left profile) at the end of the micromachining process.

This can be understood by comparing the ablation conditions of the first line with respect to others: the last ablated line tends to pollute the previous ones. To get deeper grooves, several repeating scans are necessary, and this debris accumulation becomes more evident. The spiral patterning shows better

results in terms of wall steepness and groove rectangularity. However, at the centre of the bottom surface of the fabricated groove, a hill was observed (Fig. 2.8 right profile). Most probably, the hill was formed from stuck microparticles. Those formations are particularly hard to remove, remaining even after cleaning the sample in an ultrasonic bath for one hour.
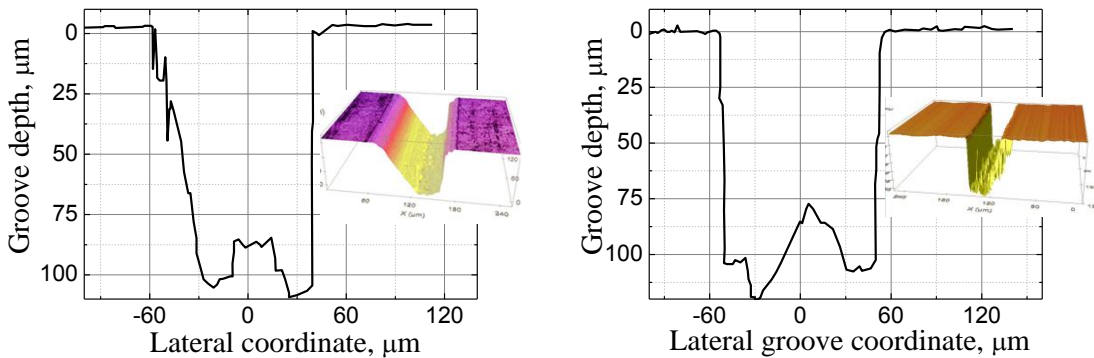

Fig. 2.8 Typical groove profile after the hatch (left) and spiral (right) algorithm pattering. For the spiral pattering algorithm, the groove slopes are more symmetric and steeper, however, debris is accumulated at the bottom of the groove.
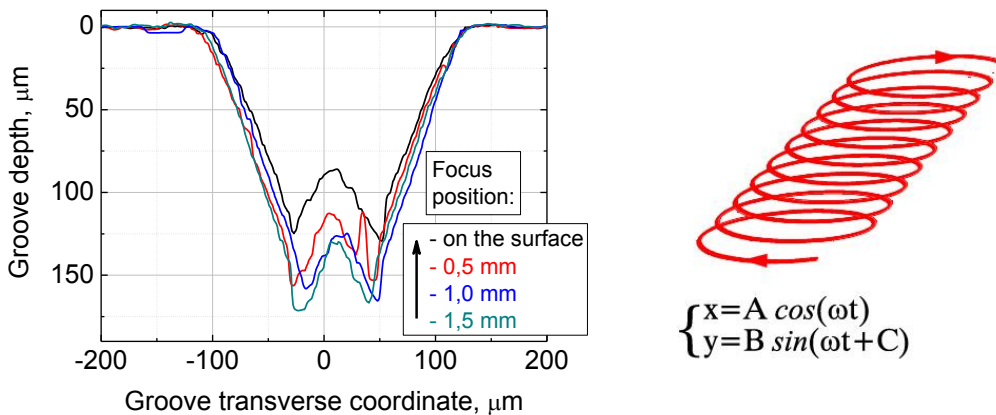
Fig. 2.9 Typical profiles of the grooves made with the galvoscanner with the circle spiral algorithm. Pulse repetition rate was 50 kHz, the algorithm consisted of the spiral written as a parametric function. The algorithm was repeated five times with 500 mm/s positioning speed. The focus plane in respect to sample position was changed. Laser power was 2 W.

Experiments to determine the optimal groove-to-groove separation distance *(d)* were also carried out. It was found that at least 50 % and no more than 80 % of the ablated region should overlap in order to get smooth-bottom

structures with a minimal bottom roughness. Such an overlap ensures that the bottom surface has no signs of the spatial frequency used in the algorithm. More specifically, the bottom boundary already reveals individual lines from the hatching algorithm, while the upper boundary makes the bottom surface of the groove more pronounced to deep holes and other irregularities, as was also revealed in other studies [113, 162].
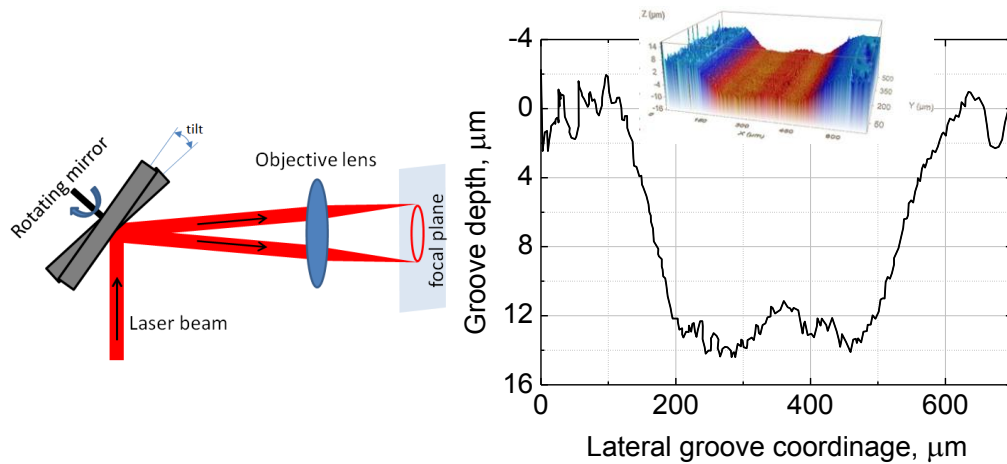

Fig. 2.10 Rotating mirror scanning approach (left) and the groove achieved with this method (right).

Further, the circular spiral algorithm was investigated. Here, the sample was translated according to the parametric equation. In this experiment, after finding the preliminary parameters resulting in definite groove dimensions (see Fig. 2.9), the focal position was changed with respect to the sample surface. All the grooves resulted in a "W" shape, not really suitable for wear sensor application. The result could probably be optimized by changing the variables of the parametric motion equation and other experimental parameters; however, without optimization the algorithm produced unsatisfactory and unacceptable results.

The "rotating mirror" approach was also tested. In this method, before focusing, the laser beam is reflected from the dielectric mirror, which is rotated with a slight (1 - 5°) tilt (see Fig. 2.10). Ideally, this would result in a circle scanning motion in the focal region, and additional perpendicular linear sample

movement would result in a groove ablation. The width of the groove could be controlled by the tilt of the mirror, whereas the depth is controlled by the sample translation speed. However, although this approach could significantly reduce the micromachining costs, as it requires neither expensive 3D motion control nor a galvoscanner, it does have major drawbacks. The grooves fabricated with this approach were asymmetric. The morphology depended heavily on the sample movement direction. Only in two parallel directions, the symmetric groove profile was obtained, as shown in the part of Fig. 2.10. Although the concept was proved to be correct, and the grooves can be fabricated with this method, it is difficult to control the groove width by the convenient tilt changing of the mirror. The achieved groove was too wide.

Next, the so-called "wobbling" algorithm (Fig. 2.11) was tested by changing the sample movement speed. Obviously, with lower sample speeds higher pulse densities resulted in deeper grooves. However, any parameter set within this motion path resulted in a wider than programmed "W" shaped groove and was also not optimal for wear sensor needs.
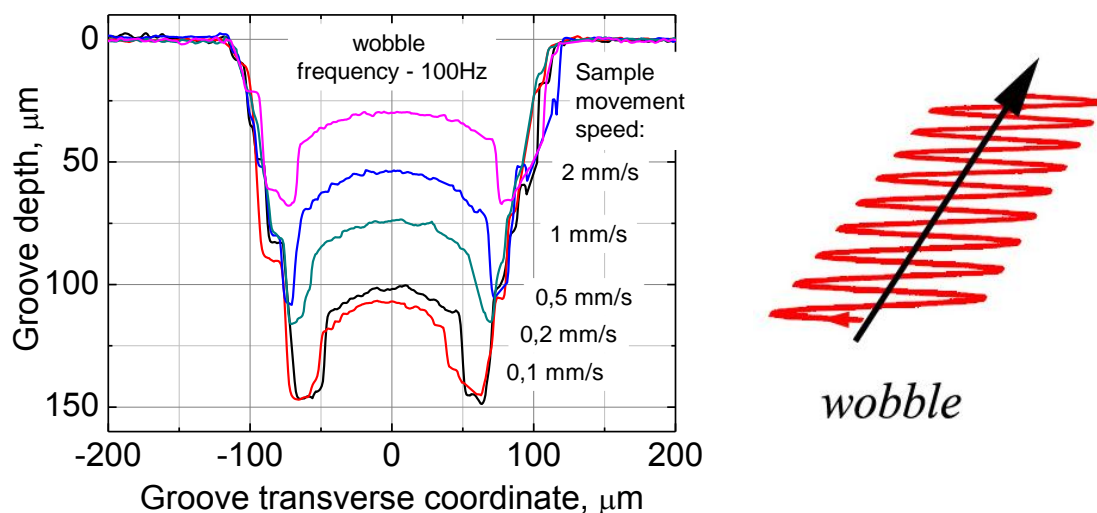
Fig. 2.11 The dependence of the groove morphology (left) and depth within the wobbling scanning algorithm (right) on the sample transfer speed. The algorithm was repeated 20 times; the wobble frequency was 100 Hz; amplitude corresponds to the groove width of 200 µm.

2.5 Reduction of the groove manufacturing time

By using tight laser beam focusing, many algorithm scans have to be performed in order to achieve the required groove depth with acceptable bottom surface smoothness and roughness. The micromachining algorithm consists of many motion lines. Therefore, the linear stage axis does many stops in-between. The limiting factor here is the acceleration and deceleration time of the linear stage axis causing machining delays because of the inertia of the sample and moving linear stage axis. Furthermore, only a small fraction of laser power can be used when moving slowly. This result in prolonged processing time required for a single groove and inefficient use of the laser power.

Table 2.2 Optimization of the micromachining time – new focusing approach.

Parameter	Earlier experiments	New experiment
Focal length of focusing lens	25 mm (sharp focusing)	150 mm (loose focusing)
Focused beam diameter ($1/e^2$)	~10 μm	~50 μm
Usable power of the laser at energy fluence 2 J/cm^2	~0.08 W	~2 W
	Laser / Beam at focus:	

Table 2.3 Typical time consumption dependence on a number of scans by using the "moving sample" approach.

Number of repetitions	Translation speed			
	1 mm/s	10 mm/s	50 mm/s	100 mm/s
1	3 s	2 s	1 s	1 s
5	13 s	6 s	5 s	4 s
10	25 s	13 s	11 s	8 s
50	124 s	50 s	45 s	45 s
100	248 s	110 s	107 s	98 s

After careful analysis of the situation, an improved concept aiming to boost the process and optimize the processing time was developed. Actually,

two concepts were tried out. The first one was the optimization of the "moving sample" approach by increasing the focal spot of our laser beam when moving "slow". Secondly, a series of tests with a fast "moving beam" by using galvoscanners were performed. In the first case, the focus spot was increased from ~12 μm, (previously 25 mm focal distance lens) to ~50 μm (with 150 mm focal distance FS lens). Parameters listed in Table 2.2.

Experiments confirmed that by using the new focusing regime micromachining time can be reduced. The focusing with lower NA lens allowed using fewer scan lines in the spiral algorithm. Table 2.3 shows the typical time consumption for producing a single 1 cm length 50x50 μm groove: the number of passes needed is approximately 100. Focusing with lower NA lens can speed up the micromachining process by reducing time consumption; however, the shape of the groove is getting worse (right part Fig. 2.12), looking more like a "V", as mentioned previously.
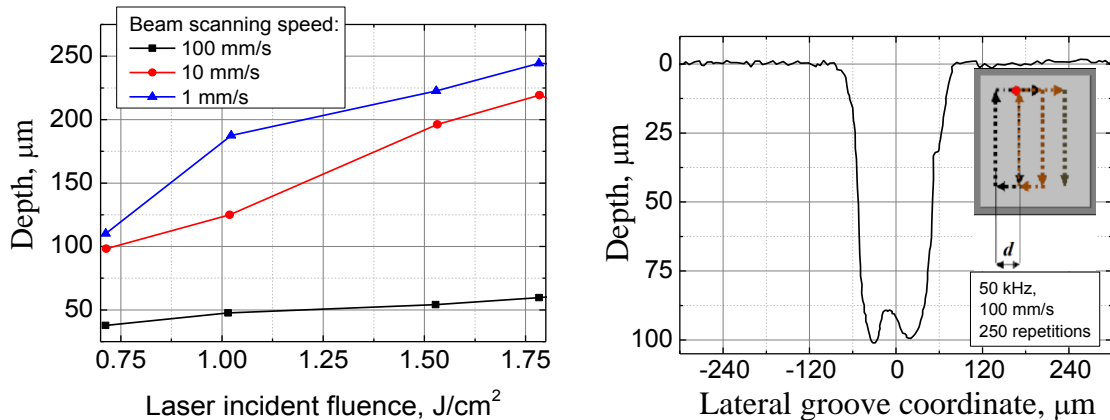
Fig. 2.12 The groove depth dependence on the laser beam fluence (left). The groove was ablated in the steel sample with the spiral algorithm, which was repeated 250 times. Each line describes a different sample scanning speed; a typical profile of the groove in steel sample machined with the new focusing approach when the laser beam fluence was ~1.85 J/cm² (right). The scheme also shows sample moving algorithm.

2.6   Ablation with pulses at 343 nm wavelength

A comparative experiment was performed at a shorter wavelength by using the most successful algorithm with the "moving sample" system. As

described before, the gentle ablation threshold fluence for the third harmonics is similar to threshold fluence at fundamental harmonics (0.2 J/cm^2). Therefore, the reduction of the wavelength does not have a major impact on the efficiency of the ablation. However, shorter wavelengths result in a smaller beam waist size when the same focusing lens is used. Beam waist for 1028 nm wavelength was measured to be 12.7 μm, while at 343 nm it decreased to ~7.6 μm (Fig. 2.13). Steel absorption also increases at shorter wavelengths.

Fig. 2.13 Comparison of the beam intensity profiles in the micromachining plane at 343 nm (7.6 μm at 1/e^2 level of maximum intensity) and 1028 nm (12.7 μm at 1/e^2 level of maximum intensity) wavelength.
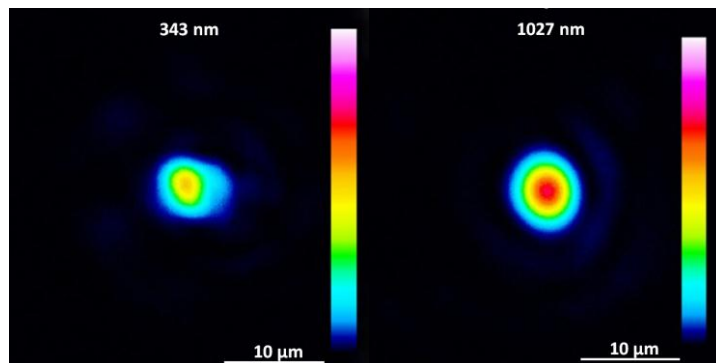
Therefore, in order to sustain the constant energy density, the line quantity in algorithm should be doubled, which results in increased processing time. Furthermore, the lower maximum pulse energy available at 343 nm wavelength, did not permit the same ablation efficiencies as at 1028 nm. Therefore, the groove depths are much smaller, as seen in Fig. 2.14.
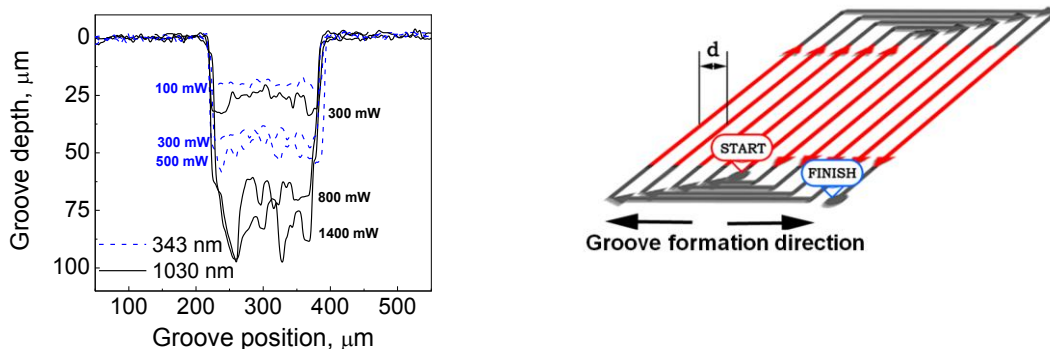

Fig. 2.14 Groove profile comparison when processed with 343 nm and 1028 nm wavelengths (left) and spiral from lines algorithm used (right). Red lines – laser ON, gray lines – laser OFF.

A single spiral algorithm was used (groove formation started from the centre outwards), and the algorithm was repeated 10 times without gas

injection. The total number of circles in the spiral was 17 at 1028 nm and 34 at 343 nm, and the distance between each circle (*d*) was 5 μm for 1028 nm and 2.5 μm at 343 nm. In these conditions, the constant energy density per area was sustained when average power at 343 nm was approximately one-third of the average power at 1028 nm. Sample movement speed was 100 mm/s; pulse repetition rate – 100 kHz, pulse polarization – *s*, focused directly on the sample surface with a lens of 25 mm focal distance.

The groove micromachining in no. 1.2379 steel samples at 343 nm wavelength showed no advantages in comparison with the 1028 nm wavelength. The ablation energy fluence thresholds were close at both wavelengths, and losses in conversion process decreased the average power at 343 nm wavelength by 4 times. So, greater ablation efficiency and greater micromachining speed for used steel could be obtained using the fundamental radiation of the laser.

2.7 The production of optimized grooves on stainless steel
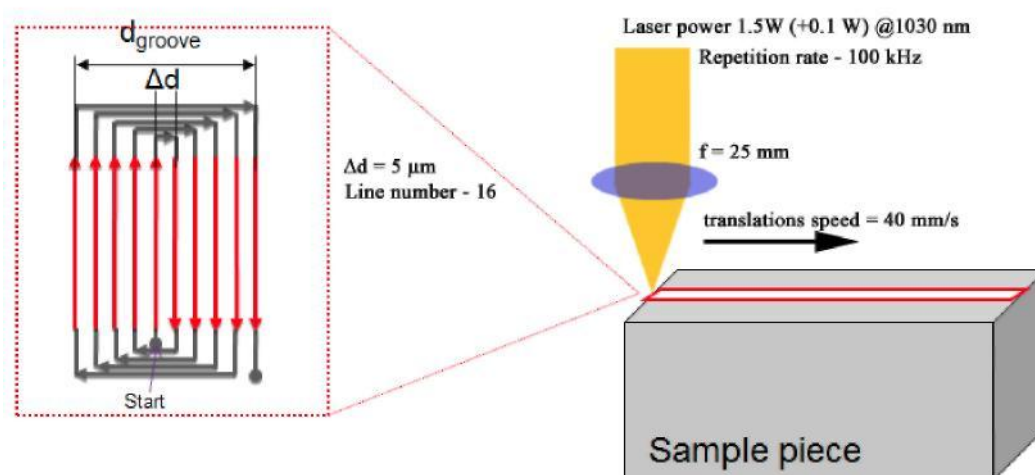

Fig. 2.15 The schematics of the groove writing algorithm.

For the setup with linear direct-drive servomotors stages stages, the spiral algorithm was selected as an optimal and was used for the required groove fabrication (Fig. 2.15). Laser pulses at 100 kHz repetition rate with 1.5 W of average optical power were used. Axis speed was 40 mm/s. The full spiral

structure, consisting of 16 lines separated by 5 μm, was completed in 20 s, and this covered the width of the 200 μm groove. For the sufficient groove depth, this patterning algorithm was repeated 15 times, resulting in an average 210 μm depth. To improve the roughness of the groove bottom, additional 10 repetitions with reduced laser power (0.1 W) were used in order to "polish" the groove bottom at the gentle ablation regime. 25 mm focal distance lens was used, and the beam was focused ~200 μm below the sample surface (with focusing above or close to the surface, "V" shaped grooves are formed by increasing the number of passes and the depth of the groove quickly saturates after approximately 20 passes). The beam intensity profile on the target plane was evaluated using the Dataray WincamD CCD camera by imaging focus plane with x10 telescope. It has a Gaussian shape (Fig. 2.13a) with beam diameter at the waist around 13 μm (at $1/e^2$ level of maximum intensity). During the laser processing, argon gas was injected into the groove for efficient debris removal.
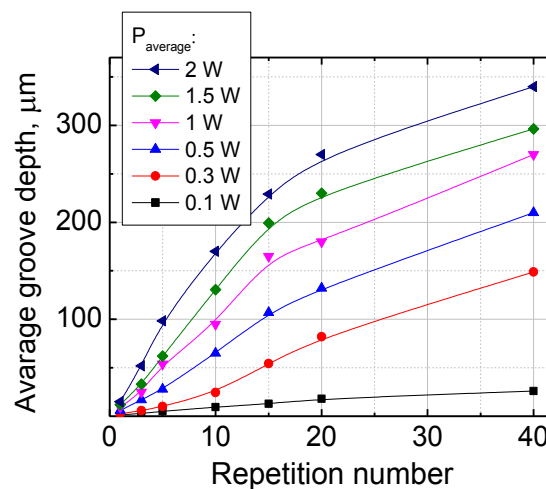
Fig. 2.16 The groove depth dependence on the scan passes.

Because of the limited energy of laser pulses, it was not possible to obtain a very deep groove during irradiation with a single shot or a single pass of the laser burst. Multiple passes of the sample under the focused laser spot can be used to produce significantly deeper grooves. For fewer than 60 passes, the depth increases linearly; however, after more passes, the groove depth does not increase with the number of passes and depth saturation is reached. The depth limit is to be expected since energy is lost via several mechanisms as the pulse

propagates down the groove. A limit is reached, where the fluence at the bottom of the groove is no longer sufficient to cause the ablation. Competition between ablation and material redeposition may also be significant. There exists a depth limit for drilling holes in metals with fs and ps-pulses. For a given sample thickness, there is a threshold fluence below which it was not possible to drill through the sample, even using a high number of pulses. The influence of repetitive scanning on the groove depth is shown in Fig. 2.16. It is evident in the graph, the saturation effect of the groove depth is not observed at least up to 300 μm with the pulse energies and focusing conditions tested, however, it was found that, in order to get smooth structures with steep slopes, groove depth and width ratio should be less than 2:1.
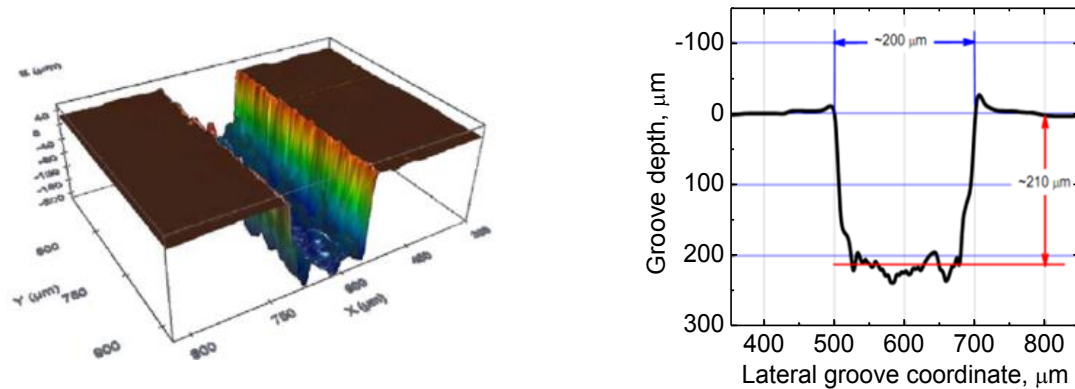
**Fig. 2.17 3D topographic image of the laser cut groove (left) and the averaged groove profile (right).**
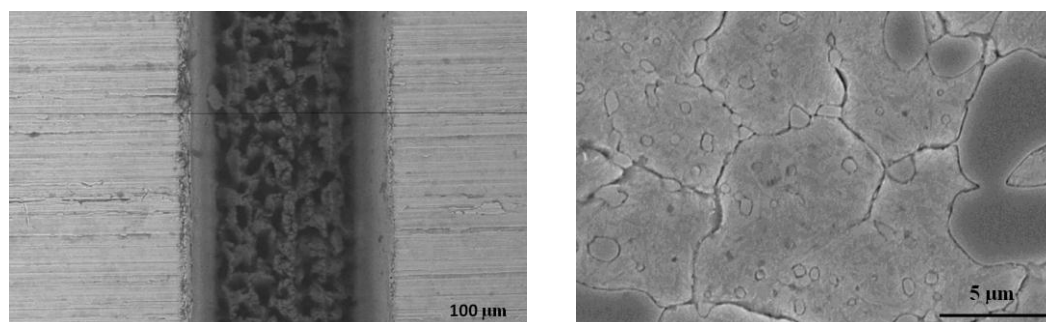
Fig. 2.18 SEM image of the micromachined groove (left) and micrograph revealing the grain size and distribution of phases of the steel plates (right).

The etched groove itself and the steel surface affected by laser were characterized using the different microscopy techniques including optical

microscopy, non-contact optical profilometry (Fig. 2.17), scanning electron microscopy (Fig. 2.18).

The algorithm resulting in grooves with the steepest walls and acceptable bottom irregularities consists of two alternating spirals (Fig. 2.19). The spiral motion paths follow each other. The first spiral is designed for cutting the groove from the centre outwards, while the other is reversed and cuts the groove from the outside inwards. This scheme was proved the most optimal in achieving the best roughness of the groove bottom and rectangularity and helped to prevent the asymmetric debris re-attachment to the groove walls without the need for gas injection. The other parameters influencing the final groove parameters are: the number of circles in the spiral (determines the width of the designed groove; circles should be separated from each other by a distance d), the repetition time of this combined algorithm (this parameter determines the depth of the groove), the scanning speed and the laser power (these parameters influence the ablation efficiency).
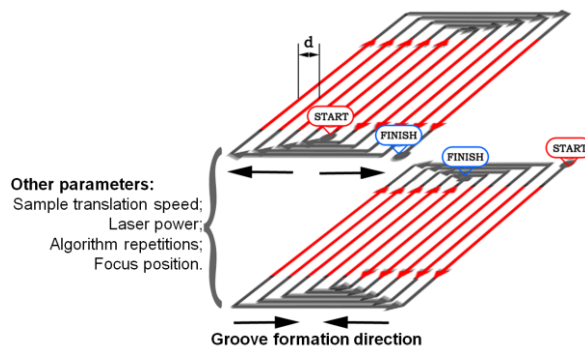
Fig. 2.19 Double-spiral algorithm with alternating origin between repetitions.

In addition, focusing should be kept at a certain depth below the sample surface. The polarization state of the beam has an important role, when the groove depth exceeds 100 μm, linear polarization perpendicular to the motion path is needed (p in respect to groove side wall) in the manufacturing process. Irradiation conditions and other experimental parameters used are listed in Table 2.4. All grooves were afterwards cleaned with distilled water in an ultrasonic bath.

Table 2.4 Micromachining on steel samples: irradiation conditions.

Laser repetition rate (f_r)	100 kHz
Wavelength (λ)	1028 nm
Pulse duration (t)	270 fs
Power (P)	2W
Scanning speed (v)	100 mm/s
Focusing lens (f)	25 mm
Focusing depth below the surface	200 μm
Circles in a spiral (for 180 μm groove)	17
Circles in a spiral (for 280 μm groove)	27
Distance between each circle (d)	5 μm
Total repetitions of the algorithm	14
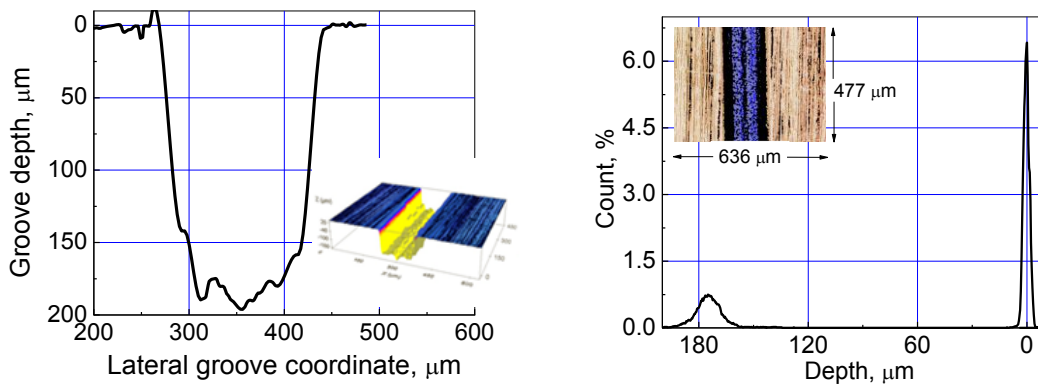
Fig. 2.20 Typical average profile and 3D topography of the 180 μm wide groove made in a steel sample (left); the height distribution of the area (636 x 477 μm²) with the groove (right). The average depth of the groove is 170 μm, bottom roughness RMS = 8.6 μm.
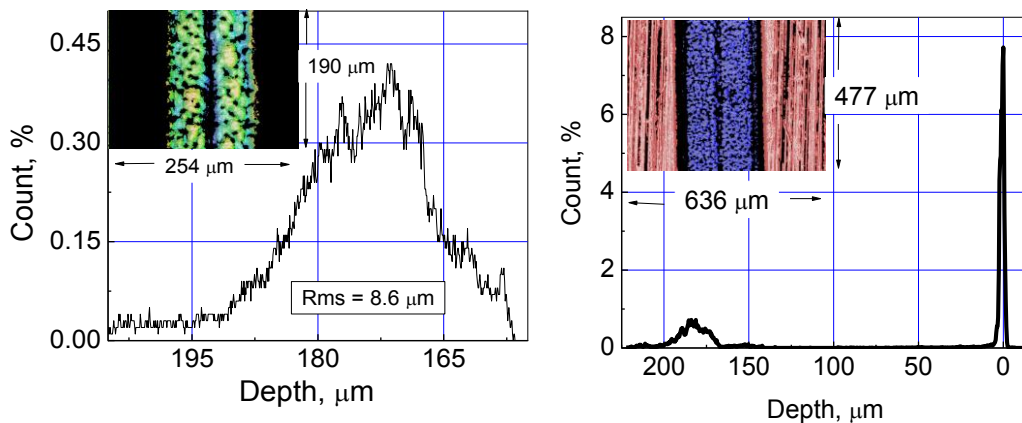
Fig. 2.21 The histogram of the depth level distribution at the groove bottom (left) and at whole groove (right). The standard deviation is 8.6 μm (RMS) (measured from this histogram). This accounts for 5 % depth accuracy.

Two kinds of grooves with different width were manufactured in the steel samples (the length of the groove was determined by sample length, either 50 or 10 mm). The resulting groove width was 180 μm (Fig. 2.20) and 280 μm (Fig. 2.21), while the depth of both grooves was close to 180 μm. No sharp spikes were observed on the groove bottom, and the overall groove bottom surface was sufficiently regular (the depth variations in the bottom were no more than 5 %). The profiles and histograms are shown in the figures below.

2.8 Micromachining on aluminium samples

One of the MesMesh project members, "Baltijos polisterenas" uses aluminium injection moulds in their production. This implied the requirement to produce wear sensors for aluminium as well. Grooves were ablated on aluminium samples. The identical bidirectinal spiral algorithm as described above and similar laser irradiation parameters were used on an aluminium sample without any optimization. The only parameter changed was the number of repetitions of the algorithm.
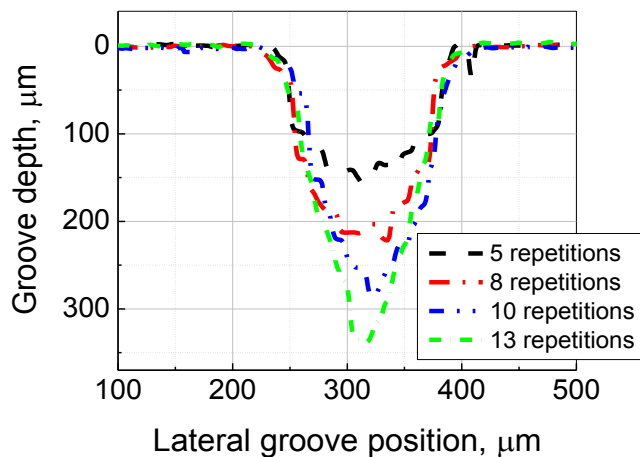
Fig. 2.22 Groove profiles made in aluminium with alternating the origin line-spiral algorithm repeating algorithm n times. Average power - 2 W, first harmonic, scanning speed - 100 mm/s, focused 200 μm below the surface with 25 mm focal distance lens.

It was revealed that ablation efficiency in aluminium was higher, and fewer repetitions were required to achieve 200 μm depths (Fig. 2.22). However, the quality of the groove bottom structure was considerably worse than that achieved in steel samples in the sense that the groove profile had a prominent "V" shape; though no spikes or asymmetric debris distribution was

observed. The reason for such groove formation could be the higher ablation threshold existing in the aluminium material (1.2 J/cm^2 for femtosecond pulses [163]). Thus laser fluence becomes too low for material ablation from the groove walls. Secondly, reflection, specific heat capacity, and penetration depth constants are different as well. Typical groove profiles and depth histograms are shown in the figures Fig. 2.23 and Fig. 2.24. The conclusion can be drawn that micromachining in aluminium is possible; however, laser parameters need to be optimized separately for every material.
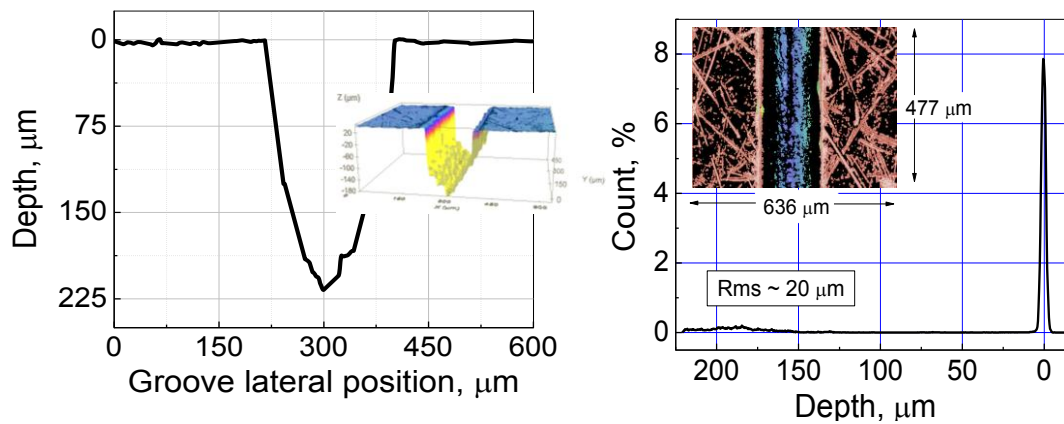
Fig. 2.23 Typical line and 3D profiles of the 180 μm wide groove made in the aluminium sample (left); Points height distribution of the area (636 X 477 μm^2) with the groove (180 μm) (right). The average depth of the groove is 190 μm, bottom roughness RMS = 20 μm.
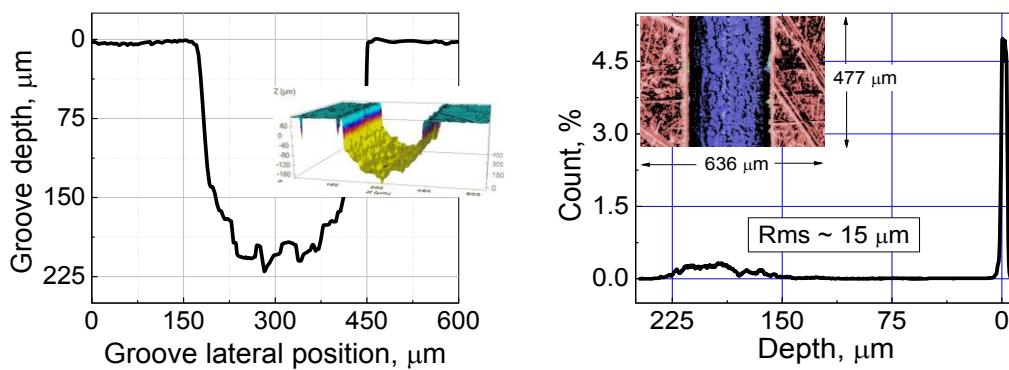
Fig. 2.24 Typical line and 3D profiles of the 280 μm wide groove made in the aluminium sample (left); Points height distribution of the area (636 X 477 μm^2) with the groove (280 μm) (right). The average depth of the groove is 200 μm, bottom roughness RMS = 15 μm.

2.9   Influence of noble gas injection

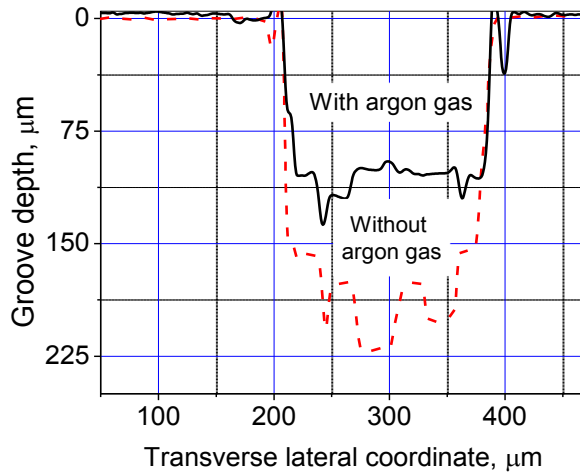Fig. 2.25 The averaged groove profiles made in steel with and without argon gas injection. Grooves manufactured at $\lambda = 1028$ nm, $P_{av} = 1.5$ W, $v = 40$ mm/s, $f = 100$ kHz, with the spiral from lines algorithm, repeated 10 times, focused 100 µm below the sample surface.

Fig. 2.26 The averaged groove profiles made in steel, with and without argon gas injection at a different number (shown in the graph) of the line spiral algorithm repetition times. Grooves were made at $\lambda = 343$ nm with $P_{av} = 500$ mW, $v = 40$ mm/s, $f = 100$ kHz.
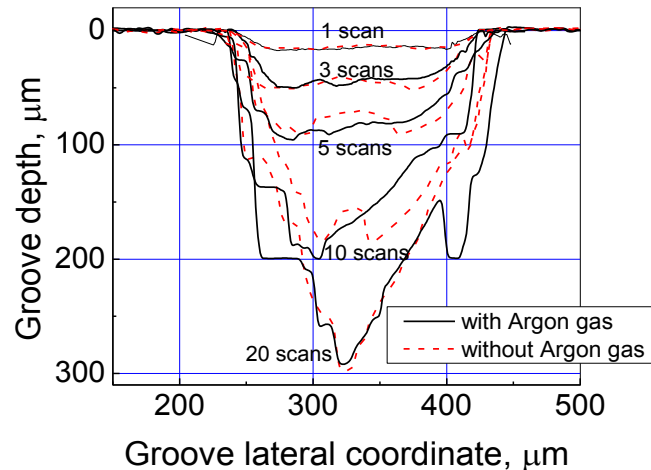
The influence of gas injection in the groove during the manufacturing procedure was also investigated. It was assumed that gas injection would also alter the groove manufacturing process, in particular by removing the debris from the channel and preventing hot particles from reattaching to the groove walls. However, the experiments carried out under gas injection (industrial grade argon gas, delivered by flexible rubber tubes and blowed on the laser spot area parallel to the direction of motion through the 500 µm needle under 3 bar pressure) demonstrated that, although groove quality increases, ablation is only half as efficient. The hot microparticles help to absorb the radiation more efficiently and redistribute it to the groove walls, improving ablation efficiency. However, this applies only to 1028 nm radiation (Fig. 2.25); no

considerable difference was observed between the groove quality irrespective of the argon gas injection when processed with 343 nm (Fig. 2.26). This suggests that due to lower ablation efficiencies, much smaller quantities of debris are reattached to groove walls and gas injection does not have a major impact on groove quality.

2.10   The effect of laser polarization
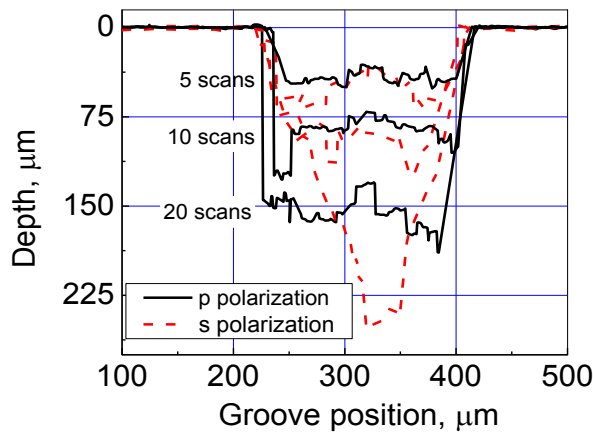
Fig. 2.27 The groove profiles made in the steel sample using different writing beam polarization. P_{av} = 1.5 W, λ = 1028 nm, f = 100 kHz, v = 100 mm/s.

When the groove depth increases, light reflectivity from the groove walls becomes crucial. If the reflectivity is high, the walls reflect most of the incident light to the central part of the groove. In this situation, it becomes hard to control even energy distribution in the groove: the walls redistribute the energy to a different groove area, and the groove loses its smoothness and tends to have a V-shaped profile. So it is essential to minimize the reflectivity from the groove wall. This can be achieved with the *p*-type polarization. Fig. 2.27 shows the dependence of the groove profiles on the processing light polarization. It is obvious that for the *p*-type polarization the groove profile is more rectangular, and the bottom is flatter.

86

2.11 Significant results and conclusions

1. The ablation threshold of the mould steel at 343 nm is 35 % smaller in comparison with the ablation threshold at 1028 nm, however, the higher pulse energy of the pulses at 1028 nm is more profitable for micromachining grooves compared with 343 nm pulses.

2. With a low NA focusing objective, grooves tend to have a prominent V-shape structure. Only the "gentle" ablation regime could be reached in this condition.

3. The "strong" ablation regime can only be reached using a tight focusing condition. Employing the sample positioning with linear direct-drive servomotors stages, the grooves can be ablated, but they are much smaller (~10 μm in width) and deeper (reaching up to 8 μm after the single scan) compared with the focusing using low NA lens. By employing a sample translation algorithm, wide grooves can be fabricated.

4. The best quality structures were achieved when focusing below the sample surface (~200 μm for 25 mm focal length focusing objective when grooves of 50-200 μm width are machined).

5. The structures manufactured with the bidirectional spiral algorithm (among other algorithms such as raster scan, single line scan with long focal distance lens, circle-spiral scan, conventional hatch and others) exhibit the steepest walls and minimal bottom waviness. The formed grooves are symmetric and regular. However, the fabrication procedure is rather slow: the time needed to produce a single groove with a length of 50 mm is about 15 minutes.

6. Linear polarization of light parallel to the direction of motion is more suitable for the production of rectangular grooves: the process is better controlled in this way. Otherwise at least the single line grooves appear in "V" shaped form.

3. Groove fabrication using micromachining system based on high repetition rate femtosecond laser and galvoscanner

Material related to this part of the dissertation was published in European Patent [P1], articles [A1-A2] and proceedings [C1-C2].

As described in the previous chapter, experimental data confirmed the acceptance of the previously described hardware (the "moving part" approach based on linear Aerotech table positioning system). The system provides a sufficient degree of freedom in order to perform micromachining tasks with good enough precision, and namely production of 200x200 μm sized rectangular grooves in stainless steel. However, this approach results in rather slow fabrication: the time needed to produce a single groove with a length of 50 mm is about 15 minutes. This is mostly limited by the inertia of linear stages and the sample. To increase the speed of the micromachining process and reduce the cost of expensive equipment, another approach to the "moving laser beam" was investigated and found to be more appropriate for micromachining microgrooves whose dimensions are not higher than the working field of available F-theta lenses when they provide beam focusing to sizes at least 5x smaller than the required groove width.

3.1 Galvoscanner system for realization of the "moving beam" concept

In the case of the galvoscanner, the moving part is not a heavy piece of metal as in the case of linear direct-drive servomotors stages but the reflecting optical element such as a dielectric or noble-metal film mirror. A 1'' optical mirror is far less heavy and has a much lower acceleration/deceleration time. An alternative experimental setup was developed to test this concept (Fig. 3.1). The beam transportation system is combined with a fast-moving galvoscanner system and is integrated with the same laser system. The new optical setup consists of galvoscanner head, beam transportation, special

focusing, scanner controller interface card, SCA software, power supply optics and a computer.
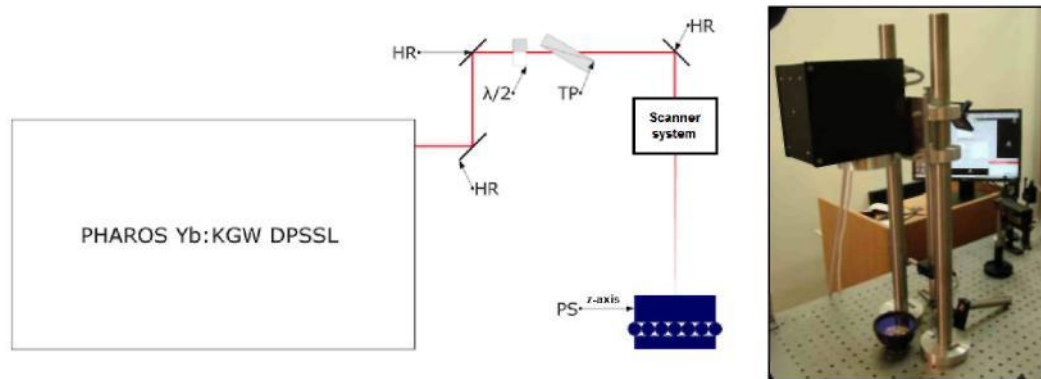
Fig. 3.1 Micromachining system based on femtosecond Pharos laser and galvoscanner: optical scheme (left) and view of galvoscanner module (right).

The galvoscanner from ScanLab [164] ("IntelliSCAN 10" [165]) has been adopted for this purpose. By using dedicated PCIe computer card (RTC4 [166]) and appropriate electronic circuits, the motion path of the scanner mirrors and fs-pulses from the "Pharos" laser were precisely synchronized. The advantage of the above-mentioned galvoscanner head is its capability of reaching a "marking" speed of up to 3 m/s with a high positioning accuracy and a up to 14 m/s marking speed. This is approximately a ten-times higher speed than in the previously described system. Scanner repeatability is < 2 µrad. 100 mm focal length F-theta objective from Scanlab was used (111 mm working distance, 70x70 mm^2 scanning area, ±28° scanning angle, ≤12 mm input beam diameter). Further details on the parameters of galvoscanner can be found [165]. The idea of the concept oriented towards optimizing the processing time was the use of galvoscanner together with the F-theta optics. On the other hand, F-theta optics offer only a limited scan field (less than 50x50 mm with 100 mm focal distance F-theta lens), which is much smaller than that achieved by the approach with the "moving sample". In order to have a sufficiently large scanning area, a long-distance-focusing F-theta lens is necessary. This is not the critical point because a system that utilizes both concepts can be constructed. However, in such a case additional expensive

hardware is required. Due to the larger focal distance and lower lens NA, an additional limitation arises: the minimal beam diameter is approximately 3 – 5 times bigger than in the previous system. This requires reoptimization of scanning algorithms with respect to groove morphology.

3.2 Optimal conditions for groove fabrication
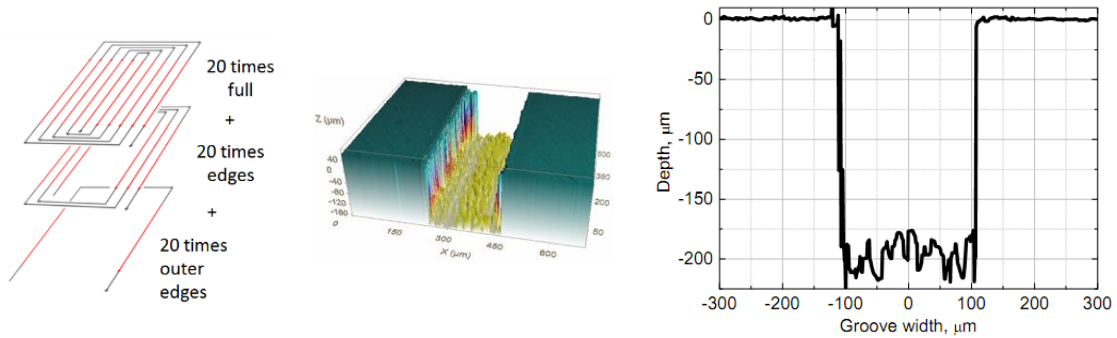
Fig. 3.2 Sketch of composite line spiral scanning algorithm (left), typical 3D surface morphology topography (centre) and averaged profile (right) of the grooves micromachined in the steel samples with the galvoscanner using the improved line spiral algorithm with additional outer line scans.
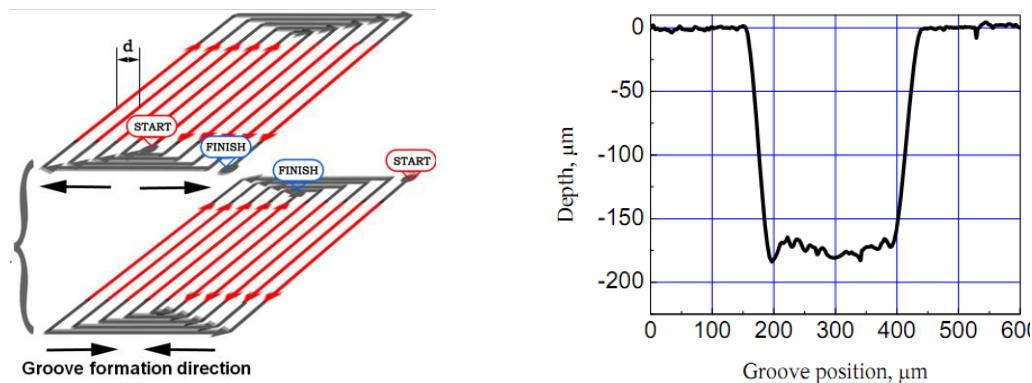
Fig. 3.3 Sketch of bidirectional spiral scanning algorithm (left) and averaged profile (right) of the grooves micromachined in the steel samples with the linear direct-drive servomotors stages using the alternating origin line spiral algorithm.

Laser beam after the scanner was focused by an F-theta lens to the spot with a diameter of ~30 μm at $1/e^2$ level. The estimation of the spot size was performed with the Ophir SP620U CCD camera (5.4x5.4 μm pixel size) [167]. The experiments were performed with the average power of the Pharos laser at 4.5 W and the pulse repetition rate at 50 kHz. This corresponds to the pulse energy 90 μJ and laser fluence 14.3 J/cm². About 10 conventional scanning

patterns were examined for the groove fabrication. They included the raster scan, circle spiral algorithms, the "wobbling" scanning algorithm, line spiral algorithms, the "rotating mirror" scanning algorithm, alternating spiral algorithms and various hatch algorithms. The best results achieved are presented in Fig. 3.2, and Fig. 3.3 corresponds to the composite spiral of lines algorithm (with extra scans at outer spiral boundaries) and bidirectional spiral algorithms with the alternating origin of the spiral. More rectangular grooves were machined using the composite spiral algorithm (<4° wall inclination angle, ~12 μm RMS roughness) but the smoother bottom was achieved using the bidirectional spiral algorithm (9.6° wall inclination angle, 8 μm RMS roughness). During the microfabrication process, the beam was scanned with the galvoscanner at 1 m/s speed. The full spiral structure, consisting of 19x2 lines separated by 5 μm, covered the groove width of 190 μm. For sufficient groove depth, this patterning algorithm was repeated 120 times, which resulted in an average 200 μm depth. For the composite spiral algorithm, the outer edges were ablated additionally repeating first 3 lines pattern 20 times and then 1 line pattern another 20 times. The waist of the focused beam was 200 μm below the sample surface.

Table 3.1 The main parameters of the two developed laser micromachining systems for groove formation in steel.

Parameter	System based on linear positioning stages	System based on galvoscanner
The parameters of used scanning algorithms		
Speed of the sample or scanned beam	100 mm/s	1000 mm/s
Focusing lens	25 mm	100 mm
Focus plane position	-200 μm	-200 μm
Number of circles in a spiral	27	19
Distance between each circle (Δd)	5 μm	5 μm
Total repetitions of algorithm	14	120
Laser irradiation conditions		
Average power	2 W	5 W
Repetition rate	100 kHz	50 kHz
Pulse energy	20 μJ	100 μJ
Focused beam diameter (1/e)	~12.7 μm	~30 μm
Micromachining time		
Time required for preparation of single 0.2x0.2x10 mm grove	15 min	1 min

The optimized laser, positioning and focusing system parameters used in the earlier described and this micromachining systems for machining grooves with dimensions 200 μm x 200 μm x 50 mm in steel blocks (Fig. 3.4) are presented in Table 3.2.
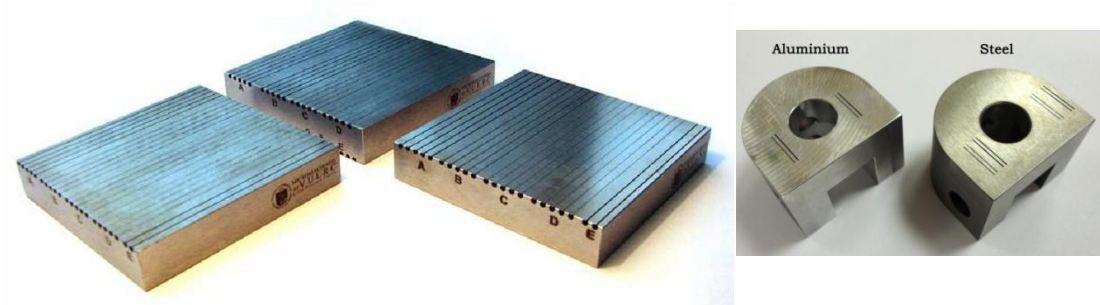
Fig. 3.4 Steel blocks (50 x 50 x 10 mm³), samples with several target dimension grooves machined.

3.3 Characterization of groove parameters

All grooves were cleaned in the ultrasonic bath by using heated distilled water with added cleaning agents for at least half an hour prior to the optical characterization of the groove morphology. This step was necessary to remove the porous recast material attached to the surface in the form of nano/micro particles that remain after the processing. Furthermore, all grooves were characterized by using the optical microscope Olympus BX51 [168] and optical profilometer Sensofar PLj2300 [169]. Fig. 3.2 and Fig. 3.3 depict the profiles and 3D images of grooves with optimized experimental parameters made in actually manufactured steel samples, which were sent in "Set 1" and "Set 2" batches (~5 samples per batch) to project partners for further wear sensor prototype manufacturing steps. Detailed experimental conditions are listed in Table 3.2. The typical untreated surface roughness (RMS) of all samples was estimated to be approximately R_{rms} = 0.5 μm, whereas characteristic RMS values characterizing bottom roughness were in the range of 8 to 12 μm (both measured from the area of 0.02 mm²). Machined bottom surface quality was visually inspected by SEM microscopy. Inspections were performed with a "Hitachi" TM-1000 (Tokyo, Japan) microscope with 15 kV

accelerating voltage and 20~10000X magnification without any conductive overlayer. Roughness measurements were taken either directly from the groove bottom topography or by inspecting the top surface of a polymer replica of the groove. Table 3.2 presents the comparison of the groove roughness with comparable groove dimensions machined with different approaches. The system based on linear stages seems to give slightly better results in terms of surface roughness (Table 3.2). Also, the microgroove production time can be significantly reduced (by more than ten times) when using fast moving galvoscanner mirrors, however, the roughness of the groove bottom is greater by a factor of ~1.3, mainly due to focusing using lower NA lens.

Table 3.2 Comparison of typical groove parameters prepared by different methods.

Parameter	System based on linear servomotor stages	System based on galvoscanner
Average depth of the groove, μm	180	197
Groove width at surface/bottom, μm	280/200	218/215
Bottom roughness (RMS), μm	8.6	11

3.4   Influence of the beam transversal distribution

It is known that the groove parameters are dependent on the laser beam profile quality and its shape. By changing focusing conditions, the groove quality can be varied [170]. Therefore, for specific laser processing tasks, the optimal focusing conditions should be accurately chosen. Gaussian beam profile might not be the most optimal for groove micromachining task as the intensity distribution in this profile is not homogeneous: the central part of the beam is much more intense than the periphery (left part of Fig. 3.5). This could influence overall quality parameters of the fabricated groove, such as groove wall inclination, bottom surface roughness, and the HAZ area. On the other hand, the HT beam profile ideally has uniform energy distribution that can yield more efficient laser energy use for ablation and thus allow more precise control of critical groove parameters.

To transform laser beam transversal distribution, the beam shapers are used, which either affect the spatial phase front of the beam and work like a Fresnel lens (diffractive beam shapers), or redistribute laser spatial energy in a refractive way to transform the Gaussian profile to HT. The advantages and drawbacks of such a transformation, as well as the use of the transformed beam for precise groove fabrication, is hardly predictable in advance as the real intensity distribution heavily depends on the input beam parameters, such as beam quality as well as aberrations in the focusing optics. Therefore, experimental results on groove microfabrication with an HT shaped laser beam are reported below.
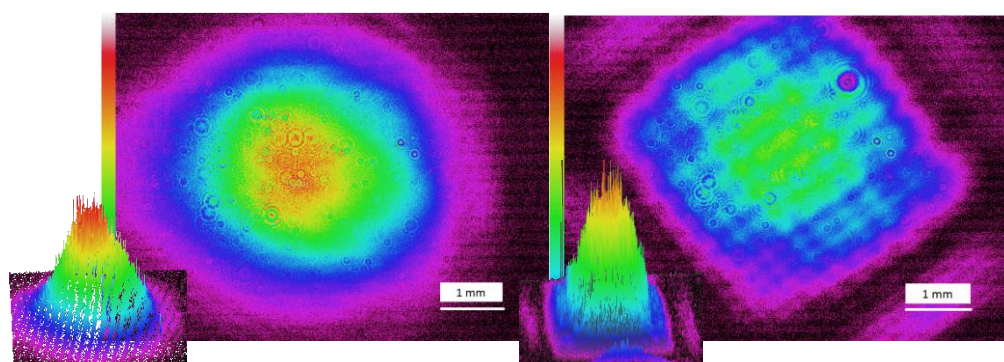
Fig. 3.5 The input Gaussian beam profile (left) before the diffractive beam shaper and transformed profile in the far field after beam shaper without the focusing objective (right).

Gaussian-to-HT beam conversion was realized using a diffractive shaper converter manufactured by TOPAG Lasertechnik GmbH [171]. The converter consists of the special DOE hologram, recorded in fused silica by means of lithographic methods and etching. This is a kind of spatially nonhomogeneous phase plate with a continuous and smooth phase relief profile, which is designed to convert spatially Gaussian distribution beam into a flat profile beam after the Fourier transformation by the objective lens in the vicinity of the focal plane. DOE is inserted into the beam pass and because of the spatial distribution of material thickness or density (which affects the refractive index) affects the angular spectrum of the beam wave vectors effectively adding new

94

spatial frequencies. These spatial frequencies Fourier transformed by the lens result in a designated intensity distribution. Table 3.3 presents the specifications used DOE. The images of the beam intensity distribution without the beam shaper and in the far field of the shaper (without the focusing lens) are shown in Fig. 3.5. It is obvious that the beam shaper transforms the profile from circular into rectangular.
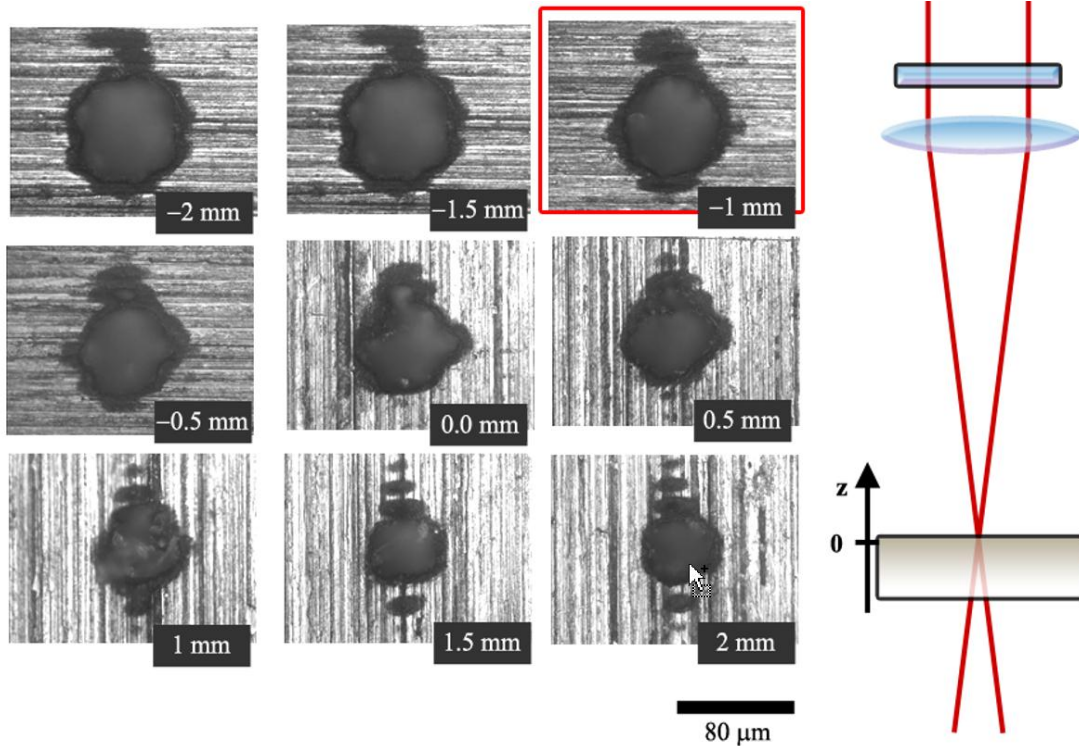
Fig. 3.6 Ablated surface (steel) morphology dependence on focus position, using HT beam profile. Surfaces were treated with 1000 pulses with the 50 µJ energy.

Table 3.3 Specifications of FBS Top Hat beam shaper.

Material:	fused silica	
Input beam:	TEM_{00}, 4 mm ø at $1/e^2$ intensity level	tolerance +/- 5 %
Necessary free aperture:	2.2x (or better 2.5x) beam diameter@$1/e^2$	along total beam path
Minimal lateral size of Top Hat spot:	1.5x diffraction limited Gaussian spot	square form
Homogeneity:	± 2.5 %	rel. to average intensity within Top Hat
Wavelength:	1064 nm	
Transmission:	> 99 %	AR/AR coating
Efficiency:	> 95 %	of input energy within Top Hat profile
Damage threshold:	4 J/cm^2 for 10 ns pulses	
Recommendation: accessories:	x/y-adjustment mount; adjustable beam expander	

Such diffractive beam shapers have to be used together with some focusing objective, and the highest beam homogeneity (2.5 % uniformity from the average value at the top of HT beam) could only be achieved in the proximity of the objective focus. In order to investigate, how full beam transformation takes places and what is the best shaper/sample position, the shaper was installed in the beam line in front of the galvoscanner, and the laser beam was focused with the 100 mm F-theta lens on a steel surface.
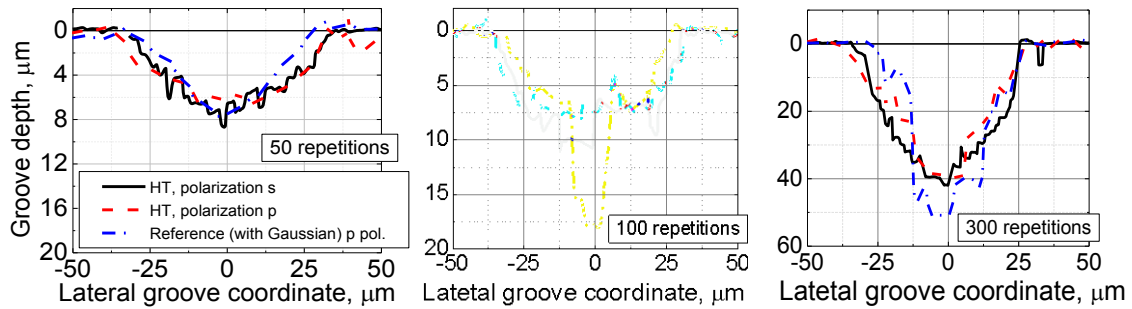
Fig. 3.7 The comparison between groove profiles ablated with the HT and Gaussian laser beams at different polarization states and beam pass repetitions of single line cutting. (P_{av} = 5 W, f = 50 kHz, v = 1000 mm/s).

Laser pulses had energy values reaching 50 µJ, and this was enough to initiate the laser ablation process even when the sample was positioned not exactly in the focus. Moving the sample along the beam propagation direction with respect to focus, it is possible to determine the HT beam formation position from the morphologies of laser-ablated craters. These results are shown in Fig. 3.6. As can be seen from the picture, when the sample is in position "-1 mm" (the axis origin was chosen close to focus), the resulting ablated crater is shaped like a slightly deformed circle. Gaussian beam focus (without FBS shaper) appears to be at the same position. When the sample is moved towards the lens (focus position is inside the sample), the ablated crater becomes more circular, and additional ablated lines could be seen on both sides of the crater. These lines become more prominent when the focus is moved deeper under the sample surface. The lines are artefacts of the diffracted beam (higher order diffractions) arising from the beam shaper. It is clear that it is not

96

possible to achieve a rectangular beam profile by moving the focus inside the sample. If the sample is moved in the other direction – outwards from the lens (focus position is above the sample surface), the crater develops a rectangular morphology. From these results, it is clear that the most prominent HT rectangular profile forms at the geometrical focus and behind it. This is opposite to the optimal microfabrication procedure with the Gaussian beam profile, where the laser focus had to be kept *below* the sample surface. Theoretically, the steepness of the edges of the HT beam, which affects the achievable minimum width, is diffraction-limited. However, practically limitations arose because of the input beam quality ($M^2 = 1.3$) and aberrations in the F-theta objective. The size of the HT profile can be adjusted by the focal lens distance and follows an NA of the focusing objective according to the equation:

$$2\omega_{TH} = \frac{4k\lambda}{\pi} \frac{f}{D} \approx \frac{\lambda}{NA}, \tag{3.1}$$

where $k \sim 1.5$ is the empirical shaping parameter, D is the diameter of the input beam on a lens, f is the focal lens of the objective. Practically, the transformed beam will be at least 1.5 times bigger than the Gaussian waist produced by the input beam through the same objective.

The single line groove width ablated with the HT profile was ~80 µm (with a sample translation speed of 50 mm/s), while the Gaussian beam ablated a line, which width reaches only 55 µm. The depth of the grooves made with the HT beam was ~5 µm, and its walls were steeper than those of the groove made with the Gaussian beam (depth ~8 µm). This difference could affect the quality and the steepness of the walls of the microfabricated target grooves. Further investigation are therefore required.

In Fig. 3.7, the results of groove formation by scanning a single line across the sample surface with different beam profiles are shown. The depth of such grooves is increased by repeating the scanning procedure multiple times. These results are similar to those acquired in the hole drilling experiment when the repetition number is not high (<100), the Gaussian beam profile produces
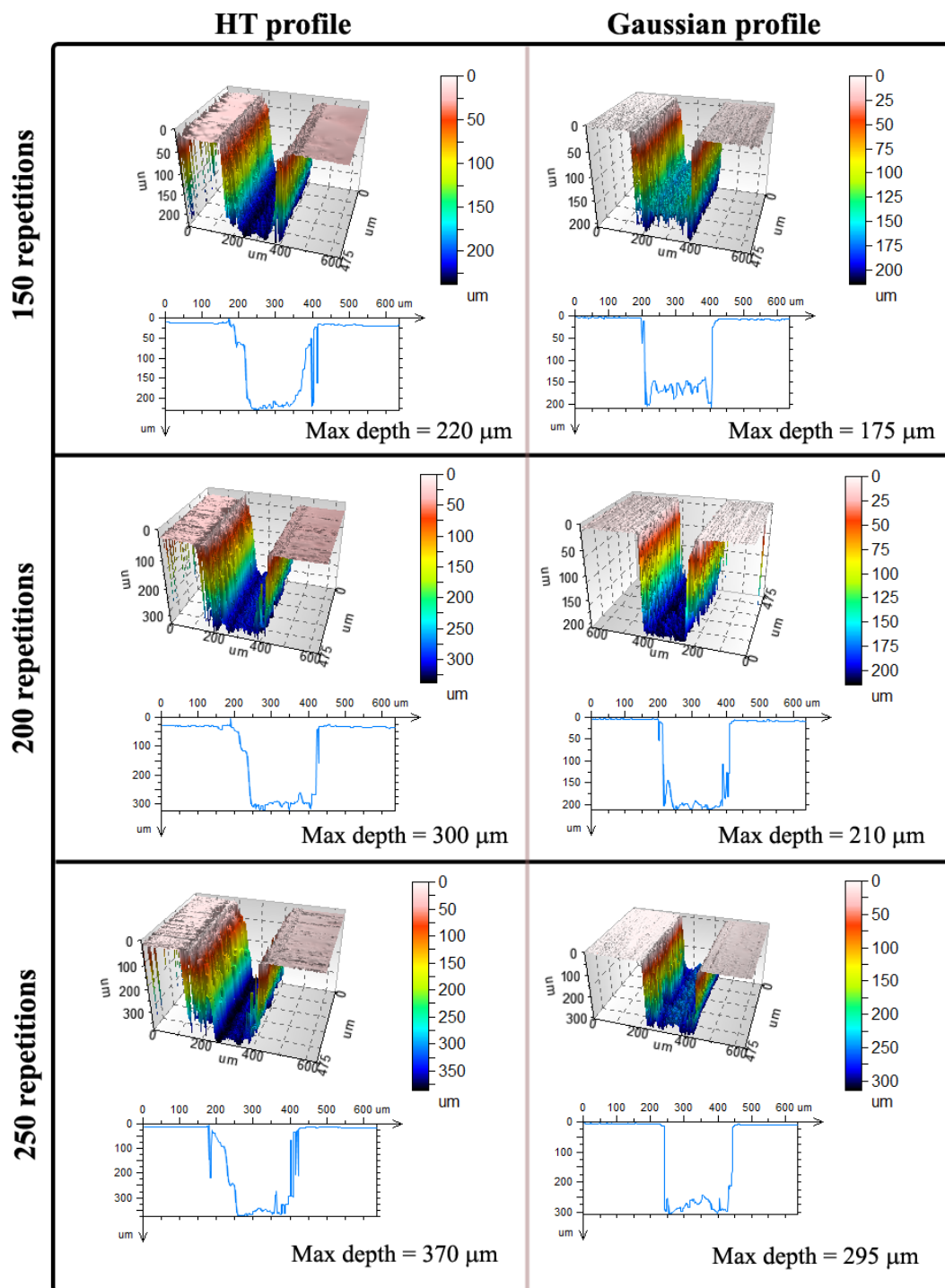
Fig. 3.8 The comparison of the grooves ablated with the spiral algorithm (10 spirals with 5 μm step) using the HT and Gaussian beam profiles with different algorithm repetition numbers. Scanning parameters: 5 W, 50 kHz, 100 mm F-theta lens, 1000 mm/s.

deeper grooves but with an increasing number of repetitions, grooves made with the HT and Gaussian beams become comparable. It should be noted that

98

p-polarization was used in the case of the Gaussian beam. Also at initial cutting (the groove depth <30 μm) stages, grooves made with the HT beam have a more rectangular profile than Gaussian. This was expected, as the HT beam has been successfully utilized for thin film scribing minimizing detrimental layer melting[172]. However, at later stages of groove cutting both profiles became comparable.

In order to reach sufficient groove width and depth, the writing algorithm and multi-pass laser treatment were employed. Results are shown in Fig. 3.8. In this figure, 200 μm width grooves manufactured in a steel sample using an identical line spiral algorithms are compared. It is clear that the HT beam profile deteriorates the groove walls and the steel surface near the groove. Both beams produced no visible kerf at groove sides, however in the case of the HT beam the steel surface at groove sides is destroyed. The HT beam produces deeper grooves compared to the Gaussian beam, but overall groove quality is worse. Grooves made with the Gaussian beam have a flatter bottom and steeper, symmetrical walls. Material ablation in the deep groove (>50 μm) is more accurately controlled by the Gaussian than by a transformed with DOE beam. However, the Gaussian beam limits maximum achievable groove depth to a lower value.

3.5   Groove roughness characterization with a polymeric replica

This subchapter presents measurement results of the bottom surface quality of a typical groove, fabricated in steel samples. In Fig. 3.9, steel samples are shown, which were examined using this technique. Each has two fabricated grooves with different depths for the actual and reference measuring circuitry of the wear sensor. The deeper groove was dedicated for the reference circuit, and the shallower – for the measuring circuit. The optimal (bidirectional spiral or composite spiral) writing algorithm was used for groove ablation (main micromachining parameters are shown in Table 3.4, while the algorithm was described in detail in previous subchapters.

Fig. 3.9 Samples prepared for ceramic mesh fabrication. Two separate, parallel grooves were fabricated on the surface of the steel sample, with dimensions 350x300 µm and 310x500 µm².
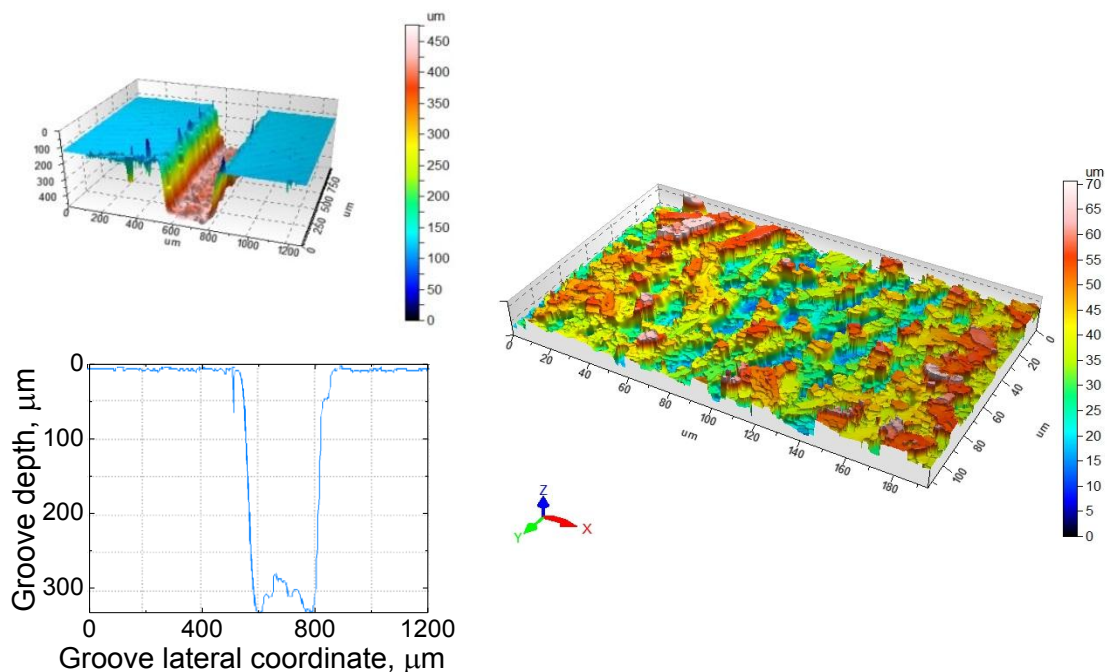
Fig. 3.10 Topographic image of grooves, having 300 µm depth, a bottom surface (left). The full groove topographical image and groove profile are shown at the right. Resulting surface roughness is 12 µm (std. dev.).

In previous experiments, the profiles of the laser-machined grooves were investigated with an optical profilometer 2300 µPLU (from Sensofar). However, measuring precise groove topography with an optical profilometry from which the average groove profile, wall inclination angle as well as bottom surface morphology is extracted afterwards, remains a challenging task. Fs-laser structuring makes the surface of metals highly absorptive [173-176]. As the structures get deeper (in the case of grooves), it gets even more absorptive,

as the light gets trapped between groove walls. Optical profilometry requires high sample reflectivity as it relies on the light reflection from a measured point. Especially, when the groove aspect ratio is higher than 0.25 - 0.5, light from the profilometer is strongly affected by the steep walls. No matter how bright the illumination is - only a small fraction of light is reflected from the bottom surface to reach the photodetector.

Table 3.4 Typical parameters of the grooves for the mesh fabrication.

	350x300 μm^2 groove	310x500 μm^2 groove
Scanning speed	1000 mm/s	1000 mm/s
Focusing conditions	F-theta lens	F-theta lens
Focal distance	100 mm	100 mm
Waist position with respect to the surface	~150 μm under the surface	~150 μm under the surface
Circles number (line spiral algorithm)	29	25
Beam polarization in respect to the groove wall	p	p
Distance between each circle (Δd)	5 μm	5 μm
Total repetitions of algorithm	145	220
Average micromachining time (one groove with 50 mm length)	120 s	250 s

Such a situation usually leads measured areas with zero light intensity in the topography data, which are being "filled" by the profilometer software according to valid adjoining measured data to adequately present the data. This is usual procedure; however, when these "dark" areas get too big, the whole measurement is no more valid. Particularly sure this problem manifest itself in the measurement errors near the steep groove walls.

In order to verify that the micromachined grooves have the same shape as measured, or in latter cases – to enhance the measuring quality, additional tests were performed. A polymeric replica moulding technique was applied. An inverted polymeric replica of the groove was produced. This process consists of creating a liquid PDMS (polydimethylsiloxane) mixture having a thermal initiator (a substance that initiates polymer hardening when exposed to the heat) at ratio 10:1. It is then poured onto the original sample and heated at

100 degrees C for 60 min (see Fig. 3.11). The high wettability of the mixture, heat and low vacuum help to debubble the PDMS-metal interface and ensure that all the voids are filled. Finally, under heat, the viscous PDMS thermal-initiator mixture withers and becomes a rubber-like mould (stamp replica). The shrinking of the mixture was found to be negligible.

The PDMS stamp is then peeled off having a negative imprinted structure. Later, the stamp replica was covered with a thin gold layer (~20 nm), in order to increase sample reflectivity. Such an inverted replica can be more successfully investigated by confocal optical microscopy as well as by SEM. As the groove bottom becomes the top layer of the sample, roughness estimation is greatly simplified.
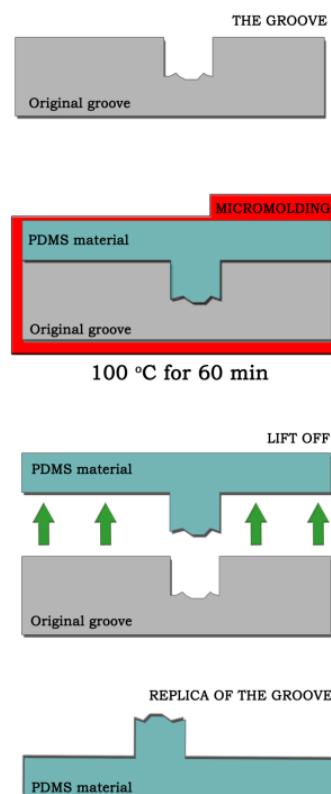
Fig. 3.11 Steps of the micromouldig technique on the PDMS material to measure groove bottom.
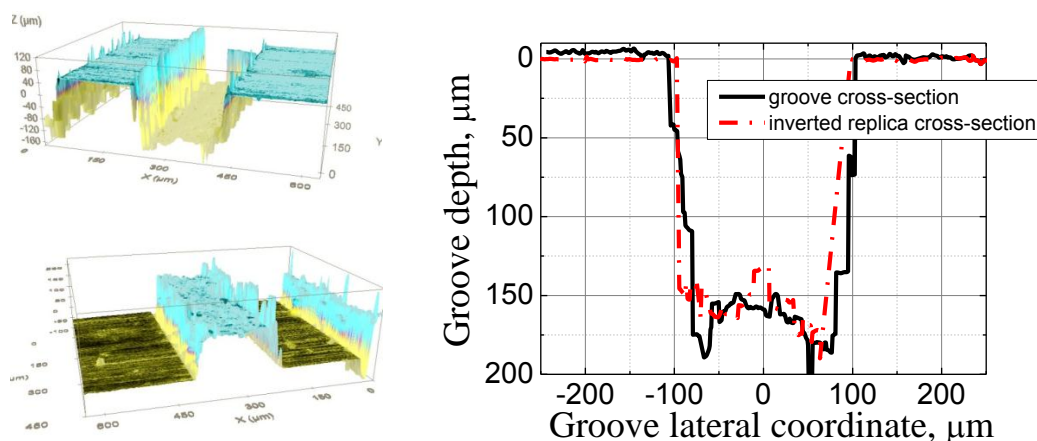
Fig. 3.12 Topographic images of micromachined groove and its replica in PDMS polymer and their cross-sections.

Two measurements of the same groove were made by taking a profile of the original groove and its inverted replica Fig. 3.12. The results were similar

with minor mismatches, which arises the different groove profile. It was difficult to find exact the same spot on the sample to measure identical groove profile. Nevertheless, data confirms the validity of profilometer data when it actually measures the deep trenches.
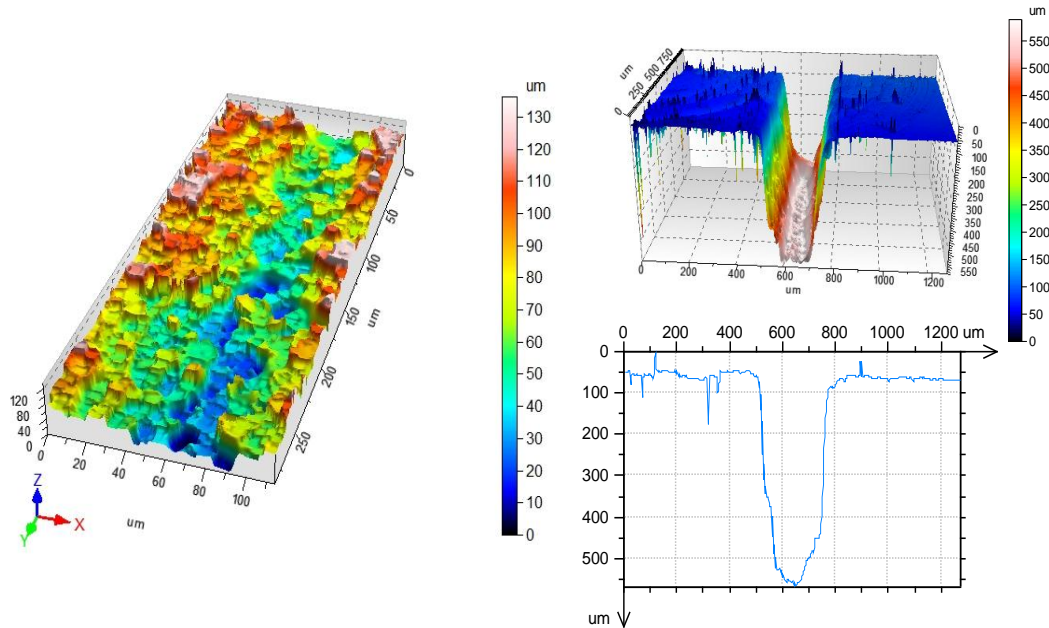
Fig. 3.13 Topographic image of the grooves, having 500 µm depth, a bottom surface (left). The full groove topographical image and groove profile are shown at the right. Resulting bottom surface roughness is 25 µm (std. dev.).

Fig. 3.13 and Fig. 3.10 show the topographies of the groove bottom surfaces made with this technique. Using statistical analysis, it was evaluated that the bottom surface of the 300 µm depth groove has a roughness of 12 µm (std. dev.) (measured on the area of 0.02 mm^2), while the roughness of the 500 µm deep groove was 25 µm (std. dev.) (measured on the area of 0.02 mm^2). The deeper the groove, the rougher is the bottom of the groove. This is a predictable result, as controllable laser energy deposition onto the material becomes complicated due to many effects including light reflection from the steep walls, different light absorption of structured bottom surface, etc. However, even 25 µm roughness accounts for only a 5 % error in the whole groove depth. By measuring the width of the bottom surface and

comparing it to the groove entrance width, it is possible to evaluate the inclination angle of the groove walls. This angle is estimated to be in the range of 75 - 85° for 200 – 300 µm depth grooves (90° means vertical groove walls).

3.6 Fabrication of deepest grooves in stainless steel

Deeper grooves can be fabricated if the writing algorithm is continuously repeated multiple times. However, there is a limit to the depth that can be reached using a constant laser power and unchanging focusing conditions. Several loss mechanisms contribute to the reduction of the material removal rate – the most prominent being the decreasing of laser fluence that targets the surface under investigation, when fluence drops below the ablation threshold, material removal halts and no deeper grooves can be fabricated. The knowledge of such a maximum groove depth and thus the limit of the laser micromachining stage can be beneficial in many ways, so here the results on the microfabrication of the deepest grooves are presented.
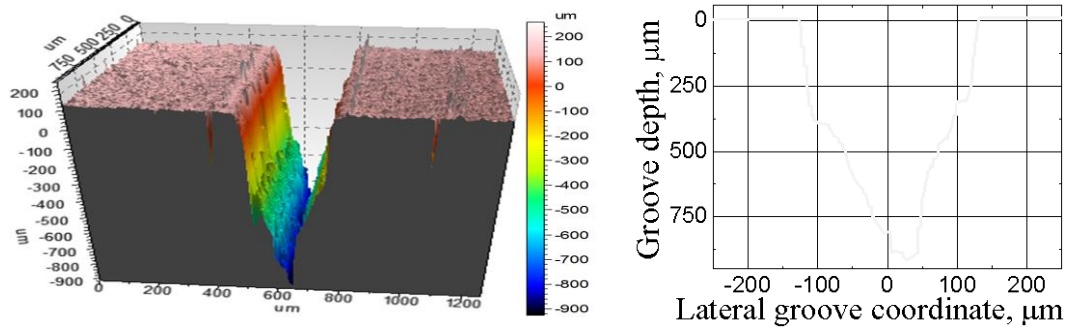
Fig. 3.14 The deepest groove ablated in a steel sample. 3D topographic profile is shown at the left, and non-averaged cross-cut profile depicted at the right.

The deepest groove, microfabricated with a 5 W, 1028 nm, 270 fs-laser system, with pulse repetition rate at 50 kHz, and using the spiral writing algorithm, had a depth reaching 900 µm. The groove width at the top was 280 µm. The topography of the groove and the profile are shown in Fig. 3.14. The writing algorithm was repeated 500 times, the beam was scanned at 1000 mm/s by the galvoscanner and micromachining of a 5 mm length groove

104

took approximately 7 min. As can be seen from the groove profile, after the groove reached the depth of ~300 μm, a prominent V-shape start to form. It was demonstrated earlier that the typical steepness of the wall reaches 75-80°. Thus the expected depth for a 280 μm width groove should be in the range of 600 – 800 μm. The results show that higher values (900 μm) could be reached. However, no flat surface at the bottom is reached. This would require additional experimental affords and more advanced scanning algorithm, which would involve sample lifting towards focus as the groove gets deeper.

By increasing the groove width and varying the relative position of the focus, it could be possible to create even deeper grooves, so the actual criteria for the groove depth limit are not a specific depth value but the ratio between groove width and depth and focusing position dynamics. From these results, it is obvious that grooves with the width/depth aspect ratios of 1:3 could be fabricated using a line spiral ablation algorithm.

3.7   Significant results and conclusions

1. When the groove length does not exceed the working field size of the F-theta lens used, galvoscanner is used and laser power is raised from 2 to 5 W, the microgroove production time can be reduced by an order in compare with the system comprising linear direct-drive servomotors stages.

2. A 45 % wider crater, obtained in the case of the Hat Top beam under the same irradiation conditions (optical energy, focus position, pulse number) compared to the Gaussian beam is ablated due to higher spatial frequencies introduced by DOE, which limit the beam waist to the bigger spot.

3. The Gaussian beam produces higher quality grooves than the HT beam (produced with the diffractive optical element) in terms of wall inclination and groove nearby surface deterioration, which is an important factor for successfully realizing ultrathin conductive ceramic mesh to monitor stress and wear on steel surfaces.

4. The deepest fabricated groove with a 5 W, 270 fs-laser system, having a pulse repetition rate of 50 kHz, using a spiral ablation algorithm and a programmed width of 250 μm, had a depth reaching 900 μm. The depth of the groove saturates with increasing passes because of the interplay of worsened material removal, higher beam reflectivity from the steep walls and the decreased energy fluence due to beam diffraction.

4. Femtosecond laser ablation of titanium-suboxide ceramics in air

Material related to this chapter was published in [P1, A2, C4-C5], and its practical aim is ultrashort-laser micromachining of titanium suboxide ceramics. Specific tasks, such as microslicing, fabrication of definite, precise microholes and micro notches in ceramic fibres while maintaining their electrical properties using the developed microfabrication system were provided.

The conductive ceramic samples used in these experiments were prepared at Bath University and consisted of titanium suboxide at Magneli phase (Ti_nO_{2n-i}, where $4 < n < 10$) as was described in the second chapter. Ceramics were pressed in the form of tablets or fibres from the ball-milled TiO_2 powder and then sintered at high temperatures.

4.1 Ablation threshold of electrically conductive titanium-suboxide ceramic tablets

The machining experiments started from the evaluation of the optical transmission spectra of all the different samples of titanium dioxide ceramics, which were obtained from the Bath University. The samples differed by their colour and conductivity, however, although the samples were ground and polished off from 1 mm down to below 50 μm, it was still impossible to measure their transmission spectra due to very high absorption and possibly the scattering in the spectral range from 200 nm to 1100 nm. Therefore, the specific absorptivity of all ceramics was evaluated to be higher than 600 cm^{-1}, and the fundamental laser harmonics of 1028 nm was chosen for all experiments.

Ablation threshold fluence values for the Ti_4O_7 samples at different incident laser pulse numbers using a constant laser repetition rate of 25 kHz were measured.
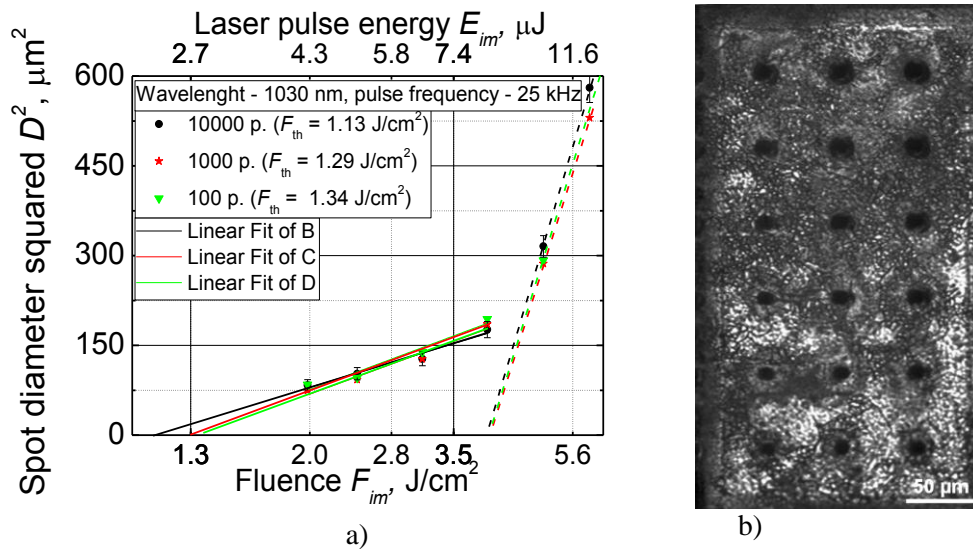
Fig. 4.1 a) Measurement of the ablation threshold fluence for various incident pulse numbers and b) figure of the ablated spot matrix (vertically – pulse number, horizontally – beam energy) in the ceramic sample.

To determine the ablation threshold at 25 kHz of the laser repetition rate, diameters of the ablation zones were extrapolated to zero fluence. In Fig. 4.1a, the extrapolation curves and measured threshold values are shown for various incident pulse numbers with error bars depicted for the case of 10000 pulses (errors for other cases are of similar magnitude and are linked with crater diameter measurements uncertainty). It was determined that at given laser repetition rate (25 kHz), the threshold fluence value (for gentle ablation) measured for 1000 subsequent laser pulses was 1.29 J/cm^2. Note that the holes created with a larger number of incident pulses are more predictable and symmetric.

From the matrix of ablated spots shown in Fig. 4.1b an incubation effect can be observed. Indeed, by affecting the same spot with a larger number of pulses the threshold reduces (e.g. from 1.34 J/cm^2 for 100 pulses treatment to 1.13 J/cm^2 for 10000 pulses). For higher pulse repetition rate (50 – 300 kHz), the incubation effect manifested itself even more, e.g. the ablation threshold for 100 subsequent pulses (at a 300 kHz of repetition rate) was reduced almost twice (to 0.61 J/cm^2) in comparison with the value obtained at 25 kHz, whereas the ablation threshold values at 50, 100 and 200 kHz repetition rates were in-

108

between. Note, that the threshold energy fluence for strong ablation regime (see Fig. 4.1a) at 25 kHz pulse repetition rate was substantially higher (~4.0 J/cm^2).

4.2   Cutting and slicing of electrically conductive ceramics

In order to evaluate the shape of trenches, grooves of various widths (as shown in Fig. 4.2) were machined using the spiral patterning algorithm. The spiral algorithm used in these experiments was the same as described in chapter 2, Fig. 2.19, where wide grooves are ablated by continuously adding new grooves side by side with some separation value (*d*) in both directions.
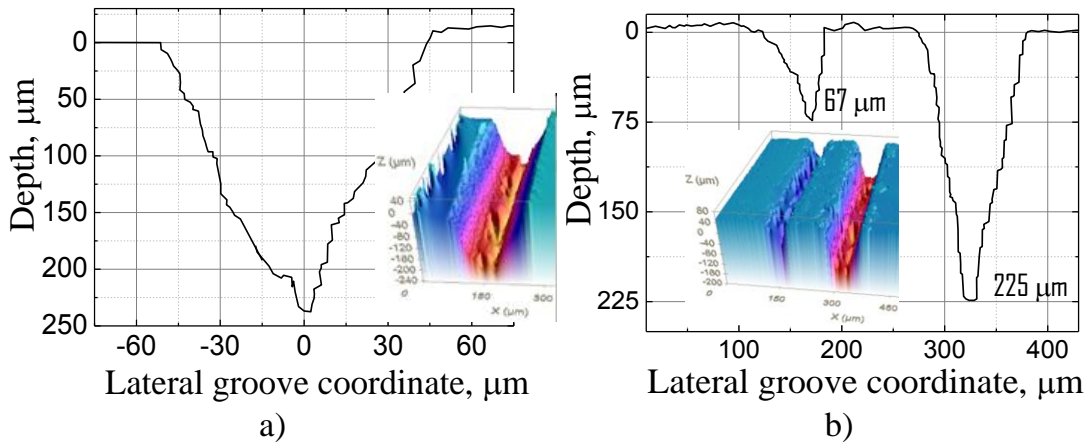
Fig. 4.2 3D micrographs and profile of grooves made in titanium suboxide ceramic samples with 25 mm focusing lens (laser power 2 W at 25 kHz repetition rate, with: a) 30; b) 20 and 27 repetitive scans and 50 mm/s scanning speed). The focusing position was on the machined surface.

All structures were formed in the ceramic sample at the fixed laser repetition rate of 25 kHz and pulse energy of 80 µJ at 1028 nm wavelength. The scanning speed was set to 50 mm/s. The beam diameter at the sample was equal to ~20 µm at 1/e^2 level. Each removed layer consisted of several transversal scans shifted by 10 µm with respect to each other. The beam focus position was on the surface.

Machined grooves are "V" shaped. The width of a groove is 60 µm at the surface and 13 µm at 90 % of its 73 µm depth (after 20 repetitive scans) and 96 µm and 27 µm of its 235 µm depth (after 30 scans), respectively. It can be

seen that the rectangularity of a groove depends on the scan number. Deeper cuts are generally more rectangular. This wall inclination was sufficient to cut the bulk samples (Fig. 4.3) to the required length and slice them to obtain trapezoid shape ceramic fibres, which were used in the wear sensor. The 7 deg wall inclination angle was achieved. The preliminary hole drilling experiments in the ends of fibres were accomplished as well, as can be seen in the bottom left part of the picture. However, further optimization of the machining process is required to obtain grooves with more rectangular shape and steeper walls.
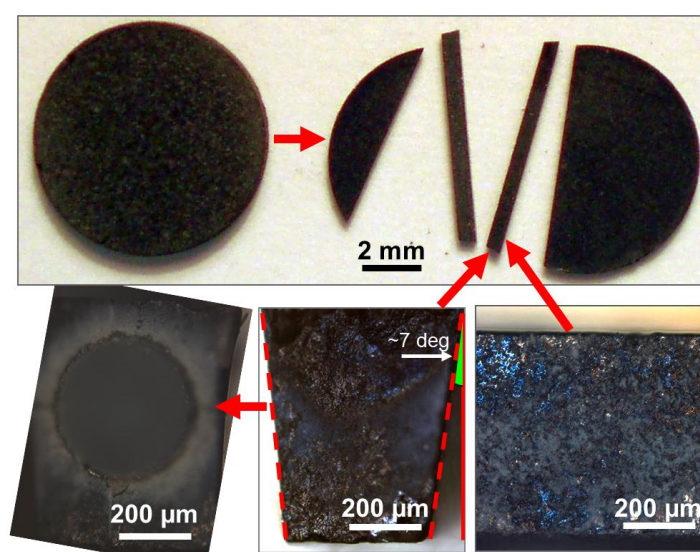
Fig. 4.3 Cutting and slicing of conductive titanium suboxide ceramics with fs-laser ablation and subsequent microhole drilling in the ends.

4.3   Notch cutting across the ceramic fibre

An example of round ceramic samples, its typical cross-section SEM image, and required hole/trench parameters are shown in Fig. 4.4. Both cutting the notch with desired parameters using the galvanometric scanner system ("moving beam" system) and drilling the holes in the centre of the fibre with linear stages ("moving sample" system) were tested.

The most straightforward way to create up to the 100 μm deep trench in the ceramic fibre for the contact attachment is to create a cut (notch), across the fibre diameter. This can be achieved most quickly with galvanometric scanners

using the spiral ablation algorithm as described in the previous chapter. This approach does not even require precise sample positioning as in the case of microhole drilling.
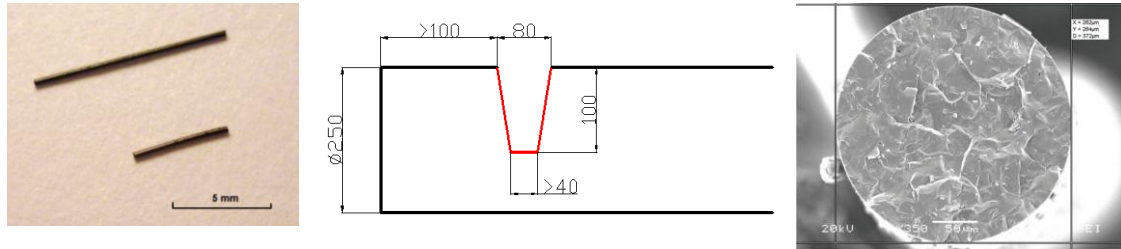
Fig. 4.4 Ceramic fibres (left), the sketch of the hole (or notch) to be made (units in µm) and SEM image of a cross-section of the fibre.

Laser power: 2W
Pulse frequency: 25kHz
Pulse duration: 300fs
Beam moving speed: 1m/s
Focusing: 100mm F-theta
Algorithm: spiral of lines
(16 lines with 5µm pitch)
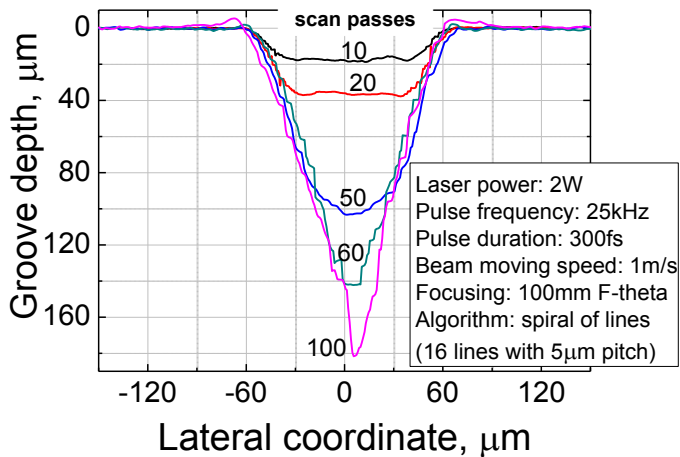
Fig. 4.5 Changes in the groove profile with a number of laser scan passes.

Two laser wavelengths 1028 nm or 515 nm were tested for this task. Other algorithm parameters are as follows: laser power – 2 W (for 1028 nm) and 1 W (for 515 nm), pulse duration – 270 fs, repetition rate – 25 kHz, number of spirals (optimized for a 80 – 110 µm wide notch) in the algorithm – 6, the distance between spirals – 5 µm, scanning speed – 1 m/s. Beam was focused with a F-theta lens, which acts as a focusing optical element and is capable of producing aberration-free spot at the wide working field with maximal dimensions 50x50 mm^2. As the focal length of such lens is rather long (100 mm), it is possible to achieve high beam scanning speed (up to several m/s). The repetition number of the entire algorithm was varied during the optimization process in order to achieve the required notch depth. In Fig.

4.6 the results of multiple experiments are shown presenting notch parameters dependence on the number of scan passes, whereas Fig. 4.5 presents typical profiles of the machined notch.
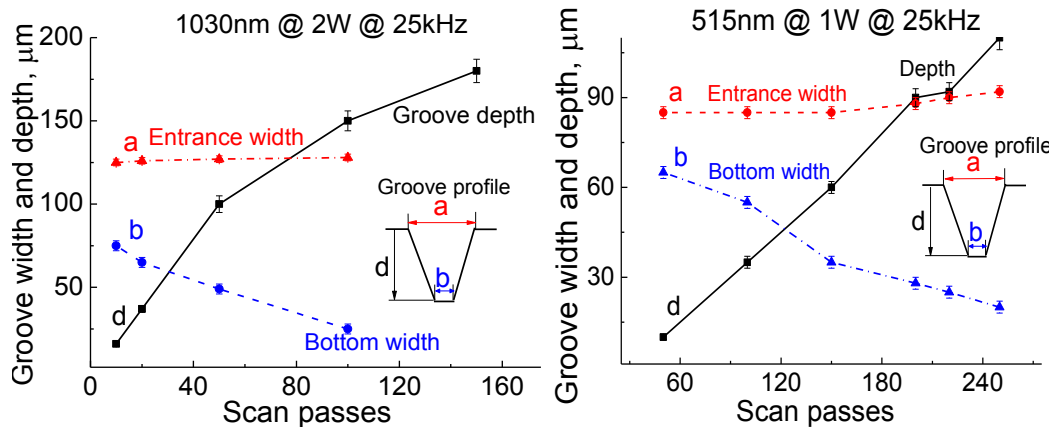
Fig. 4.6 Dependence of the notch depth on the number of algorithm repetitions for fundamental (1028 nm) and second laser harmonics (515 nm).

| 10 repetitions | 20 repetitions |
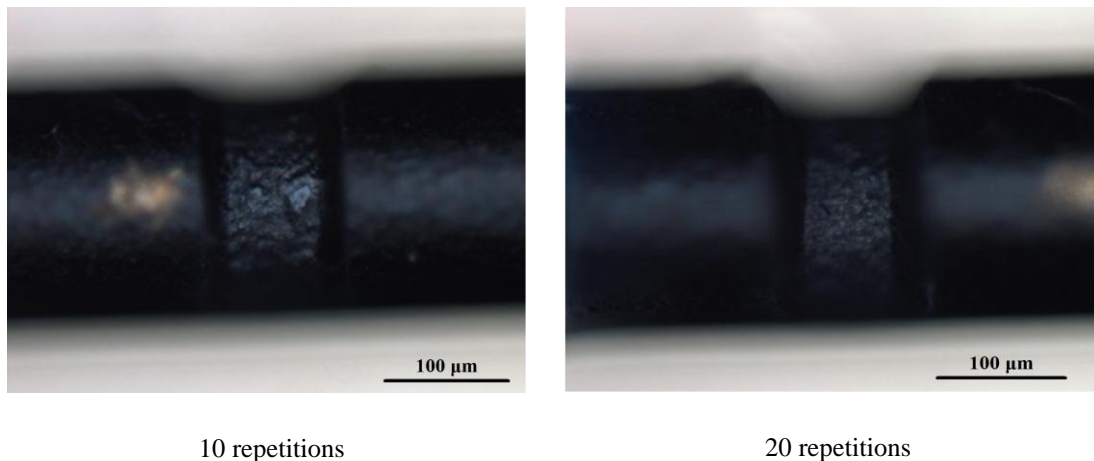
Fig. 4.7 Bright field microscopy images of notches made in Ti_4O_7 ceramic fibres. Processing parameters: wavelength – 1028 nm, power – 2 W at 25 kHz, scanning speed – 1 m/s, focused directly on the surface with 100 mm F-theta lens.

Obviously, the notch gets deeper with increasing number of repetition (see Fig. 4.6). The groove entry width is always bigger than the bottom width. When the groove gets deeper, the incident beam area increases, as well as the incident angle, and it results in the decrease of effective laser fluence and decrease or even absolute cessation of ablation. ~20° angle of wall inclination was achieved for grooves with the required depth at the available laser pulse

energy. Several pictures of the notches made at various algorithm scan passes and examined with bright field microscopy are shown in Fig. 4.7.

Table 4.1 Optimal machining parameters for the micronotches (120 x 100 µm) in titanium suboxide ceramic fibre.

Laser repetition rate	25 kHz
Wavelength	1028 nm
Pulse duration	270 fs
Laser power	2000 mW
Polarization	p
Scanning speed	1000 mm/s
Focusing lens (F-theta)	100 mm
Focusing depth below the surface	0 µm
Lines in a spiral	24
Distance between adj. lines	5 µm
Algorithm scan passes	40
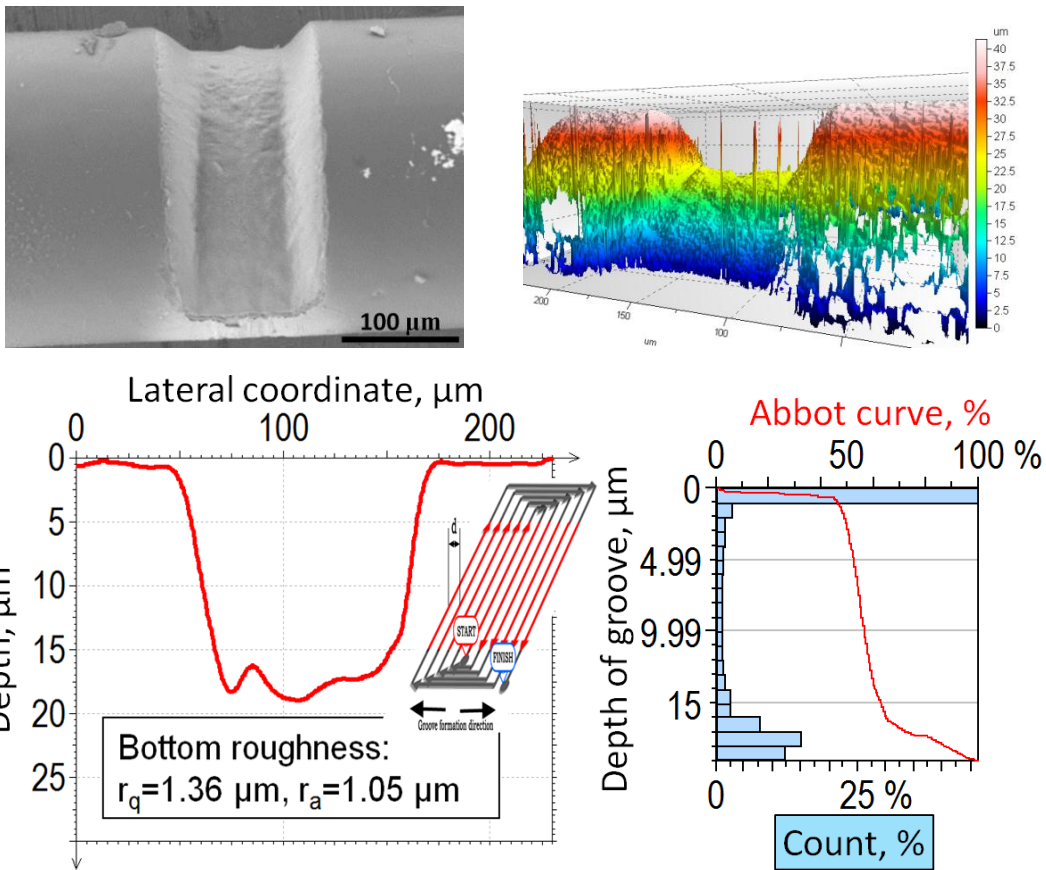
Fig. 4.8 Fabrication algorithm (bottom left corner) and the resulted typical averaged profile of notches inspected with optical profilometry (3D, Abbot [red curve] and depth distribution [blue columns]).

It was found that the optimal repetition number of the spiral algorithm to produce the 100 µm deep grooves is 40 for the first harmonics when the other processing parameters are as indicated inTable 4.1. Note, that the quality of the

113

trenches was comparable in both cases when using 100 and 200 scans for the machining at first laser harmonics (1028 nm, 2 W) and second harmonics (515 nm, 1 W), respectively. Machining using shorter wavelength increase required production time 2 times, due to the dropped laser power.

A result of a typical groove morphology investigation with the confocal profilometer, scanning electron microscope, as well as statistical software is shown in Fig. 4.8. SEM micrograph, 3D image and notch profile are self-explanatory. The bottom right graph Fig. 4.8 shows the depth distribution of the machined groove. At the same graph is also depicted Abbott-Firestone curve, which describes the surface texture of the groove.

It should be noticed, that the processing time for one notch with the fundamental harmonics was less than five seconds, so the manufacturing process is relatively fast (in compare with the micromachining using linear servomotor stages). Also, parallel microfabrication on multiple fibres lying side by side can be done simultaneously in this setup and requires almost the same manufacturing time.

4.4   Trepanning drilling of microhole in ceramic fibres

For microhole drilling, the modified "movable sample" system setup was used. In this case, maximum precision of beam positioning can be achieved, which is not easily in the "movable beam" setup implementing a low numerical aperture F-theta lens. Furthermore, a visualization system was essential because precise fibre positioning before the micromachining was necessary. A microscope objective with NA of 0.2 (the focal length - 25 mm) was used as a focusing optical element. Holes were drilled by the treppaning algorithm similar to the previously discussed the spiral algorithm: the sample was moved in a circular trajectory with constantly increasing radii as depicted in Fig. 4.9.

The number of circles in this algorithm determines the diameter of a hole, while sufficient hole depth is achieved by additional repetition of the algorithm. Holes of various sizes are shown in Fig. 4.10.
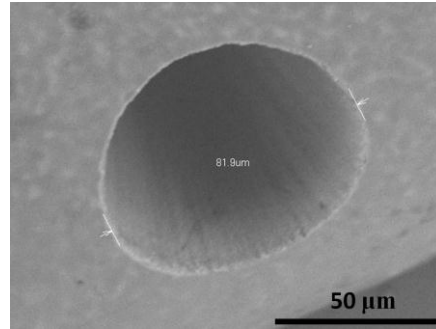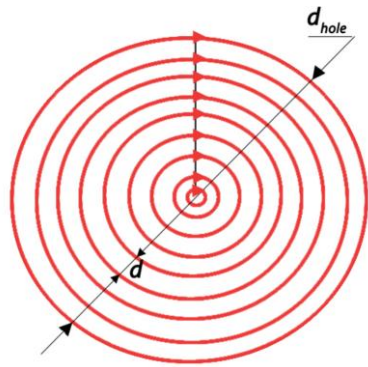
Fig. 4.9 Circle patterning algorithm (left) and the SEM micrograph (right) of the microhole drilled in ceramic fibre.
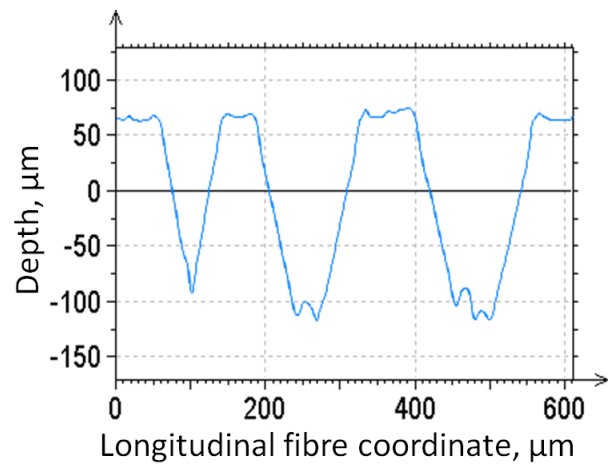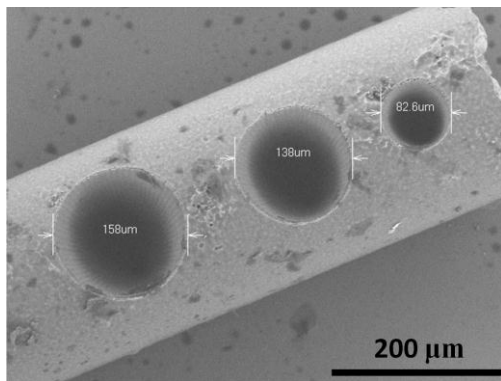
Fig. 4.10 Holes of various sizes drilled in ceramic fibre: SEM picture (left), and profiles along the fibre (right).
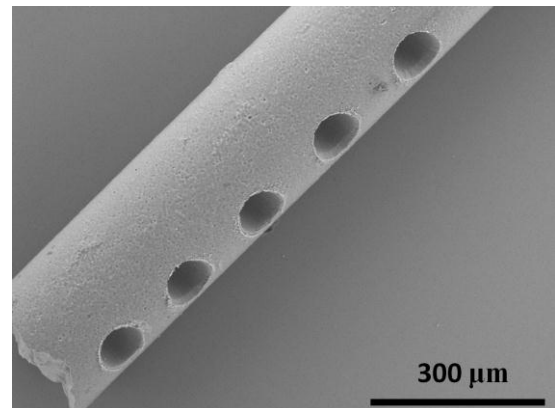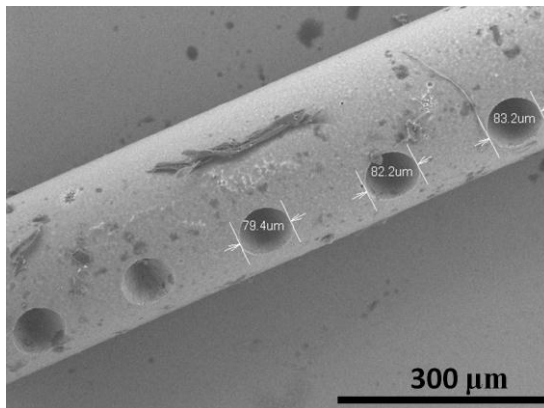
Fig. 4.11 Processed fibre before (left) and after ultrasonic washing (right).

Optimal holes for the strong attachment of the thin silver electrical wire to the ceramic fibre should have a diameter of 80 µm and depth of 100-150 µm. Table 4.2 presents the experimental parameters to achieve such a hole.

115

As can be seen from Fig. 4.11, microholes have good repeatability. However, because of the inertia of the linear servomotor stages, the fabrication of microholes took long to be feasible for the industrial applications.

Table 4.2 Hole drilling parameters.

Laser repetition rate	25 kHz
Wavelength	1028 nm
Pulse duration	270 fs
Laser power	50 mW
Polarization	Linear
Scanning speed	1 mm/s
Focal distance of lens	25 mm
Focusing depth below the surface	0 mm
Circles in a spiral (for 80 μm hole)	16
Distance between adj. circle	5 μm
Algorithm repeats	50
Drilling time for one hole	5 min

Fig. 4.12 Optical scheme of the experimental setup for microhole drilling using SHG and f-2f-f imaging system. λ/2 – ZO half wave plate, P – thin film Brewster type polarizer, BD – beam dump, M1-M3 – dielectric HR mirrors, L1-L2 – imaging lenses, BS – beam splitter, HG – harmonics generator, PhD – illuminating photodiode, CCD – process vision camera.
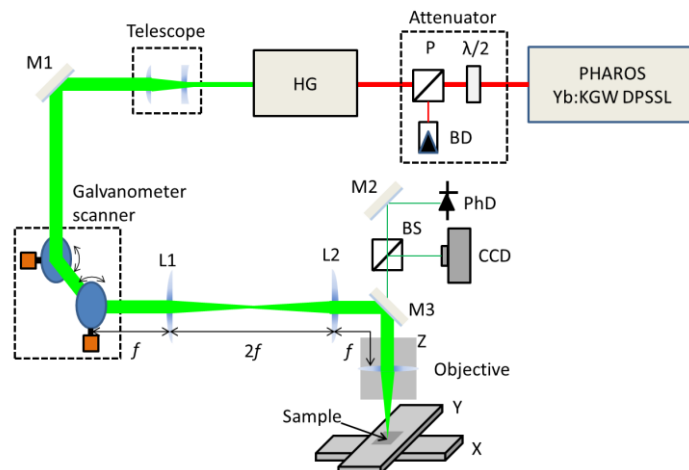
Therefore, the "movable beam" scheme was modified for this particular task (as the structure dimensions do not exceed the field of view of the objective). A 4f imaging system, consisting of two 2" AR/AR coated lenses of 250 mm focal length each was utilized for these tasks. Lenses relayed the angular beam deflection from the galvoscanner mirrors to the objective entrance plane without changing the axial beam position. The change of beam incident angle onto the objective aperture enables a beam waist shift in the focal plane. The distance between the scanner mirrors, lenses comprising a 4f

system and the objective are determined by the focal distance of the lenses and is equal to $f - 2f - f$ respectively (the case when both lenses have identical focal distance f). The working field D of such a system is twice the maximal beam shift distance Δx on the sample surface:

$$D = 2\Delta x = 2\frac{f_1}{f_2}(f_1 + f_2)\text{tg}(2\alpha_{max}), \qquad (4.1)$$

where f is the lens focal distance and α_{max} is maximal beam deflection angle, limited either by lens aperture or by maximal deflection of the scanner mirror.

Optical scheme of the modified "movable beam" setup is depicted in Fig. 4.12. In this configuration as in the previous setup, beam spot size is determined by the focusing power of the objective ensuring the required resolution. Although the working area has become much smaller (approx. 300 μm in diameter) and the focused spot was prone to spherical aberration at the field extremes, working field of this setup was sufficient to carry out the micromachining tasks on the fibres.

4.5   The quality of the drilled microholes

Machined fibres were inspected with optical brightfield microscopy, optical confocal profilometry and scanning electron microscopy. As can be seen from the pictures Fig. 4.13, Fig. 4.11, the overall hole quality was satisfactory. The most important aspect is the absence of melted slag at the hole boundary. Such slag is always present in micromachined samples done with nanosecond or picosecond duration laser pulses. Melted material can also have different physical properties (for example loss of conductance) and is undesirable. It is obvious that fs micromachining does not have this drawback only when the right machining parameters are chosen (e.g. Fig. 4.14).

Material (debris), removed from the holes during laser machining, tends to stick to the surrounding surface, as is clearly shown in Fig. 4.10 and Fig. 4.14. However, it can be quite easily removed using the ultrasonic bath cleaning procedure. The difference after this procedure is demonstrated in Fig. 4.11. Nevertheless, washing should be performed with caution, as such ceramic

material is very brittle. And in the case of deep holes, ultrasonic vibration in the bath breaks the fibre. Best results were obtained in heated water (>70° C) with the addition of special liquids for ultrasound cleaning.
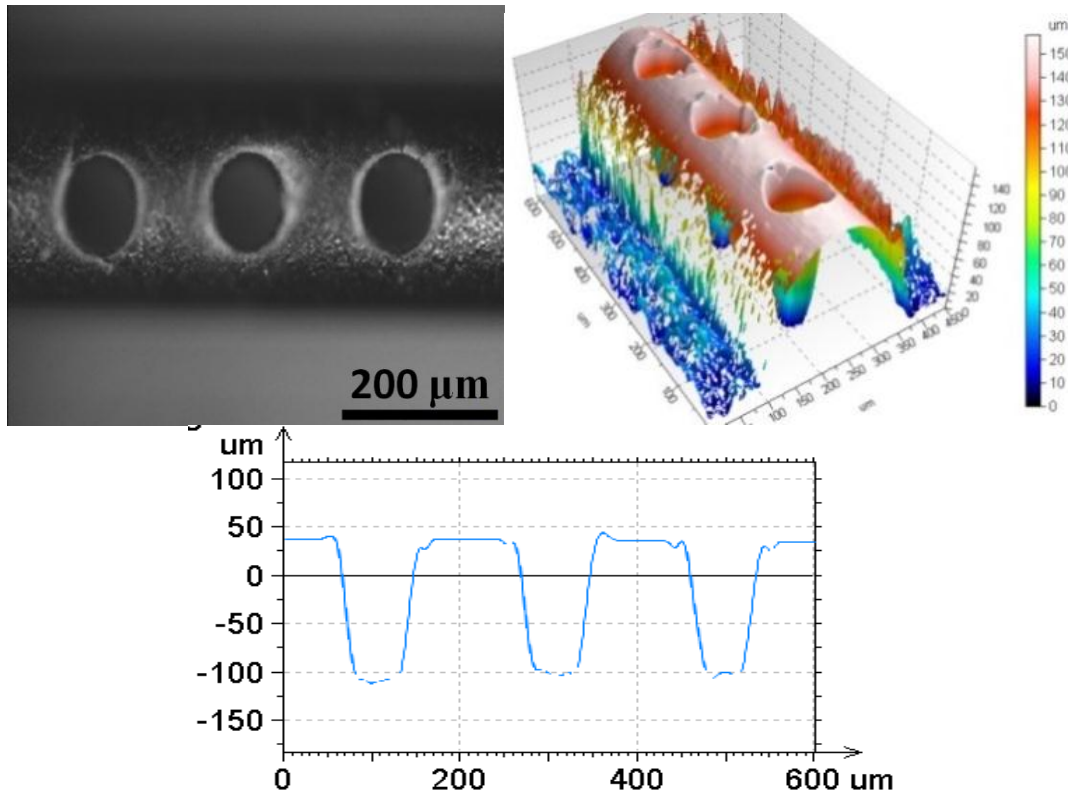
Fig. 4.13 80 μm diameter holes drilled in titanium suboxide ceramic fibre: bright field images and confocal profilometry (3D topography and profile along the fibre).

Closer inspection of the holes reveals some irregularities; however, they are small and do not affect electrical properties of the material. Some small amount of debris is still present near the holes boundary. Sometimes, microcracks can form in the fibre, small areas of possibly melted material are visible, but these
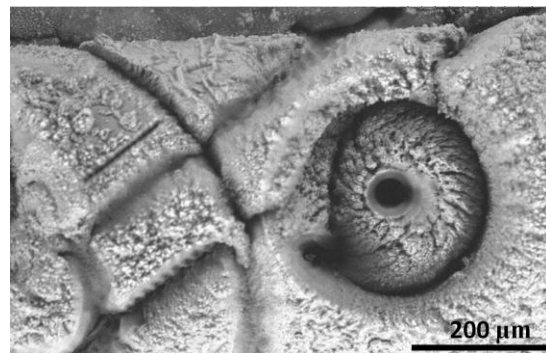
Fig. 4.14 Hole machining example with wrong process parameters: P_{av} = 1.2 W, v = 10 μm/s, 14 repeats.

118

zones do not exceed 6 μm as can be seen in Fig. 4.15 and do not impact on conductive properties of the ceramics. Microhole bottom roughness was estimated to be not greater than 4 μm (RMS).

Debris	Melted zone	Microcracks	Melted slag
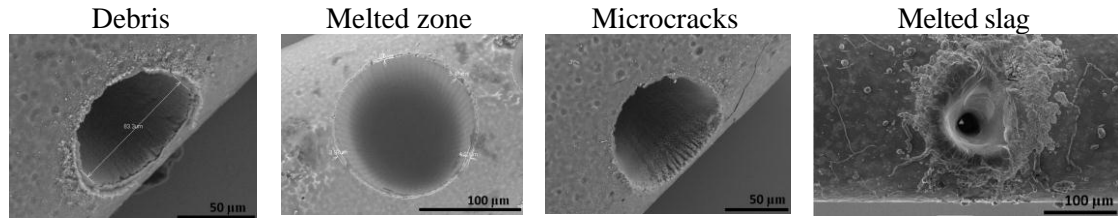
Fig. 4.15 Closer look at the drilled holes with various possible irregularities. Remelted slag formed at the boundary of the ablated well when fabricated with too high pulse power and repetition rate.

The absence of slag is the key result in this experiment. Slag is present when the material is micromachined with ns or ps duration laser pulses. Melted material experiences strong thermal stress and could have different physical properties (for example, loss of conductance) and is undesirable here. Similar slag could also appear when processing with fs-laser pulses. If the laser repetition rate is set too high or too high fluence is selected, thermal accumulation may develop in the material resulting in sufficient temperature increase for consequent melting. For example, a microhole drilled for about 120 seconds with 1.6 W laser power at 100 kHz pulse repetition rate with the SH wavelength is shown in Fig. 4.15. The quality of this microcavity is much worse. Visible slag of melted material is clearly present. It was not possible to create a desirable electric contact, in this case, as infinite resistance (>20 MΩ) was observed between the contacts. It was realized that when the density of pulses on one spot per second is too high, drilling through the fibre leads to overheating and loss of conductivity in the holes region, probably because of surface layer complete oxidation. This demonstrates that the melting of ceramics is possible, and should be avoided, as this area looses its conductive properties.

4.6   Resistivity analysis of ceramic fibres with soldered contacts
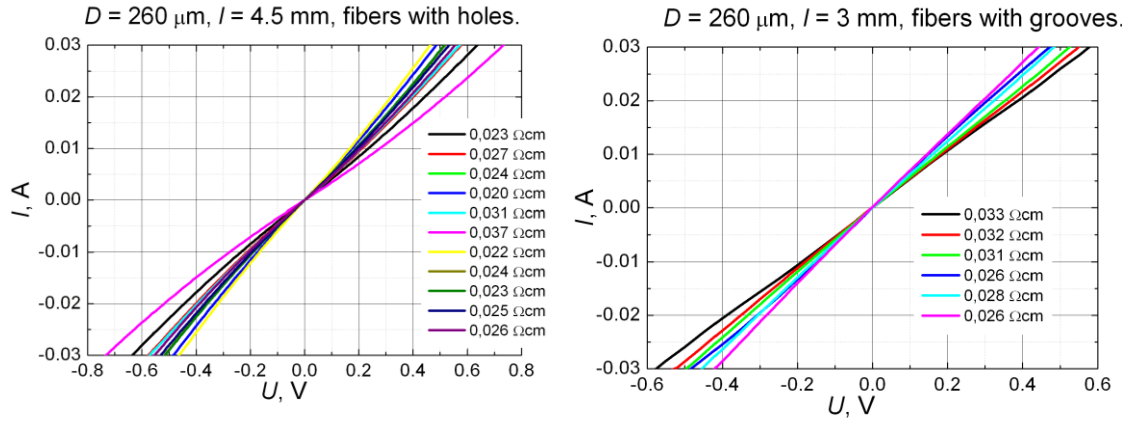
Fig. 4.16 Current-voltage characteristic of fibres with different wire attachment approaches.

Table 4.3 Average specific resistivity of investigated fibres.

Contact type/Number of samples	Average specific resistance ± standard deviation, m$\Omega \cdot$cm
Side contacts/8	28 ± 5
Microhole contacts/6	26 ± 5
Micronotch contacts/11	29 ± 3

Liquid aluminium and platinum pastes were used as a solder alloy to attach the 40 or 60 μm diameter metallic wires to the ceramic fibre. Platinum, aluminium, and silver contacts were tested with the latter proving to be most reliable. 2 types of micro structured bonding (microholes and notches) were compared with wire bonding to the side of the ceramic fibre. The latter proved to be very poor as regards mechanical strength. After the paste was spread on the bonding area and preliminary wire soldering accomplished, contact annealing in N$_2$ atmosphere at 700$^{\rm o}$ was performed for half an hour.

The quality of the contacts was observed with an optical microscope and tested by measuring the current-voltage characteristic of the multiple samples using an Agilent E5270B precision measuring mainframe (0.1 fA – 1A range for current and 0.5 μV – 200 V range for voltage mesuarment with 0.5 μV, 0.1 fA resolution). The DC resistance (R) of the sample was calculated from the linear part of the current-voltage characteristic for each sample, and average specific

resistivity, which was important parameter of the contact quality, was evaluated for each group of samples with different contact bonding method:

$$\rho = R\frac{\pi D^2}{4l}, \tag{4.2}$$

where D is a diameter of the fibre and l is the distance between contacts.

The final results depicted in Fig. 4.16, indicated that all the fibres showed very similar specific resistivity (Table 4.3). This proved that the material sustains all its conductive properties after micromachining with the fs-laser.

4.7 Significant results and conclusions

1. The developed ultrashort pulse laser micromachining system was successfully adapted for titanium suboxide ceramic microfabrication tasks including cutting up to 1 mm thick, microhole trepanning and micronotch fabrication.

2. The laser micromachining of notches and holes in ceramic fibres for electrical contacts was carried out using both types of systems ("movable sample" and "movable beam").

3. Processing parameters for ceramics microfabrication were optimized for minimal heat affected zone and the resulted heat affected zone achieved was smaller than 6 μm.

4. Specific resistances of the ceramic fibres processed with a femtosecond laser with aluminium based solder and silver wires fixed in machined micro trenches and microholes were in the range of $21 - 35$ mΩ·cm. This coincides well with the conductivity of the unprocessed fibres and leads to the conclusion that femtosecond laser machining does not influence conductivity of the material.

5. The fabrication of notches in titanium suboxide ceramic fibres is simpler, faster and more straightforward in comparison with the blind hole trepanning drilling.

5. Femtosecond ablation under a thin liquid buffer layer

Material related to this part of the dissertation was published in articles [A3-A5, A8, A9] and proceedings [C6, C7].

The chapter aims to propose the feasibility of thin water layer assisted femtosecond laser ablation in the case of non-transparent materials and presents microcutting, microdrilling and groove formation results on various materials: steel, copper, invar foil and magnetic material (neodymium alloy). It is demonstrated that the addition of a thin water layer on top of the samples during ablation results in superior throughput and femtosecond laser machining quality due to the additional spatial transformation of ultrashort pulses as well as cooling and cleaning properties of the covering fluid. Experimental evidence of filament formation is presented by laser-induced damage patterns of a thin chromium layer.

5.1 Experiment setup

The laser beam was focused using an F-theta lens (f = 100 mm) above the sample, which was covered with a water layer so that filament formation can occur near the interface of the samples. The chosen parameters were as follows: laser repetition rate 33 kHz – 200 kHz and an average optical power P = 10 W. For copper foil cutting experiments, 5 W were used. In the experiments with thin film chromium layers, single laser pulse with 2 – 18 µJ energies was used. Schematics of conventional (standard) beam focusing and focusing through water layer are shown in Fig. 5.1 (a,b). In both approaches, 100 mm focal length F-theta objective was used.
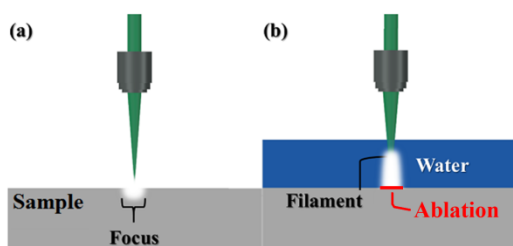
Fig. 5.1 Different beam focusing approaches by femtosecond laser micromachining: (a) standard focusing, (b) focusing through water buffer layer. Picture adapted from [177].

122

Fig. 5.2 presents simplified CAD drawing of the setup, showing principle and geometry of the experiment. The scanner served as a beam scanning apparatus. 3D motion stages with stepper motors were used to adjust the sample height position as well as to extend the available working field. Laser power was controlled either by using a motorized half-wave phase plate and Brewster type polarizer or by tailoring the voltage of the output Pockels cell. Variable beam expander 1.5x – 8x was used to enlarge the beam to fill all the available optics aperture.

Fig. 5.2 Simplified CAD drawing of the optical setup, showing principle and geometry of the experiment.
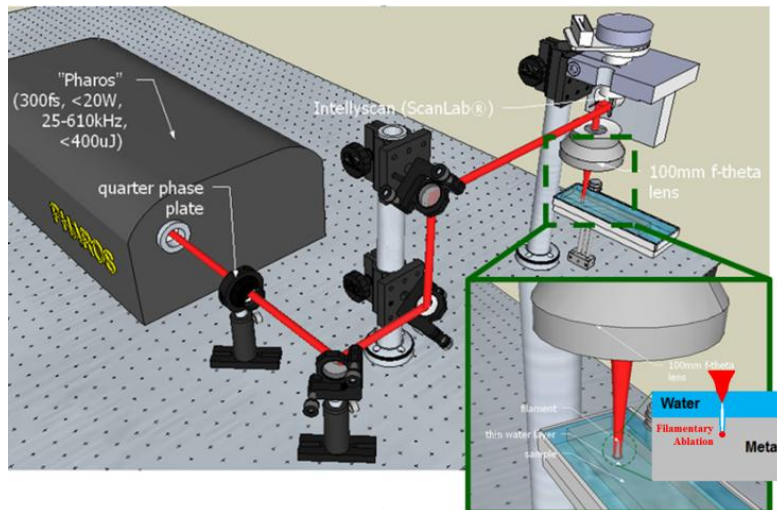
The water layer was formed by submerging the samples in a reservoir. The thickness of this film was measured by shining a beam from a green laser onto the surface of the water film and measuring how the position of focused and reflected beam (from the water layer) changes on a CCD array when more or less water is poured into the reservoir. It was found that the thickness of the water layer could be determined to an accuracy of about ~10 μm with this method.

5.2 Influence of liquid on the morphology and ablation rate

Fs-pulses, in contrast to longer pulses, undergo a nonlinear transformation during self-focusing in water. The intense (in given experimental conditions I ≈ $3 \cdot 10^{14}$ W/cm^2) pulse self-focuses in transparent media (water), it increases

ablation efficiency, enables thick (up to 2.5 mm) sample cutting, and decreases thermal damage to the sample and debris repositioning. To compare morphology difference produce by DLA and FPF machining grooves were machined with both techniques under the same experimental conditions on a polished steel sample (oxidized steel alloy FE220323, Fe/Cr18/Ni10, 50x50x8 mm dimensions), the only difference is that in the second case, the buffer liquid layer was used: distilled water (pure deionized water with a resistivity of >18 MΩ cm); acetone (CH_3COCH_3 ≥99.8 %, from Sigma-Aldrich); or methyl alcohol (CH_3OH ≥99.8 %, from Sigma-Aldrich). Other experimental parameters were the same.
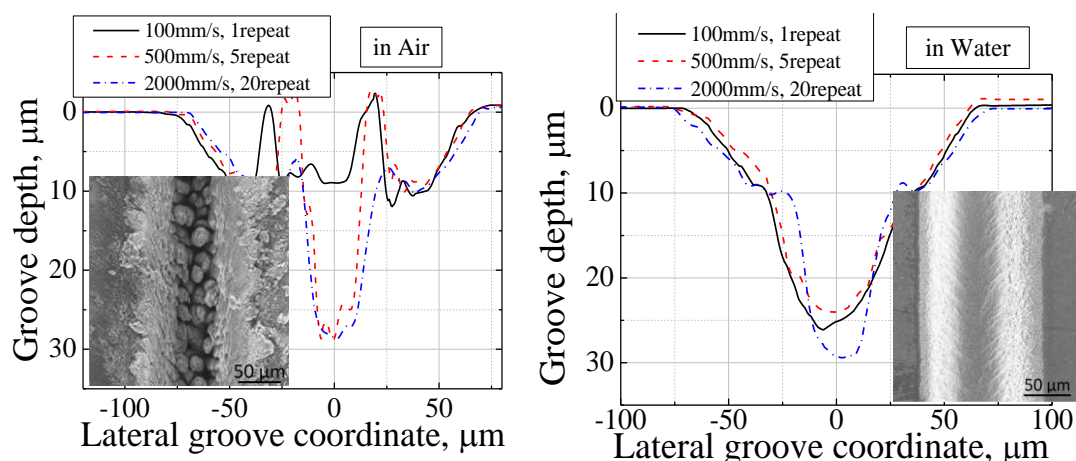
Fig. 5.3 Average groove profile, showing the impact of the liquid layer on the groove depth and morphology in the ablation process of steel.

Beam focus was held on the surface of the static sample. The laser beam was scanned with 100, 500, 1000 or 2000 mm/s speed along a 20 mm line repeating the exposure 20, 100, 200 or 400 times accordingly, so that the overall groove machining time was the same. Other experimental parameters were 1028 nm, 270 fs, 5 W, 25 kHz; spot diameter ~18 μm at FWHM; energy fluence ~40 J/cm², beam delivered by galvoscanner and focused with 100 mm f-theta lens. 1 line pattern was scanned repeatedly. Fig. 5.3 shows typical average groove profiles.

124

When the beam scanning speed was slow (<100 mm/s), one of the shortcomings of DLA in the air became evident. The bottom surface of the machined groove was glossy, shining (observed through an optical microscope). This witnesses that the melting and liquid material dynamic processes took place. Also, the deposition of energy on the sample is very fast (fs-laser pulses are used) and the repetition rate of the pulses is not high (25 – 100 kHz), so that there is enough time to spread the thermal energy from the surface into the bulk of the sample, melting still occurs when high energy pulses are used. Particularly central part of the groove becomes very unregularly when micromachined in the air. On the other hand, the grooves produced using the same algorithm and a thin liquid layer above are smoother, with no ablation debris, and also showing no signs of thermal affection (insets on Fig. 5.3). This is caused by improved cleaning of the groove bottom from the ablation particles by a water shock wave [117] as well as generated high-pressure steam. Furthermore, in the case of filament-assisted ablation, the groove morphology, as well as depth, do not depend so critically on the beam scanning speed and the pulse density as in the case of ablation in the air. Going into details, the grooves machined in the air are 8 % wider than the grooves produced under water. Water was found to be the best buffer liquid because the depth of grooves machined under water is 20 % and 10 % larger in comparison with the grooves machined under methanol or acetone. This could be caused by different nonlinear absorption of liquids. Furthermore, water is not flammable, and its vapour is not toxic.

Fig. 5.4 The front surface of sprockets cut from 1 mm stainless steel with the filamented laser beam in acetone (on the right side of picture) or in water (on the left side of picture).
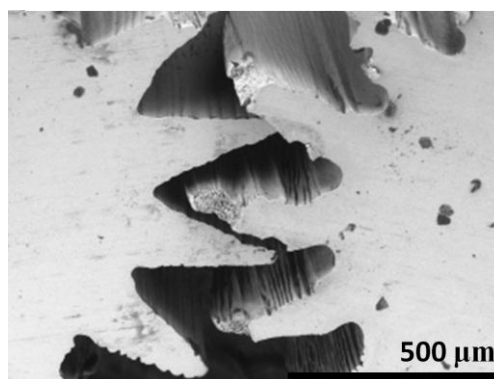
Fig. 5.4 shows a multiple-tooth-sprocket cut from 1 mm sheet metal under an acetone layer (right sprocket) and under a water layer (left sprocket) with all other experimental parameters identical (25 kHz, 350 μJ, 800 mm/s, liquid thickness 0.5 mm). It is evident that the sprocket cut under water has teeth of better quality than the one cut in acetone.

5.3   Ablation thresholds of steel in liquid

To further understand the difference between the filament-assisted and air ablation, as well as to determine single pulse crater size on the surface, the ablation threshold of polished stainless steel was measured by both techniques. Single as well as multiple pulse exposure experiments were carried out and gentle as well as strong ablation thresholds were determined.

Due to the nonlinear transformation of the spatial intensity distribution during the beam propagation in water, the standard definition of ablation threshold (defined for Gaussian beam distribution) is no longer applicable. Therefore, for the experiments described here, the ablation threshold is defined as minimal fluence, which impinges the water layer, for which metal surface damage occurs.

Fig. 5.5 shows the results obtained for a single pulse and 10 pulse thresholds. The ablation threshold in the air, especially for the case of a single-pulse ablation, has two distinct areas of different rate, resulting in gentle (below ~0.7 - 1 J/cm^2) and strong (above 5 J/cm^2) ablation areas. It should also be noticed that both ablation thresholds decrease when multiple pulses are used. These results are similar to the results obtained by other groups [178-180]. The threshold fluence in water was the lowest compared to methanol or acetone (data not shown) in the multiple-pulse case. However, when compared with the threshold in the air, under single pulse exposure the gentle ablation threshold under a 0.5 mm water film is 1.5 times higher in water. This could be partially caused by the Fresnel reflection from the air-water interface and be mainly due to multiphoton absorption in the liquid layer.

126
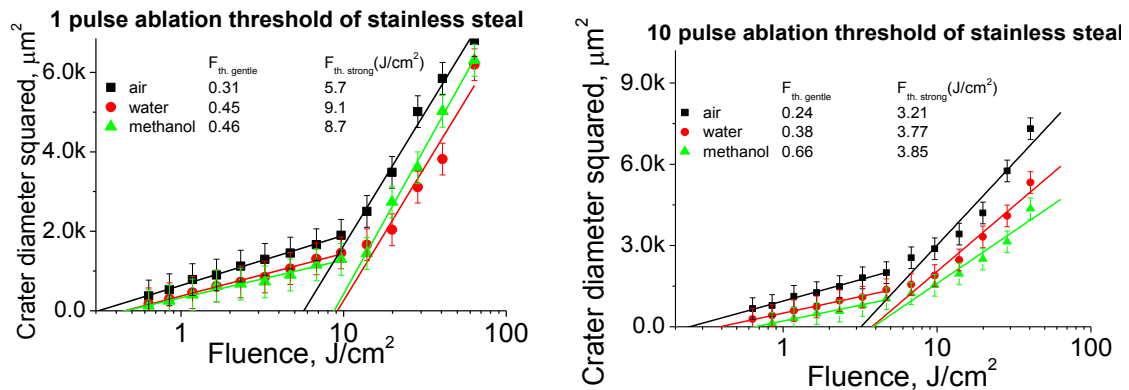
Fig. 5.5 Comparison of the ablation threshold of a polished stainless steel in the air and under a thin (0.6 mm) layer of liquids.

Dependence of the ablation threshold on the surrounding medium and on the irradiating pulse number is explained by the higher pressure of the confined plasma and shock waves [119] and an incubation effect [62]. Generally, both ablation thresholds should decrease with the increasing pulse number. The experiments confirmed this hypothesis. However, at 100 pulses, as well as at 1000 pulses (curves not shown here), the distinct separation of the ablation regions is impossible because the crater diameter dependence clearly shows a steady, gradual increase and not two regions with their logarithmic nature. This may be caused by sample heating. Despite this difficulty in traditional interpretation, some facts should be mentioned. The low energy ablation threshold in the case of multiple pulses is almost 2 times higher than the threshold in the air. In high energy regime, the water layer is significantly modified by the laser beam, the cavitation process and dynamic flow processes. These were observed in recent shadography experiments [181, 182] and may have an impact on the decreasing difference between two thresholds in strong ablation regime. In any case, the important result is that for the strong ablation regime, both ablation thresholds in the air and under a water layer are approximately of the same value (about 3.1 J/cm^2).

5.4   Single pulse chromium film ablation under water

To further extend the understanding of what is happening with the laser beam between the air-water interface and the sample surface, an investigation was undertaken to see how the beam propagates under water and whether nonlinear transformation actually takes place. As the beam intensity is too strong for any CMOS CCD camera, other means of detecting the transverse distribution avoiding imaging have to be taken. The simplest way to observe the transversal structure of the beam is to let the beam impact material surface. A thin metal film was used as a beam transformation detector. The film was exposed to laser pulses, and damage patterns were examined. The idea was to gain information from the modification of the film about the transversal beam structure and the intensity distribution. After each laser pulse, the beam was directed to a new yet undamaged chromium location, water layer thickness and sample height were changed. The pulse energy was changed as well, and single-pulse ablation patterns on glass coated with the metal film were obtained. The sample (70 nm thick chromium film sputtered on a 4 mm BK7 substrate) was immersed in water to a depth of the $300 - 3000$ μm. The thickness of the water layer was varied either by pouring or discharging water from the reservoir with the stationary sample or by controlling the immersion depth of the sample. The film was exposed to laser radiation, and the impact was examined with an optical profilometer as well as SEM.

In order to numerically model the behaviour of the pump beam in focusing Kerr media, simulations were carried out by using an extended paraxial model, neglecting time-dependent effects, electron plasma generation and related defocusing effects. Despite its simplicity, the physical model used describes both key features of asymptotic (evolution of the beam filaments and its surrounding rings) and transient regimes [183].

The evolution of a linearly polarized beam propagating with a central frequency ω_0 and wave-number $k = n\omega_0/c$ was considered in this simulation. Here $n = 1.326$ is the linear refraction index of the water at a propagation

128

wavelength of $\lambda = 1028$ nm. Since multiple filamentation involves a complete break-up of the beam's cylindrical symmetry, the complex scalar envelope $A(x,y,z)$ of the beam in a nonlinear medium with included diffraction, Kerr nonlinearity and nonlinear losses due to multiphoton absorption (MPA), evolves according to the modified nonlinear Schrodinger equation in $(2 + 1)$ dimensions. In the frame of the adopted paraxial approximation moving at group velocity $v_g = [\partial k(\omega)/\partial \omega]^{-1}$, the resulting equation for the field amplitude, $A(x,y,z)$ reads:

$$\frac{\partial A}{\partial z} = \frac{i}{2k}\left(\frac{\partial^2 A}{\partial x^2} + \frac{\partial^2 A}{\partial y^2}\right) + \frac{i\omega_0 n_2}{c}|A|^2 A - \frac{\beta^{(K)}}{2}|A|^{2K-2}A. \tag{5.1}$$

where z is a distance of propagation, $n_2 = 4.1 \cdot 10^{16} W\,cm^{-2}$ is the nonlinear index of refraction and $\beta^{(5)} = 10^{-47} cm^7 W^{-4}$ is the multiphoton absorption (MPA) coefficient. In the simplest (atomic) case, this coefficient ($\beta^{(K)}$) (where K is the number of photons involved in the process) may be estimated from the Keldysh formulation [184]. However, this model does not include the above-threshold ionization effect *(i.e,* absorption of more photons than are required for ionization by valence electrons) and the accuracy of such estimations often fails for high-intensity ultrashort pulses. Alternatively, the MPA coefficient can be deduced experimentally [126]. The intensity distribution of the incident beam was taken according to an experimentally measured beam pattern with an initial amplitude at the maximum $A_0 = \sqrt{2P_{cr}/\pi\omega_0^2}$, beam waist ω_0 and infinite initial radius of curvature. This nonlinear differential equation was solved numerically using the split-step procedure to separate the nonlinear and dispersive parts inside each step. The results of the modelling are displayed and compared with the experimental results (Fig. 5.6) in Fig. 5.7.

Firstly, it should be stated that the ablation patterns under the water layer differ significantly from the damage patterns obtained in the air. Fig. 5.6 in particular, shows some interesting result from this comparison. The upper row shows the single pulse damage patterns on the BK7 substrate coated with chromium film when the ablation took place in the air. Whereas the lower row is the same experiment, but the 1.2 mm thick water layer was added on top of

the sample. In the upper row, when the water layer was absent, more or less symmetrical damage of chromium layer can be seen as a circle with black boundaries on a grey undamaged film background (areas with completely evaporated film). Inside this circle, dark spots of various sizes can be clearly distinguished (glass surface damage), when the pulse energy is increased, or the chromium layer is brought nearer to the focus, the area of chromium film damage expands, which means that intensity at the periphery of the beam becomes sufficient for film removal. However, not only chromium was evaporated during the ablation process but also the glass under the film was damaged. The damage starts at the points, where impurities or glass inhomogeneities are present and looks like the black spots of various sizes in the circle.
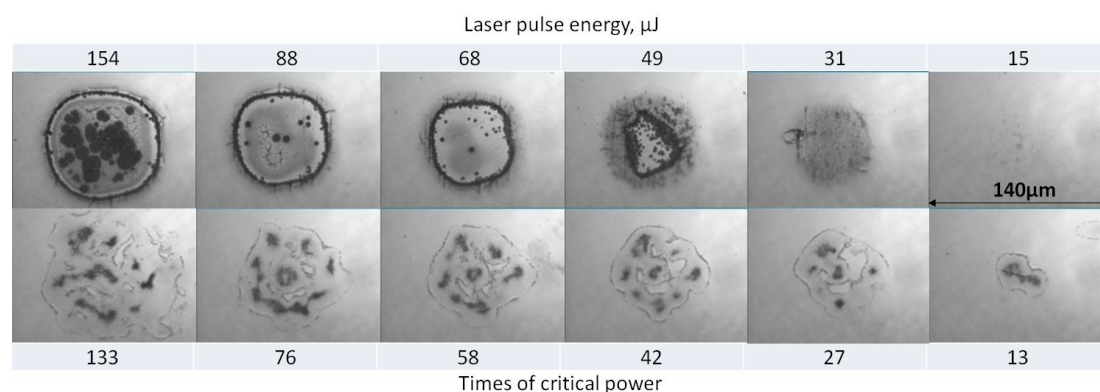
Fig. 5.6 Single laser pulse impact on the 70 nm thick chromium layer, emphasizing the key role of the water layer in the process of beam spatial transformation and multiple filament formations. The upper row is the single pulse damage patterns obtained in the air, lower row – using 1.2 mm thick water layer.

The case with a water layer (bottom row) is more interesting. The damage pattern differs significantly from the damage in the air. Due to self-focusing and laser beam squeezing in water, definite chromium layer damage appears in water at smaller energy. In water, the damage has a characteristic dot patterns. These dots are 15-25 μm wide and represent areas, where the chromium layer was modified or damaged. They represent the transversal structure of the nonlinearly transformed beam. For certain pulse energies, it definitely looks like the beam was nonlinearly transformed from the initial Gaussian shape

130

(TEM$_{00}$, beam quality factor $M^2 < 1.2$) into a multifilament beam with generally a non-central symmetry structure through nonlinear interaction between the intense femtosecond laser beam and water. For example, when the laser pulse energy is 49 μJ, the beam transforms into an asymmetric array of filaments consisting of a central filament and seven filaments around it.

The dots inside this figure represent damages to the glass surface. This experiment substantiates the hypothesis which even at relatively small fs pulse energies (a few μJ at 270 fs), the fs beam passing through a thin layer of liquid can be significantly transformed and filamented. In addition, for high pulse energies, the damage pattern is not symmetric and appears chaotic. However, the beam resulting in this complex damage structure is definitely not chaotic. The chromium-film damage pattern is exactly repeatable at different sample locations when other experimental parameters (pulse energy, water layer thickness, focusing, etc.) does not change. Another experiment (also not shown here), with multiple laser pulses impinging the same spot of the sample, showed that the transversal beam structure does not change significantly and stays stationary at least for few laser pulses (up to 5 pulses at 10 kHz repetition rate). All the pulses develop and contribute to the same ablation pattern revealing the same transversal beam structure.

Numerical reproduction of such nonlinear behaviour of the beam requires exact characterization of the beam, which is not an easy task. This involves measuring not only the transversal intensity distribution but also the beam phase front. During the modelling of this experiment, the following assumptions were made:

- the transversal intensity distribution of the beam does not change during focusing (initial beam has the Gaussian distribution),
- the phase-front at the focus is perfectly flat.

Modelling results for this phenomena qualitatively yield similar results. Images of the ablation pattern and corresponding numerical modelling results are displayed in Fig. 5.7. When the actual beam transverse intensity distribution

measured before focusing is used as an input laser beam with a strictly flat phase front curvature, the experimental ablation patterns match the numerically generated intensity distribution patterns.
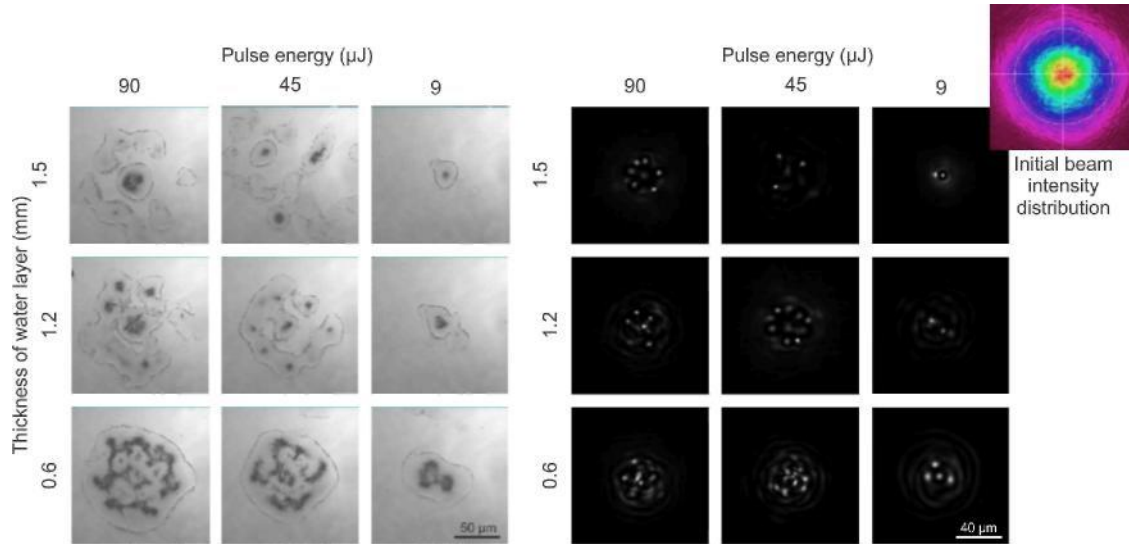
Fig. 5.7 Ablation patterns acquired experimentally (left) and by modelling the modified Schrodinger equation (right) for given different pulse energy settings and water thickness values.

Laser pulse nonlinear transformation takes place because of the optical Kerr effect and multiphoton absorption in water. According to the beam modelling, these processes break up the near-Gaussian spatial transverse intensity distribution into a filament array. The multiple white spots visible in the theoretical results represent the most insensitive areas, the filament cores, whereas the darker spots in the experimental results represent the areas, where the chromium layer was damaged or even removed through the ablation process. The ablation takes place most efficiently in those areas of highest intensity. Inconsistencies that are present may be due to inaccuracies in the water-layer thickness determination, the phase front being not ideally flat (e.g. because of beam aberrations through the focusing optics, even though intensity distribution for the modelling was recorded using a CCD camera, and is shown in Fig. 5.7 (top right corner). To conclude, both experimental and simulated results testify that the beam breaks up into an unsymmetrical matrix of multiple filaments. The number of filaments depends on the instantaneous pulse power

relative to the critical power in water to be more precise, as well as on the water-layer thickness:

$$P_{cr} = \frac{3.77 \cdot \lambda^2}{8 \cdot \pi \cdot n_2} = 3.88 \text{MW},$$
(5.2)

where $\lambda = 1028$ nm is the laser wavelength and $n_2 = 4.1 \cdot 10^{-16}$ cm^2/W is the water nonlinear index of refraction.

The cause of this process is the intrinsic property of laser-matter interactions in the case of high peak power laser beams. The intensity profile of the real laser beam is never ideally smooth but is modulated. In water, these modulations, initially caused by various optical component imperfections, dust, or burned spots, initiate beam break-up into filaments.

The agreement between theoretical and experimental results demonstrates that self-actions should also be important for the cutting or percussion drilling of materials with a thickness larger than 1 mm in water. The modelling also showed that the transversal energy distribution changes rapidly along the axis. In comparison to conventional focusing in the air, in water, the beam has "hot spots" in the

Fig. 5.8 An example of partially controlled filamentation in water through beam distortion. Images represent chromium film ablation patterns made with one pulse exposure through 500 μm water layer when the laser beam was focused by the weak cylindrical lens.

form of filaments. This energy bundles concentrated spatially may accelerate light-matter interactions because of higher EM wave intensity. In addition, by manipulation of initial beam intensity distribution impinging on the water layer, break-up control might be possible as described in [130, 185, 186].

As an example, Fig. 5.8 shows that to some extent it is possible to control the spatial distribution of the filaments when the beam symmetry is destroyed. In this particular experiment, a weak astigmatism was introduced into the beam by passing it through a 0.5-dioptre cylindrical lens before final focusing on the

sample. The result is the break-up of the beam into filaments that are aligned across the line. Even weaker distortion of the central symmetry with a 0.25-dioptre cylindrical lens results in beam break-up into several lines. The controlled beam break-up could have potential applications for multiple-foci fabrication without costly spatial light modulators.

All these experiments visually demonstrate that when high-energy pulses are focused even within a thin water layer, the intensity of the femtosecond pulses is high enough to cause beam self-actions, noticeable even at minor propagation distances (hundreds of μm). These effects dramatically affect the intensity distribution of the beam impinging on the surface of the samples. During the material cutting process, these intensity distributions lead to more efficient ablation of the samples and are different at different depths of cut. As the samples are cut, the thickness of the water layer increases, since the depth of the groove increases, and, in this way, the experiment also shows the possible intensity distributions that can be expected at different depth and pulse energy values.

To conclude, the experiment and modelling confirm that nonlinear beam transformation indeed takes place in the buffer liquid, and filaments are formed at least in the case of a small number of consequent pulses.

5.5 Optimization of water assisted femtosecond ablation micromachining process

For the optimization of the micromachining process, over 200 laser-cutting experiments were conducted by varying four main parameters: scanning speed along the surface of the sample (linked with pulse overlap), focal position relative to the surface of the sample, repetition rate and thickness of the added water layer. The boundaries for speed (10 - 1500 mm/s), repetition rate (33.3 - 200 kHz), water layer thickness (0.6 mm - 1.5 mm) and focus position (1 mm above to 1 mm below the surface of the sample) were either limited by hardware or by the fact of ablation disappearing. The obtained empirical model specified as valid only within the boundaries of these parameters. The

parameters chosen for the study are independent of one another, *i.e.,* one parameter is not a linear or nonlinear combination of the other, and, therefore, the value of one parameter can be changed while keeping other parameter values constant. Several additional experiments varying the laser pulse duration, the fluid origin, water pollution degree and air blow-off rate were also carried out to supplement the investigation. Optimization of the cutting speed is accomplished utilizing IDOE [187-189] techniques.

Table 5.1 Parameters varied.

Parameters	Numeric Values
(S) Scanning speed (mm/s)	10 - 1000
(R) Repetition rate (kHz)	33.3 - 200
(*F*) Focal position (mm)	-1.0 - 1.0
(*T*) Water layer width (mm)	0.3 – 1.2

The water layer was formed by submerging the samples in a reservoir. The goal was to minimize fabrication duration, that is, to retrieve a collection of parameters that would cut through a 1 mm thick sample in the least amount of time. The most reproducible cutting-time measurements were obtained when half of the circle with a diameter of 1 mm were cut at the sample edge, and the cutting time was estimated as the time needed to cut a circle until it separates from the rest of the sample. The thickness of the water layer may change as the experiments progress due to water evaporation. Therefore, an optical *in situ* monitoring system was built to measure the thickness of the water in the real time. The laser parameters were chosen as follows: average laser power — 10 W (this is the maximum average power that could be used with the current setup at all repetition rates), minimal pulse duration (270 fs), fundamental wavelength (1028 nm), focal spot diameter ~20 μm (FWHM) when focused in the air. An optimization process involving multiple independent parameters may require countless experiments to study the dependences fully. In such situation, IDOE techniques can significantly reduce the minimal quantity of required experimental data to see the trends. Experimental design is known as *full factorial,* [187] was used, requiring only 81 experimental tests (three

experimental points for each parameter which represent the minimal, mid and maximal values) to obtain the rough empirical model for four independent parameters and understand main dependencies. The initial range of values of each parameter and their meaning are displayed in Table 5.1. After all, experiments had been completed; a polynomial model (first and second order terms along with interaction terms) was fitted to the results.

Optimization of a multiparametric process involves working with multidimensional space. Therefore, the parameter relations to the response (the outcome of the experiment that is measured) cannot easily be graphically displayed. Hence, to obtain the true dependencies of the response based on the values of the parameters, *statistical analysis* must be employed. For that purpose, JMP software was used [190]. The empirical model is obtained by fitting a polynomial expression to the experimental results. Such a procedure is standard in IDOE methods [187]. The preliminary expression in particular was:

$$
\begin{aligned}
\textit{Fabrication duration}(S,R,F,T) = {} & a_0 + b_1{\cdot}S + {\cdot}b_2{\cdot}R + b_3{\cdot}R + b_4 + b_5{\cdot}S{\times}R + \\
& b_6{\cdot}S{\times}R + b_7{\cdot}S{\times}F + b_8{\cdot}T{\times}R + b_9{\cdot}T{\times}F + b_{10}{\cdot}R{\times}F + b_{11}{\cdot}R{\times}T{\times}F + \\
& b_{12}{\cdot}S{\times}R{\times}T + b_{13}{\cdot}S{\times}T{\times}F + b_{14}{\cdot}S{\times}R{\times}F + b_{15}{\cdot}S{\times}T{\times}R + b_{16}{\cdot}S^2 + b_{17}{\cdot}T^2 + \\
& b_{18}{\cdot}R^2 + b_{19}{\cdot}F^2 + \epsilon_0
\end{aligned}
\tag{5.3}
$$

Here, coefficients b_{1-19} represent the impact of each term on the results, a_0 is the intercept and ϵ_0 represents the residuals (variation in the results that cannot be explained by the empirical model), S - scanning speed, R - repetition rate, F - focal position, T - water layer width. The goal of statistical analysis is finding the fit with the simplest expression, which minimizes the residuals and keeps other coefficients with as little variation as possible. Naturally, all terms may not be present given the specific nature of the process (e.g, the interaction $S \times R$ may not exist). Therefore, terms which are deemed statistically insignificant are dropped from the model, thus obtaining an simpler model with fewer terms.

After conducting the experimental tests, large variations in the results were noticed depending on different parameter settings, e.g, when fabricating with $R = 33$ kHz, $F = 0$ mm, $T = 0.3$ mm, $S = 800$ mm/s, the duration required

to cut a 1 mm Ø circle from 1 mm thick steel plate was 16 s, whereas, when fabricating with $R = 200$ kHz, $F = 1$ mm, $T = 0.6$ mm, $S = 10$ mm/s, fabrication took more than 15 minutes. There was also a parameter combination that could not end up with final separation of the cut material. Therefore, the responses differ by several orders in magnitude, depending on the parameter values chosen.

When differences of several orders are present, fitting polynomial models to the results may become difficult as the true functional expression may typically end up with high-order terms (the polynomial expression described by equation (6.3) may no longer suffice), hence the number of coefficients may become large, and overall understanding of the underlying physics may become difficult and misleading. Therefore, to refine the areas with optimal parameters, it was decided to narrow down the region, where the polynomial model need not require high-order terms by choosing response values no higher than 120 s (all the parameter values producing fabrication times longer than 120 s were dropped). The final parameter range (with the dropped points) described by the polynomial model is listed in Table 5.2. The polynomial model was fit, and corresponding statistical parameters are displayed in Fig. 5.9.

Table 5.2 Final parameter optimization range.

Parameters	Parameter range
(S) Scanning speed (mm/s)	100 - 1000
(R) Repetition rate (kHz)	33.3 – 108.3
(F) Focal position (mm)	-1.0 - 1.0
(T) Water layer width (mm)	0.3 – 0.6

The sum of all products of terms with their corresponding coefficients and intercept (see Fig. 5.9) gives the final empirical expression that relates fabrication duration and the four parameters:

Fabrication duration [s] = $(2.8 - 0.0029 \cdot S + 0.0000061 \cdot S_n^2 - 0.073 \cdot F + 1.1 \cdot F_n^2 + 0.013 \cdot R + 0.000033 \cdot R_n^2 + 6.6 \cdot T + 0.0000098 \cdot S_n \cdot F_n - 0.0000019 \cdot S_n \cdot R_n + 0.0032 \cdot F_n \cdot R_n - 0.000017 \cdot S_n \cdot F_n \cdot R_n - 0.0024 \cdot S_n \cdot T_n)^2$, (5.4)

where $S_n = S - 532.5$; $F_n = F + 0.018$; $R_n = R - 85.85$; $T_n = T - 0.39$ are normalized parameters. With such prediction expression, one can estimate not only the optimal conditions for fabrication but also estimate the most influencing parameters as well as deviations in the results if the parameters themselves pose statistical uncertainty. For example, one can estimate the decrease in the rate of fabrication if the sample-positioning plane is tilted (change in focal position throughout the sample).
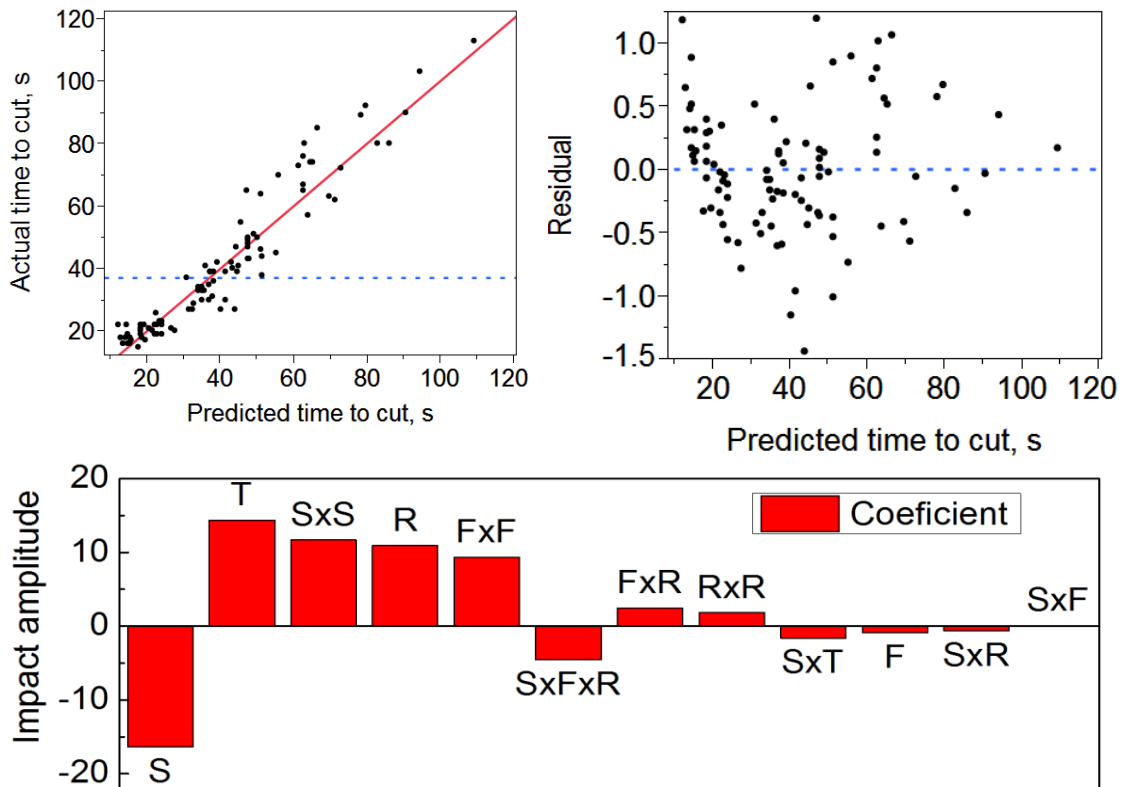
Fig. 5.9 Fit statistics. Measured points relative to model-calculated points are displayed in the top left corner. Deviations (residuals) of the actual points from the calculated points are displayed in the top right corner. Coefficient data and their impact on the results are displayed in the bottom part. Fit $R^2 = 0.92$, RMSE = 0.5 s, $a_0 = 58$.

The top left graph in Fig. 5.9 displays how well the actually measured points coincide with points predicted by the model; if the model ideally explains the results, then the points should be situated along the diagonal. The graph in the top right corner shows the deviation of the predicted values from the measured values; since experimental errors are present in real experiments, these points should be scattered following a normal distribution. In this case,

the predicted points coincide with the measured points, and the residuals appear to be scattered normally, meaning that the prediction precision is homogeneous throughout the entire response range. The root mean square error (RMSE) value (RMS of residual variation) was calculated as equal to 0.92 s; since the pure error (experimental error calculated by conducting experiment replicates) is equal to 1.87 s, it can be concluded that the model fits the measured results sufficiently well, and further increase in accuracy is unnecessary. The terms used to construct the model are listed in the bottom part of Fig. 5.9. The impact of each term was normalized to unity, and the bar chart describes the impact of each term on the results, e.g. the term *F* x *F* produces approximately twice the variation in the results relative to term *S x F x R*. The positive and negative impacts represent how the results change if the parameter values are increased or decreased, e.g., an increase in repetition rate and thickness of the water layer will entail longer fabrication duration and decrease the fabrication speed.

The acquired dependence is complex and several parameter interactions are present *(S x S, F x F, S x F x R, F x R, R x R, S x T, S x R, S x F)* and influence the experiment outcome; therefore, the result-parameter space is curved and bent in many dimensions. This presents the complexity of representing the dependencies graphically, due to the restriction of seeing only a part of the dependence. In reality, the terms represent hidden physical mechanisms that influence such experimental outcomes. After the empirical model is obtained, the relationships between the results and the embedded parameters (pulse overlap, intensity, fluence, *etc.)* can be calculated. To avoid ambiguity, a comment should be added here on the repetition rate. The repetition rate is reciprocal to laser pulse energy, and, when the average laser power is kept constant, a change in repetition rate results in a change in pulse energy. In addition, when the scanning speed is kept constant, a change in the repetition rate results in a different pulse overlap, which could potentially affect experimental outcomes.
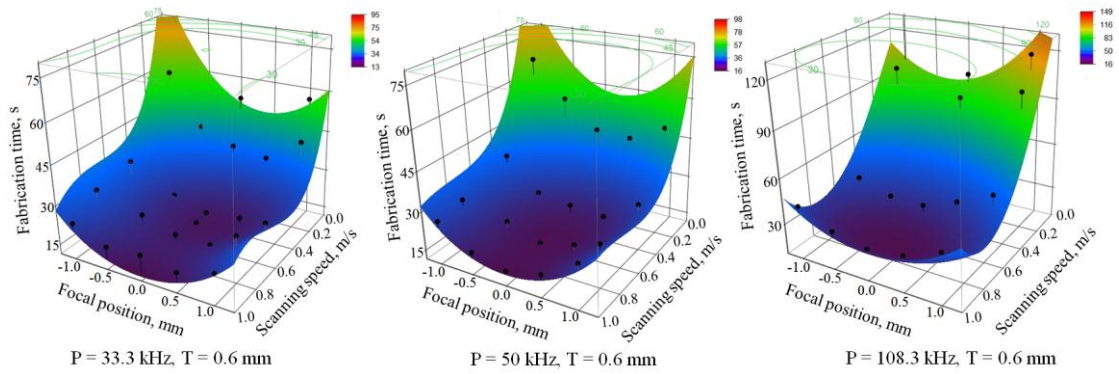
Fig. 5.10 Fabrication duration *vs.* focal position and beam scanning speed graphs for cutting 1 mm diameter circle from 1 mm thick steel sheet at different repetition rate settings when 600 μm water layer is used. The black dots are the actually measured points, whereas the surface is produced via the prediction expression.

As was demonstrated earlier, the interaction of the beam with the water layer is governed by nonlinear interaction mechanisms, therefore beam break-up, the resulting fluence, and energy propagation directions are influenced mostly by the beam front curvature (which relates to focal position) that impinges on the water layer, the energy of the pulse (reciprocal to pulse repetition rate) and the distance the beam propagated through nonlinear media (thickness of water layer). Consequently, the appearance of interaction terms is not surprising. The energy of the pulses and the thickness of the water layer dramatically influence how the energy distributes over the surface of the sample and how the propagation path of the beam changes. Furthermore, the water layer changes significantly, when fabrication with different parameter settings is carried out, as was shown by the shadowgraphy experiments [181]. Not surprisingly, repetition rate, as a parameter, is one of the most important parameters that influence fabrication duration. The increase in pulse energy, when the repetition rate decreases (as the power is held constant) most likely contributes to shorter fabrication duration since self-actions are more pronounced at higher pulse energies, and effects such as varying pulse overlap from the changing repetition rate may be neglected.

Several fabrication duration graphs *vs.* two other arbitrarily chosen parameters are displayed in Fig. 5.10. The surface represents the model with

140

fixed value of water layer thickness (600 μm). Stars with needles represent the experimentally measured points and their residuals. It should be noted, that because of the visualising difficulties with statistical analysis software (JMP [190]), the points that are below the fit surface (points with negative residuals) are not visible. It can be seen that, as the remaining two parameters are varied, the surface bends though the experimentally measured points but does not drift away, which confirms the validity of the empirical model obtained.
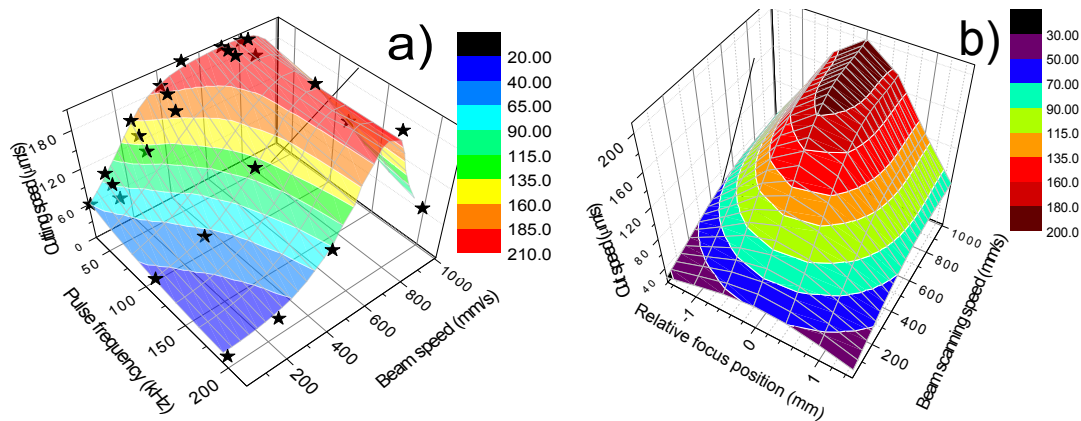
Fig. 5.11 The dependence on the cut speed for 1 mm steel with 10 W average laser power under 500 μm water layer on various parameters: a) on the pulse frequency and beam scanning speed (focus position at optimal position of -0.2 mm), b) on beam speed and focus position (pulse frequency at 60 kHz). Dots are experiment values, surface – best fit of the model.

Fig. 5.11 represents the dependencies in more convenient "average cut speed" terms. As is evident from these graphs, cutting speeds up to 0.2 mm/s are achieved on stainless steel samples of 1 mm thick. Best results in terms of cutting speed of steel are obtained when maximal pulse energy and power of the laser are used at the same time. For laser in the current setup, this was 300 μJ, 10 W at 33 kHz. The beam scanning speed is set to close to 750 mm/s, the minimal sustainable water layer thickness of ~300-500 μm (which was found to be different for different materials, probably because of different surface wetting properties) is used, and the laser beam has focused some hundreds of μm below water layer surface.

Several images of cut samples using the optimal fabrication parameters are displayed in Fig. 5.12 a) and b) presents the same 1 mm thick stainless steel sample cut under water film and in the air. e) and f) present cuts accomplished in the one euro-coin. g) presents cut entrance (straight cur) and exit (curved cut) on the same image. As is evident, cutting macro and micro components is possible using this setup.
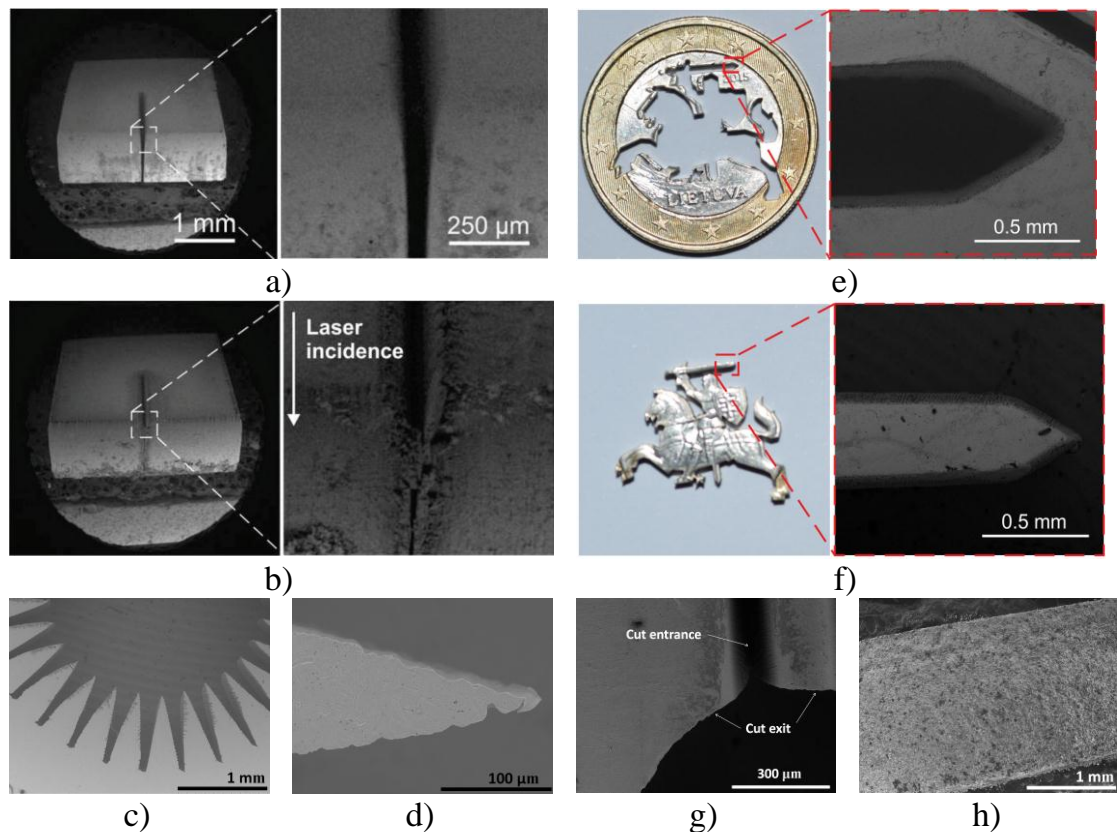
Fig. 5.12 Examples of complex structures cuts and wall surface quality micromachined using water assisted ablation showing cut morphology and quality in 1 mm thick stainless steel a–d, g); > 2 mm thick copper-nickel, nickel, copper-nickel "sandwich" e–f); neodymium magnet h). Optimal fabrication parameters that were used: average power - 10 W, T = 0.5 - 0.6 mm, R = 33.3 kHz, F = -0.5 mm, S = 300 mm/s. b) is for comparison, displays the cut of stainless steel sample in the air.

Furthermore, not only steel but many other alloys and different materials can be cut with this technique. For metals, the possible thickness for through-cutting reaches 2 mm as is evident from Fig. 5.12, where a one-euro coin was micromachined. It is worth mentioning that similar results can be acquired using non-optimal parameters. However, the cutting rate may differ by a few orders of magnitude depending on the settings in the experimental domain

presented. Fig. 5.13 shows the SEM micrographs of some hard materials microfabricated with this technique. In the case of metals, samples cut in the air possess visibly melted regions, HAZ and redeposition of debris on nearby surfaces (as evident in Fig. 5.13). Furthermore, the rate of fabrication in the air decreases by a factor of seven compared to cutting in water.

a)   b)   c)
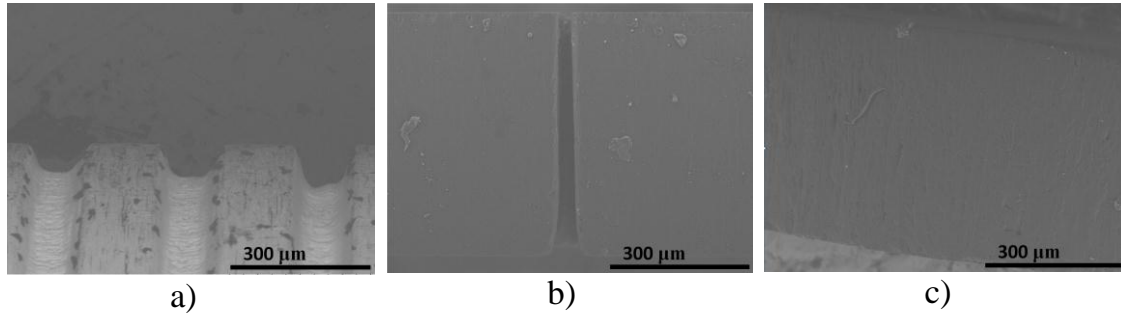
Fig. 5.13 a) Tungsten tube (groove made on the cylinder surface), b) silicon carbide (side view of through cut) and c) artificial diamond (top view of the cut piece) microfabricated in water with fs ablation.

5.6   Influence of the laser pulse duration on the cutting speed of steel

There are ongoing scientific debates between the fs and ps-laser "followers" as regards which lasers are better suited for micromachining [47]. The following study focuses on the dependence on pulse duration (*t*) of the laser cutting speed for steel immersed in water. The duration was changed using a laser built-in pulse compressor by varying the distance between the compressor gratings. As the Pharos laser utilizes widely used chirped pulse amplification techniques [191] to amplify the weak stretched in time femtosecond pulses from the oscillator, it was possible to get amplified but chirped in time radiation. Beyond the pulse duration (*t*) (250 fs – 20 ps), other experimental parameters such as beam scanning speed (*v*) (10 – 1000 mm/s) and sample position relative to the focus position (*f*) (-1 - 1 mm) were also varied. The other parameters were kept as follows: laser average power 10 W, pulse repetition rate – 33 kHz, water layer thickness – 300 μm. The beam was focused with the same 100 mm F-theta lens as in the previous experiments. A piece of a circle

(1 mm diameter) was micromachined until it separated from the sample for each parameter set. The cutting time was measured.

All the experiments were analysed and fitted using the statistical full factorial model with extra added beam speed points. Parameter interaction terms (v^2, f^2, $v{\cdot}f{\cdot}t$, t^2, $v{\cdot}t$, $f{\cdot}t$, $v{\cdot}t$) were used in the model (the exact functional expression is provided in Appendix 1). The model predicted all the results with an RMS error better than 0.03 s, which exceeds time measurement precision. Overall, 80 cutting experiments with through-cutting times from 16 to 300 s were carried out and jointly analysed.
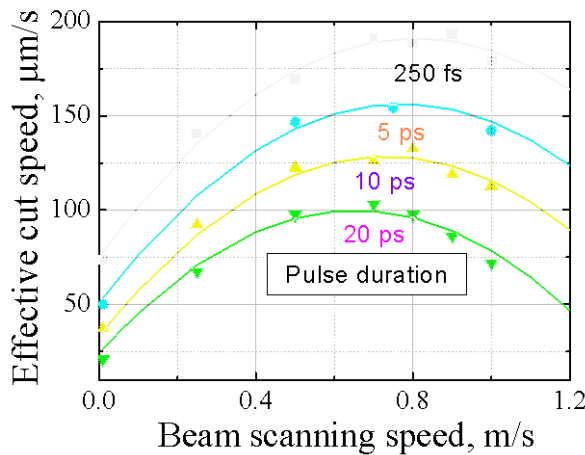
Fig. 5.14 Cutting speed dependence on pulse duration and beam scanning speed when other parameters (average laser power 10 W, wavelength 1028 nm, water layer thickness 500 µm, relative focus position at 0 mm) are kept constant.

The best fit model showed that the optimal parameters for steel cutting would be as follows: beam travel speed - 788 m/s, beam focus position 170 µm below the water surface with the shortest available pulse duration (250 fs). With these parameters, one will achieve 190 µm/s effective cutting speed through 1 mm steel sheet. The investigation showed that the effective cutting speed of steel decreases with increasing laser pulse duration. Similar dependencies in terms of laser pulse duration are presented in recent conference contribution for the micromachining of steel in the air [93]. The most influential parameters are the beam speed, pulse duration and their interaction terms. The least important is the focus position. Consequently, the optimal focus position does not change with variations in the pulse duration or beam speed. However, as is evident from Fig. 5.14, the optimal beam scanning speed decreases slightly when the pulse is stretched. The results show that,

144

with the filamented-beam ablation technique, it takes almost twice as long to cut through a 1 mm steel sheet when switched from 250 fs to stretched 20 ps-laser pulses. This indicates the nonlinear nature of the light-matter interaction.

5.7   Cutting throughput comparison for metallic materials

Cutting speed results for metallic as well as other materials are displayed in Fig. 5.15. All the materials were cut using optimal parameter values for 1 mm thick steel, which might not be optimal for other materials and material thicknesses. However, as one can note from Fig. 5.15, given the same material type, the results roughly follow a linear dependence when displayed on a logarithmic scale.
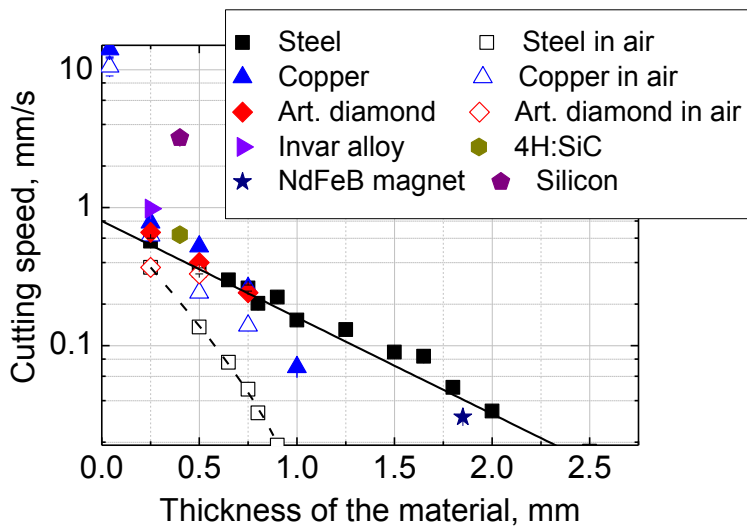
Fig. 5.15 Cutting throughput results for different materials and material thicknesses.

Overall, metals display lower cutting rates (0.15 mm/s for 1 mm thick steel, 0.07 mm/s 1 mm thick copper) compared to transparent materials (0.31 mm/s for 1 mm soda-lime glass). This may be due to the higher metal reflectivity and the evaporation temperature of metals as compared to transparent materials. $0.25 - 2$ mm thick steel cutting with this technique can be summarized by the following expression: $v(\text{mm/s}) = 4 \cdot 5^{-1-d(\text{mm})}$, where d is the steel thickness. This expression is represented by the solid black line on the Fig. 5.15. It is clearly visual that the steel cut in the air (dash line) is below the solid line, thus the cut speeds in the air are considerably lower. Crystalline

silicon wafer is being cut approximately 10 times faster (3.4 mm/s for 0.4 mm thickness) under water than in the air.

The most impressive advantages of these micromachining techniques were revealed when a piece of nontransparent black plastic (2.8 mm thick) was cut (not shown on the graph). A cutting speed of almost 10 mm/s was achieved with no signs of burning or any thermal damage. For this material, it is impossible to compare the results with ablation in the air because at this laser power any set of process parameters (beam scanning speed, frequency, focus position) resulted in the almost instantaneous burning of the plastic. This example implies that water-assisted fs micromachining heats and evaporates material very locally indeed, and helps to remove thermal influence completely.

When ablating in the air, cutting through samples with a thickness greater than 1 mm were impossible due to reclogging of the cut channel by ablation debris. Deep trenches and high aspect ratio grooves are difficult to machine in the air, mostly due to obstruction of the plasma plume expansion in the sample and accordingly of material removal, which then tends to stick to the sidewalls. However, this is not the case when liquid is present. Depending on the laser parameters, irradiated liquids can experience the formation of an intense shock wave [179], vapour expansion, cavitation [192] and breakdown. All these phenomena result in disturbance of the incident beam, increased laser power losses and scattering of the laser beam. However, despite them, the effective cutting speed of the thick material samples is increased. For all the materials, the cutting speeds are higher when cutting under water. Using the same experimental setup without the water layer, yields cutting throughput results that are lower from 200 % (0.75 mm copper) to 780 % (0.75 mm steel) for metals, and by 750 % for semiconductors (0.4 mm silicon).

The dimensions of the cuts made in all of the above-stated materials were approximately 70-100 μm at the entrance and approximately 35-50 μm at the exit. This yields the tapper angle values approximately better than to 2° for

1 mm thick materials. Wider (closer to 100 µm) cuts are obtained in materials having better absorptivity (metals). The peak-to-valley roughness of the cuts for all of the samples presented was approximately 5 µm.

5.8   Cutting of copper foil under water

The ability to fabricate clean cuts without any additional post treatment is a great advantage, with potential applications in shadow mask production for OLED devices, and the automobile industry [193]. Therefore cutting under water possesses unique advantages. Several attempts of foil cutting were accomplished with copper (of 40 µm thickness) and invar (250 µm thick) foils. The experiments were carried out under the filamentation regime in a thin layer of water as well as in ambient air for the purpose of comparison. In both cases, the laser parameters were the same: pulse duration – 250 fs, average beam power – 5 W, pulse repetition frequency – 25 kHz. A loose focusing condition (100 mm focal length F-theta lens) was used in both cases. The sample position relative to the beam focal position and the beam scanning speed were the variable parameters. The time to cut through a 7 mm-long line, as well as the quality of the cut, were the objects of study and optimization.

After analysing the outcome of many experiments, it was concluded that, in terms of the cutting speed, there is only a minor process speed up when filament-assisted ablation is used in comparison with ablation in the air. Fig. 5.16 shows the effective cutting speed dependence on the beam scanning speed and focus position with respect to the sample surface. There is no gain in the cutting speed of the foil. However, it is clear that broader parameter range in the case of underwater micromachining leads to similar results in terms of effective cutting speed. This means that one will have wider "parameter working window". Furthermore, water layer helps to clean the nearby surfaces from the ablation debris by generating a pressure wave, spreading from the ablated area with a speed exceeding 6000 km/hour (at least in the air) [179]. This improves the cut quality. Fig. 5.17 shows the SEM micrographs of the microcuts made in copper using both approaches. The film ablated in the air

(upper-row images) is heavily polluted with ablation debris. The contaminated areas extend up to 200 μm from the cut edge. Heat-affected areas of the material, up to 50 μm wide from each side of the cut, can also be identified. These are the areas, where ripples are formed. A lithographic mask made with such cuts would definitely require post-treatment for cleaning. On the other hand, the film micromachined using a filamented beam (images in the bottom row of Fig. 5.17) and water assistance is clean from ablation process waste and shows diminished areas with ripples that is no heat affected areas. Similar results are obtained for thick materials cut with this technique.
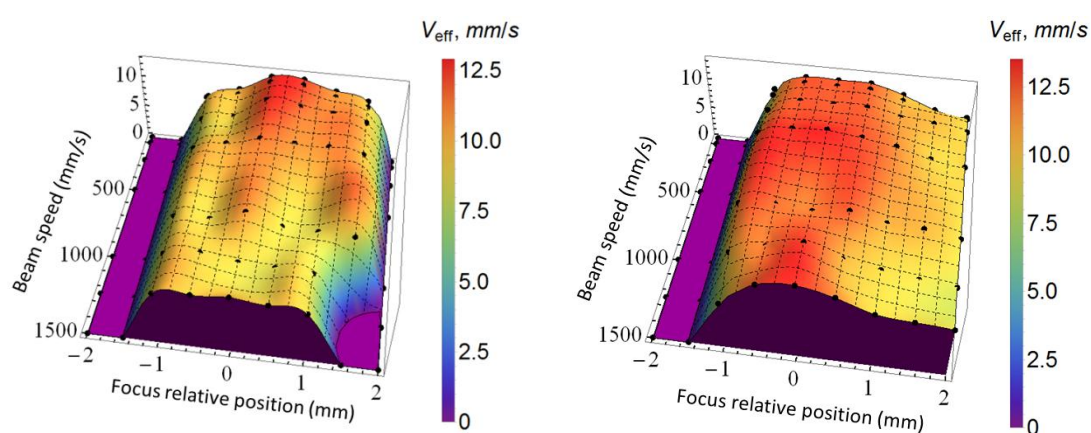
Fig. 5.16 Effective cutting speed dependence on the beam scanning speed (0 – 1500 mm/s) and the sample surface position relative to focus (-2 - +2 mm) when the copper foil is micromachined using femtosecond laser ablation in the air (left) and filament-assisted ablation (right).

By this method, it is possible to improve the surface quality of the sidewalls, increase the maximal depth and machining performance of high-aspect ratio grooves, which have the width close to the characteristic plasma plume size. Some side effects that should be mentioned are reduced sticking of the ablation particles to the sample surface and greatly diminished air pollution from nanoparticle dust, as they all remain in the water. However, the method involves an additional technological challenge of supplying and maintaining in a precise manner the required amount of liquid at the processing point.
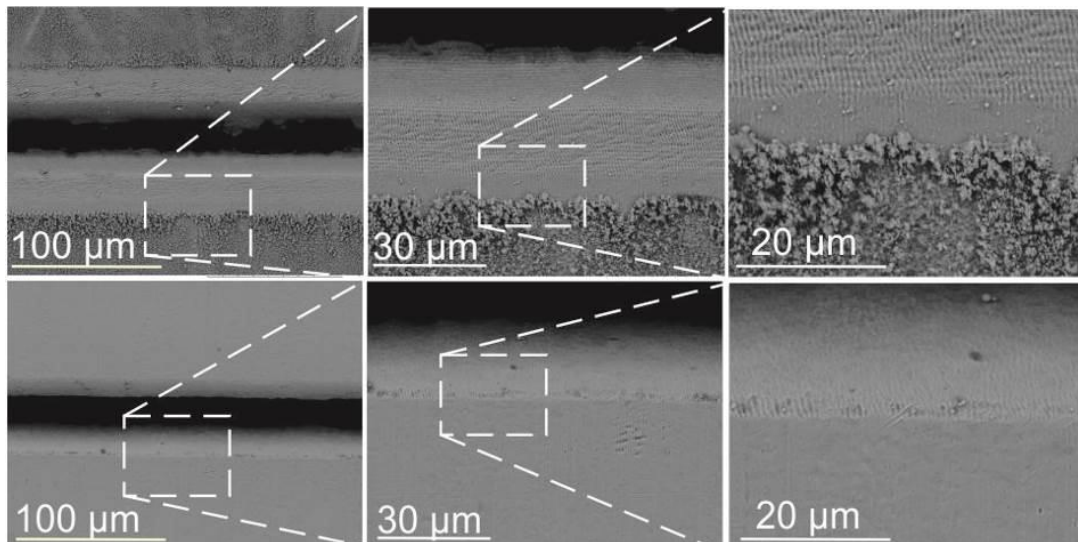
Fig. 5.17 SEM micrographs of copper foil microcuts accomplished by fs-laser ablation in the air (upper row) and filament-assisted ablation in water (lower row).

5.9 Energy-dispersive X-ray spectroscopy on steel samples

EDS was used for the elemental analysis of steel samples treated with the fs-laser. The investigation showed that elemental composition was not affected by the laser treatment, as has also been found in other studies [194]. Cut areas of the steel samples were examined with the "SU70" SEM and "TM-3000", which have an EDS extension from Hitachi Oxford Instruments. All measurements were carried out with 15 kV accelerating voltage. Though no new elements were found in the laser-treated area, but the existing element concentration was changed from that of the original surface. This study focused on these elements: Fe, Cr, Mo, C, Mn, Cu, Al, S, Cl, Na and O. High-energy photon spectra were obtained by EDS analysis of steel for three different cases: the original laser untreated surface; the centre of the cut area of the sample when the cut was performed in the air; and the middle of the cut area of the sample when the cut was performed under a thin water layer. The laser parameters for both cases of laser treatment were the same. Table 5.3 explicitly presents the atomic composition of all these cases acquired through the EDS analysis.

149

From SEM and EDS of high-energy photon analysis, a substantial increase in the oxygen atomic percentage was observed, when the steel specimen was cut in the air. The iron percentage in the sample is a good base point for analysing the other elements, as it should remain unchanged by the laser treatment or possible contamination of the surface. The ratio of iron to oxygen (Fe/O) for the three cases studied is 4.87, 0.82 and 4.7. There are much more oxygen atoms in the cut area when the cutting is accomplished in the air. The EDS techniques rely on the interaction of accelerated charged particles with matter. Although the penetration depth for excitation particles differs with material density, conductivity, porosity, etc, the emitted electrons are absorbed within the 200 – 1000 nm skin layer of the material. Therefore, EDS reveals the surface element composition. Water efficiently cools the sample by dissipating the heat produced during laser micromachining. Therefore peak surface temperature, as well as the thermalisation rate in water, must be accordingly lower and greater. On the other hand, water or water vapour, produced during under-water ablation, isolate the ablation area from the oxygen in the air. This all diminishes the oxidation processes that occur in the case of micromachining in the air [195]. Therefore, in the case of steel laser micromachining, it is more advantageous to use filamented ablation under water when oxidation should be avoided.

Table 5.3 Chemical composition (atomic %) of the original surface and area near the laser cut in a steel sample.

	Carbon	Oxygen	Aluminium	Silicon	Sulfur	Chromium	Manganese	Iron
Original surface	22.56	**11.19**	0.91	0.72	-	9.40	0.24	54.52
Cut in the air	21.25	**38.86**	1.12	0.40	0.23	5.77	0.28	32.08
Cut in water	30.32	**9.88**	1.37	0.32	0.29	8.45	0.36	46.54

Similar results concerning oxygen concentration were obtained in the case of copper film. The Cu/O ratio of the three compared cases was accordingly: 13 -17 for the untreated surface, 10 - 17 for the underwater cut

and 2.7 - 4.6 for the in-air cut. This indicates that the cut area of the copper film is also more heavily oxidized when the cutting is performed in the air rather than under water.

5.10 Significant results and conclusions

A novel technique of filament-assisted direct laser machining by ablation unites nonlinear beam transformation, effective cut area cleaning, sample cooling and robust ablation in one process, as well as helping to improve such important laser micromachining process factors as (i) cutting speed, (ii) material removal obstruction in greater depths, (iii) diminishing the heat-affected zone. The influence of the water layer on the femtosecond ablation yield and quality of metallic samples can be summarized as follows:

1. Filament-assisted ablation helps to increase the cutting speed by up to 10 times compared with the conventional ablation in the air for some thick materials and greatly extends the depth saturation limit. In addition, better results in terms of quality are demonstrated.

2. A thin water layer on top of the sample reduces ablation-process contamination of nearby surfaces (material debris) and the dimensions of the heat-affected zone.

3. Chromium thin-film ablation patterns signify that a thin (0.3-1 mm) water layer above the sample transforms a femtosecond beam, with power exceeding >50 times the critical power for self-focusing, into multiple filaments at least in the case of single pulses.

4. The comparison carried out with EDS of the surface element composition of steel and copper cut areas in the case of femtosecond micromachining in the air and water revealed 5.7 times higher oxygen ratios in samples cut in the air, indicating the formation of an oxidized material layer that is absent on the samples cut in water.

5. A laser-cutting parameter optimization for 1 mm thick bulk steel ended up with a maximum 0.2 mm/s cutting speed, with the following laser, scanner, and focusing parameters: highest pulse energy (300 μJ at 10 W average

laser power and 33 kHz pulse repetition rate); shortest pulse duration (270 fs); minimal (~300 μm) water buffer layer; focusing 200 μm above the sample surface (for 100 mm F-theta objective); 500 – 800 mm/s scanning speed range. Data statistical analysis revealed that pulse energy and beam scanning speed are the factors that mostly affect the cut speed.

6. List of main results and conclusions

1. Using 2D positioning system based on linear direct-drive servomotors stages and high repetition rate femtosecond laser, 200x200x5000 μm grooves in mould steel and aluminium were fabricated with the required 5 % accuracy and better than 84° wall inclination angle and the whole process took 15 minutes. Using galvoscanner for beam positioning the same grooves even with better quality on plane samples were fabricated during 1 minute.

2. The structures manufactured with the bidirectional spiral algorithm (among other algorithms such as raster scan, line scan with loose focusing, circle-spiral scan, conventional hatch, and others) exhibit the steepest walls and minimal bottom waviness in both systems developed. The grooves formed are symmetric and regular. With a 5 W, 270 fs-laser system, a pulse repetition rate of 50 kHz, using this algorithm and a programmed width of 250 μm, the deepest fabricated groove had a depth reaching 900 μm.

3. Comparison of fabrication procedures showed that the highest ablation efficiency of the mould steel is mainly dependent on the average power of the femtosecond pulses, independently of the wavelength for 1028 nm and 343 nm pulses, and, in comparison with a Gaussian beam, the hat-top structure of the beam has no positive influence in comparison with a Gaussian beam for the fabrication of grooves with a depth larger than 30 μm. The Gaussian beam produces higher quality grooves and do not deteriorates groove edges and nearby surface.

4. A developed ultrashort pulse laser micromachining system was successfully applied for titanium suboxide ceramic microfabrication tasks including cutting samples up to 1 mm thick, microhole percussion drilling and micronotch fabrication. The fabrication of notches in titanium suboxide ceramic fibres for electrical contact attachment is a more straightforward, simpler and faster process in comparison with the hole percussion drilling

because of the lower sample positioning accuracy and focusing tightness requirements

5. The specific resistances of the ceramic fibres processed with a femtosecond laser with aluminium based contacts and silver wires fixed in machined microtrenches and microholes were in the range of 21 – 35 mΩ·cm; that coincides well with the unprocessed conductivity of the fibres and leads to the conclusion that delicate femtosecond laser machining (repetition rate < 60 kHz, energy fluence < 11 J/cm^2) does not significantly influence this electrical property of the material.

6. A filamented-beam ablation technique was adopted for absorbing solid-state materials, which considerably broadened the applicability of femtosecond micromachining, raised the cutting speeds and quality of the process. Filament-assisted ablation helps to increase the cutting speed of thick materials (0.5 – 2.5 mm) up to seven times compared with conventional ablation in the air for steel, copper, conductive ceramics and other absorbing materials. In addition, better results in terms of quality are demonstrated.

7. Experiments with chromium thin-film ablation demonstrate that a thin (0.3 - 1 mm) water layer above the sample transforms a femtosecond beam, whose power exceeds >50 times the critical power for self-focusing, into multiple filaments at least in the case of single pulse or a small number (<5) of pulses.

8. A comparison of the surface element composition of steel and copper cut areas in the case of femtosecond micromachining in the air and water performed with EDS revealed 5.7x times higher oxygen ratios in the samples cut in the air. This indicates the formation of an oxidized material layer that is absent on the samples cut in water.

9. Optimal parameters for ablation cutting of the stainless steel in water are: the shortest available pulses from the laser used - 270 fs, the largest average power at smallest repetition rate - 10 W at 33 kHz, water buffer layer in

range from 300 μm to 600 μm, beam focusing position 200 μm above the sample surface for 100 mm F-theta lens and scanning velocity in the range of 500 – 800 mm/s. With that parameters 0.2 mm/s effective cutting speed for 1 mm thick stainless steel is achieved.

7. Bibliography

[1] U.S.G. Survey, Mineral commodity summaries 2014, U.S. Geological Survey, 196 (2014).

[2] D.M. Allen, T. Talib, D. Horne, Surface textures and process characteristics of the electrolytic photoetching of annealed AISI 304 stainless steel in hydrochloric acid, Precis. Eng., **5** 51-56 (1983).

[3] F. Shieu, L. Cheng, M. Shiao, S. Lin, Effects of Ti interlayer on the microstructure of ion-plated TiN coatings on AISI 304 stainless steel, Thin Sol. Films, **311** 138-145 (1997).

[4] M. Knowles, G. Rutterford, D. Karnakis, A. Ferguson, Micro-machining of metals, ceramics and polymers using nanosecond lasers, Int. J. of Adv. Man. Techn., **33** 95-102 (2007).

[5] L. Cerami, E. Mazur, S. Nolte, C. Schaffer, *Femtosecond Laser Micromachining*, in: R. Thomson, C. Leburn, D. Reid (Eds.) *Ultrafast Nonlinear Optics* (Springer Intern. Publ., 2013).

[6] R.E. Smallman, R.J. Bishop, *Modern physical metallurgy and materials engineering* (Butterworth-Heinemann, 1999).

[7] M.J. Weber, *Handbook of optical materials* (CRC press, 2002).

[8] F. Wooten, *Optical properties of solids* (Academic press, 2013).

[9] O. Balachninaitė, A. Bargelis, A. Dementjev, R. Jonušas, G. Račiukaitis, V. Sirutkaitis, *Lazerinė technologija* (VU leidykla, 2008).

[10] D.R. Lide, *CRC handbook of chemistry and physics* (CRC press, 2004).

[11] P. Campbell, Enhancement of light absorption from randomizing and geometric textures, JOSA B, **10** 2410-2415 (1993).

[12] M.S. Brown, C.B. Arnold, *Fundamentals of laser-material interaction and application to multiscale surface modification*, in: *Laser precision microfabrication* (Springer, 2010).

[13] S. Wilson, M. Hutley, The optical properties of'moth eye'antireflection surfaces, J. Mod. Opt., **29** 993-1009 (1982).

[14] W. Zhou, M. Tao, L. Chen, H. Yang, Microstructured surface design for omnidirectional antireflection coatings on solar cells, J. Appl. Phys., **102** 103105 (2007).

[15] S.A. Boden, D.M. Bagnall, Tunable reflection minima of nanostructured antireflective surfaces, Appl. Phys. Lett., **93** 133108 (2008).

[16] J. Mueggler, Z. Kancleris, A. Galdikas, M. Yadav, H. Khiroya, A. Melninkaitis, V. Sirutkaitis, D. Paipulas, A. Alesenkov, O. Balachninaite, A.C.E. Dent, D. Reginonini, V. Adamaki, *Sensor system for monitoring wear*, in: S.D. F.A. Muggier Service A/S (Ed.), 2013).

[17] Community research and development information service database. MesMesh project. Online access: http://cordis.europa.eu/result/rcn/57034_en.html (last accessed 2015.09.20).

[18] Project "MesMesh" (Ultra - thin conductive ceramic mesh to monitor stress and wear on a steel surface) funded by the European Commission under the FP7 Cooperation Program. Online access: http://www.mesmesh.eu (last accessed 2015.09.20).

[19] C.B. Carter, M.G. Norton, *Ceramic materials: science and engineering* (Springer Science & Business Media, 2007).

[20] A.J. Moulson, J.M. Herbert, *Electroceramics: materials, properties, applications* (John Wiley & Sons, 2003).

[21] R.C. Buchanan, *Ceramic materials for electronics* (CRC press, 2004).

[22] A. Gusev, E. Avvakumov, A. Medvedev, A. Masliy, Ceramic electrodes based on Magneli phases of titanium oxides, Science of Sintering, **39** 51-57 (2007).

[23] Y. Wang, F. Li, B. Yan, T. Fan, M. Xu, H. Gong, Kinetic study on preparation of substoichiometric titanium oxide via carbothermal process, J. Therm. Anal. Calorim., 1-10 (2015).

[24] J. Smith, F. Walsh, R. Clarke, Electrodes based on Magnéli phase titanium oxides: the properties and applications of Ebonex® materials, J. Appl. Electrochem., **28** 1021-1033 (1998).

[25] M. Ivanovskaya, V. Romanovskaya, G. Branitsky, Composite materials based on Ti and Ru oxides, J. Mater. Chem., **4** 373-377 (1994).

[26] Ebonex company. Online access: http://www.ebonex.co.uk/products/ (last accessed 2015.09.20).

[27] B. Young, B. Wilson, D. Price, R. Stewart, Measurement of X-ray emission and thermal transport in near-solid-density plasmas heated by 130 fs laser pulses, Physical Review E, **58** 4929 (1998).

[28] S. Eliezer, *The interaction of high-power lasers with plasmas* (CRC Press, 2002).

[29] X. Wang, D.M. Riffe, Y.-S. Lee, M. Downer, Time-resolved electron-temperature measurement in a highly excited gold target using femtosecond thermionic emission, Physical Review B, **50** 8016 (1994).

[30] W. Farm, R. Storz, H. Tom, J. Bokor, Direct measurement of nonequilibrium electron-energy distributions in sub-picosecond laser-heated gold films, Surf. Sci., **283** 221-225 (1993).

[31] M. Bonn, D.N. Denzler, S. Funk, M. Wolf, S.-S. Wellershoff, J. Hohlfeld, Ultrafast electron dynamics at metal surfaces: Competition between electron-phonon coupling and hot-electron transport, Physical Review B, **61** 1101 (2000).

[32] B. Chichkov, C. Momma, S. Nolte, F. Von Alvensleben, A. Tünnermann, Femtosecond, picosecond and nanosecond laser ablation of solids, Appl. Phys. A, **63** 109-115 (1996).

[33] L. Jiang, H.-L. Tsai, Improved two-temperature model and its application in ultrashort laser heating of metal films, J. Heat Transfer, **127** 1167-1173 (2005).

[34] J. Chen, D. Tzou, J. Beraun, A semiclassical two-temperature model for ultrafast laser heating, Int. J. Heat Mass Transfer, **49** 307-316 (2006).

[35] J. Fujimoto, J. Liu, E. Ippen, N. Bloembergen, Femtosecond laser interaction with metallic tungsten and nonequilibrium electron and lattice temperatures, Phys. Rev. Lett., **53** 1837 (1984).

[36] J. Dickinson, S. Langford, J. Shin, D. Doering, Positive ion emission from excimer laser excited MgO surfaces, Phys. Rev. Lett., **73** 2630 (1994).

[37] B. Rethfeld, K. Sokolowski-Tinten, D. Von der Linde, S. Anisimov, Ultrafast thermal melting of laser-excited solids by homogeneous nucleation, Physical review B, **65** 092103 (2002).

[38] I. Mingareev, *Ultrafast dynamics of melting and ablation at large laser intensities* (Lehrstuhl für Lasertechnik, 2009).

[39] A.I. Kuznetsov, C. Unger, J. Koch, B.N. Chichkov, Laser-induced jet formation and droplet ejection from thin metal films, Appl. Phys. A, **106** 479-487 (2012).

[40] D. Perez, L.J. Lewis, Ablation of solids under femtosecond laser pulses, Phys. Rev. Lett., **89** 255504 (2002).

[41] D. Perez, L.J. Lewis, Molecular-dynamics study of ablation of solids under femtosecond laser pulses, Physical review B, **67** 184102 (2003).

[42] S. Nolte, C. Momma, H. Jacobs, A. Tünnermann, B. Chichkov, B. Wellegehausen, H. Welling, Ablation of metals by ultrashort laser pulses, JOSA B, **14** 2716-2722 (1997).

[43] Y. Miyasaka, M. Hashida, T. Nishii, S. Inoue, S. Sakabe, Derivation of effective penetration depth of femtosecond laser pulses in metal from ablation rate dependence on laser fluence, incidence angle, and polarization, Appl. Phys. Lett., **106** 013101 (2015).

[44] Y. Huo, T. Jia, D. Feng, S. Zhang, J. Liu, J. Pan, K. Zhou, Z. Sun, Formation of high spatial frequency ripples in stainless steel irradiated by femtosecond laser pulses in water, Laser Phys., **23** 056101 (2013).

[45] C. Mauclair, S. Landon, D. Pietroy, E. Baubeau, R. Stoian, E. Audouard, Ultrafast laser machining of micro grooves on stainless steel with spatially optimized intensity distribution, J. Laser Micro/Nanoeng., **8** 11 (2013).

[46] A.Y. Vorobyev, C. Guo, Direct femtosecond laser surface nano/microstructuring and its applications, Laser Photonics Rev., **7** 385-407 (2013).

[47] R. Le Harzic, D. Breitling, M. Weikert, S. Sommer, C. Föhl, S. Valette, C. Donnet, E. Audouard, F. Dausinger, Pulse width and energy influence on laser micromachining of metals in a range of 100fs to 5ps, Appl. Surf. Sci., **249** 322-331 (2005).

[48] A. Vorobyev, V. Kuzmichev, N. Kokody, P. Kohns, J. Dai, C. Guo, Residual thermal effects in Al following single ns-and fs-laser pulse ablation, Appl. Phys. A, **82** 357-362 (2006).

[49] A. Vorobyev, C. Guo, Direct observation of enhanced residual thermal energy coupling to solids in femtosecond laser ablation, Appl. Phys. Lett., **86** 011916 (2005).

[50] P. Mannion, J. Magee, E. Coyne, G. O'Connor, T. Glynn, The effect of damage accumulation behaviour on ablation thresholds and damage morphology in ultrafast laser micro-machining of common metals in air, Appl. Surf. Sci., **233** 275-287 (2004).

[51] W. Jia, Z. Peng, Z. Wang, X. Ni, C.-y. Wang, The effect of femtosecond laser micromachining on the surface characteristics and subsurface microstructure of amorphous FeCuNbSiB alloy, Appl. Surf. Sci., **253** 1299-1303 (2006).

[52] S. Höhm, M. Rohloff, J. Krüger, J. Bonse, A. Rosenfeld, *Formation of Laser-Induced Periodic Surface Structures (LIPSS) on Dielectrics and Semiconductors upon Double-Femtosecond Laser Pulse Irradiation Sequences*, in: *Progress in Nonlinear Nano-Optics* (Springer, 2015).

[53] R. Buividas, M. Mikutis, S. Juodkazis, Surface and bulk structuring of materials by ripples with long and short laser pulses: Recent advances, Prog. Quantum Electron., **38** 119-156 (2014).

[54] A. Malshe, D. Deshpande, Nano and microscale surface and sub-surface modifications induced in optical materials by femtosecond laser machining, J. Mater. Process. Technol., **149** 585-590 (2004).

[55] B. Wu, M. Zhou, J. Li, X. Ye, G. Li, L. Cai, Superhydrophobic surfaces fabricated by microstructuring of stainless steel using a femtosecond laser, Appl. Surf. Sci., **256** 61-66 (2009).

[56] C. Lin, C. Cheng, K. Ou, Micro/nano-structuring of medical stainless steel using femtosecond laser pulses, Physics Procedia, **39** 661-668 (2012).

[57] E. Stratakis, V. Zorba, M. Barberoglou, C. Fotakis, G. Shafeev, Femtosecond laser writing of nanostructures on bulk Al via its ablation in air and liquids, Appl. Surf. Sci., **255** 5346-5350 (2009).

[58] W. de Rossi, L. Machado, N. Vieira, R. Samad, D-scan measurement of the ablation threshold and incubation parameter of optical materials in the ultrafast regime, Physics Procedia, **39** 642-649 (2012).

[59] J. Liu, Simple technique for measurements of pulsed Gaussian-beam spot sizes, Opt. Lett., **7** 196-198 (1982).

[60] Y. Domankevitz, N.S. Nishioka, Measurement of laser ablation threshold with a high-speed framing camera, IEEE J. Quantum Electron., **26** 2276-2278 (1990).

[61] W. Hu, Y.C. Shin, G. King, Modeling of multi-burst mode pico-second laser ablation for improved material removal rate, Appl. Phys. A, **98** 407-415 (2010).

[62] Y. Jee, M.F. Becker, R.M. Walser, Laser-induced damage on single-crystal metal surfaces, JOSA B, **5** 648-659 (1988).

[63] S. Youn, M. Takahashi, H. Goto, R. Maeda, Microstructuring of glassy carbon mold for glass embossing–Comparison of focused ion beam, nano/femtosecond-pulsed laser and mechanical machining, Microelectron. Eng., **83** 2482-2492 (2006).

[64] M. Kuhnke, T. Lippert, E. Ortelli, G. Scherer, A. Wokaun, Microstructuring of glassy carbon: comparison of laser machining and reactive ion etching, Thin Sol. Films, **453** 36-41 (2004).

[65] K. Ho, S. Newman, State of the art electrical discharge machining (EDM), Int. J. Mach. Tools Manuf, **43** 1287-1300 (2003).

[66] G.E. Totten, L. Xie, K. Funatani, *Handbook of mechanical alloy design* (CRC Press, 2003).

[67] E. Leveugle, D. Ivanov, L. Zhigilei, Photomechanical spallation of molecular and metal targets: molecular dynamics study, Appl. Phys. A, **79** 1643-1655 (2004).

[68] R. Le Harzic, N. Huot, E. Audouard, C. Jonin, P. Laporte, S. Valette, A. Fraczkiewicz, R. Fortunier, Comparison of heat-affected zones due to nanosecond and femtosecond laser pulses using transmission electronic microscopy, Appl. Phys. Lett., **80** 3886-3888 (2002).

[69] C. Chien, M. Gupta, Pulse width effect in ultrafast laser processing of materials, Appl. Phys. A, **81** 1257-1263 (2005).

[70] D.E. Rivas, M. Weidman, B. Bergues, A. Muschet, A. Guggenmos, O. Razskazovskaya, H. Schröder, W. Helml, G. Marcus, R. Kienberger, *Generation of high-energy isolated attosecond pulses for XUV-pump/XUV-probe experiments at 100 eV*, High Intensity Lasers and High Field Phenomena (HILAS2016), March 20–22, 2016, Long Beach, United States.

[71] B.C. Stuart, M.D. Feit, S. Herman, A. Rubenchik, B. Shore, M. Perry, Nanosecond-to-femtosecond laser-induced breakdown in dielectrics, Physical Review B, **53** 1749 (1996).

[72] O.A. Hurricane, D.A. Callahan, D.T. Casey, P.M. Celliers, C. Cerjan, E.L. Dewald, T.R. Dittrich, T. Doppner, D.E. Hinkel, L.F.B. Hopkins, J.L. Kline, S. Le Pape, T. Ma, A.G. MacPhee, J.L. Milovich, A. Pak, H.S. Park, P.K. Patel, B.A. Remington, J.D. Salmonson, P.T. Springer, R. Tommasini, Fuel gain exceeding unity in an inertially confined fusion implosion, Nature, **506** 343-348 (2014).

[73] R. Le Harzic, D. Breitling, M. Weikert, S. Sommer, C. Föhl, F. Dausinger, S. Valette, C. Donnet, E. Audouard, Ablation comparison with low and high energy densities for Cu and Al with ultra-short laser pulses, Appl. Phys. A, **80** 1589-1593 (2005).

[74] Y. Hirayama, M. Obara, Heat effects of metals ablated with femtosecond laser pulses, Appl. Surf. Sci., **197** 741-745 (2002).

[75] A. Ancona, F. Röser, K. Rademaker, J. Limpert, S. Nolte, A. Tünnermann, High speed laser drilling of metals using a high repetition rate, high average power ultrafast fiber CPA system, Opt. Express, **16** 8958-8968 (2008).

[76] J. König, S. Nolte, A. Tünnermann, Plasma evolution during metal ablation with ultrashort laser pulses, Opt. Express, **13** 10597-10607 (2005).

[77] K. Venkatakrishnan, B. Tan, P. Stanley, N. Sivakumar, The effect of polarization on ultrashort pulsed laser ablation of thin metal films, J. Appl. Phys., **92** 1604-1607 (2002).

[78] A. Borowiec, H. Tiedje, H. Haugen, Wavelength dependence of the single pulse femtosecond laser ablation threshold of indium phosphide in the 400–2050nm range, Appl. Surf. Sci., **243** 129-137 (2005).

[79] M. Eyett, D. Bäuerle, Influence of the beam spot size on ablation rates in pulsed-laser processing, Appl. Phys. Lett., **51** 2054-2055 (1987).

[80] J.R. Vázquez de Aldana, P. Moreno, L. Roso, Ultrafast lasers: A new frontier for optical materials processing, Opt. Mater., **34** 572-578 (2012).

[81] X. Liu, D. Du, G. Mourou, Laser ablation and micromachining with ultrashort laser pulses, IEEE J. Quantum Electron., **33** 1706-1716 (1997).

[82] K. Furusawa, K. Takahashi, H. Kumagai, K. Midorikawa, M. Obara, Ablation characteristics of Au, Ag, and Cu metals using a femtosecond Ti: sapphire laser, Appl. Phys. A, **69** S359-S366 (1999).

[83] H. Varel, D. Ashkenasi, A. Rosenfeld, M. Wähmer, E. Campbell, Micromachining of quartz with ultrashort laser pulses, Applied Physics A: Materials Science & Processing, **65** 367-373 (1997).

[84] D. Bruneel, G. Matras, R. Le Harzic, N. Huot, K. König, E. Audouard, Micromachining of metals with ultra-short ti-sapphire lasers: Prediction and optimization of the processing time, Opt. Lasers Eng., **48** 268-271 (2010).

[85] J.-P. Colombier, P. Combis, F. Bonneau, R. Le Harzic, E. Audouard, Hydrodynamic simulations of metal ablation by femtosecond laser irradiation, Physical review B, **71** 165406 (2005).

[86] F. Bauer, A. Michalowski, T. Kiedrowski, S. Nolte, Heat accumulation in ultra-short pulsed scanning laser ablation of metals, Opt. Express, **23** 1035-1043 (2015).

[87] P.R. Herman, A. Oettl, K.P. Chen, R.S. Marjoribanks, Laser micromachining of transparent fused silica with 1-ps pulses and pulse trains, Proc. of Optoelectronics' 99-Integrated Optoelectronic Devices (1999).

[88] G. Račiukaitis, M. Brikas, P. Gečys, B. Voisiat, M. Gedvilas, Use of high repetition rate and high power lasers in microfabrication: How to keep the efficiency high?, J. Laser Micro Nanoen., **4** 186-191 (2009).

[89] R. Knappe, H. Haloui, A. Seifert, A. Weis, A. Nebel, *Scaling ablation rates for picosecond lasers using burst micromachining*, Laser Source Technologies and Industrial Lasers and Applications Conference, part of SPIE Photonics West 2010 (SPIE LASE2010), January. 23 - 28, 2010, San Francisco, California, USA.

[90] B. Neuenschwander, T. Kramer, B. Lauer, B. Jaeggi, *Burst mode with ps-and fs-pulses: Influence on the removal rate, surface quality, and heat accumulation*, Laser Source Technologies and Industrial Lasers and Applications Conference, part of SPIE Photonics West 2015 (SPIE LASE2015), February 10–12, 2015, San Francisco, California, USA.

[91] R.L. Harzic, H. Schuck, R. Buckle, T. Anhur, F. Bauerfeld, D. Sauer, *Influence of laser parameters for micro and sub-um processing by short and ultrashort laser pulses*, in: E. Beyer, F. Dausinger, A. Ostendorf, A. Otto (Eds.) *Proceedings of Lasers in Manufacturing 2005* (AT-Verlag Stuttgart, 2005).

[92] B. Neuenschwander, B. Jaeggi, M. Schmid, From fs to sub-ns: Dependence of the material removal rate on the pulse duration for metals, Physics Procedia, **41** 794-801 (2013).

[93] J. Franks, *Market demands for ultra short pulse laser micromachining*, 17th International Symposium on Laser Precision Microfabrication (LPM2016), May 23-27, 2016, Xi'an, China.

[94] A. Borowiec, H. Haugen, Femtosecond laser micromachining of grooves in indium phosphide, Appl. Phys. A, **79** 521-529 (2004).

[95] J. Bonse, A. Rosenfeld, J. Krüger, On the role of surface plasmon polaritons in the formation of laser-induced periodic surface structures upon irradiation of silicon by femtosecond-laser pulses, J. Appl. Phys., **106** 104910 (2009).

[96] H. Tönshoff, C. Momma, A. Ostendorf, S. Nolte, G. Kamlage, Microdrilling of metals with ultrashort laser pulses, Journal of Laser Applications, **12** 23-27 (2000).

[97] M. Kraus, M.A. Ahmed, A. Michalowski, A. Voss, R. Weber, T. Graf, Microdrilling in steel using ultrashort pulsed laser beams with radial and azimuthal polarization, Opt. Express, **18** 22305-22313 (2010).

[98] A. Ostendorf, C. Kulik, T. Bauer, N. Baersch, *Ablation of metals and semiconductors with ultrashort pulsed lasers: improving surface qualities of microcuts and grooves*, Laser Source Technologies and Industrial Lasers and Applications Conference, part of SPIE Photonics West 2004 (SPIE LASE2004), January 24–29, 2004, San Jose, California, USA.

[99] A. Löbe, J. Vrenegor, R. Fleige, V. Sturm, R. Noll, Laser-induced ablation of a steel sample in different ambient gases by use of collinear multiple laser pulses, Anal. Bioanal.Chem., **385** 326-332 (2006).

[100] S. Amoruso, R. Bruzzese, X. Wang, J. Xia, Propagation of a femtosecond pulsed laser ablation plume into a background atmosphere, Appl. Phys. Lett., **92** 041503 (2008).

[101] A. Pereira, A. Cros, P. Delaporte, S. Georgiou, A. Manousaki, W. Marine, M. Sentis, Surface nanostructuring of metals by laser irradiation: effects of pulse duration, wavelength and gas atmosphere, Appl. Phys. A, **79** 1433-1437 (2004).

[102] C. Boulmer-Leborgne, R. Benzerga, J. Perriere, *Nanoparticle formation by femtosecond laser ablation*, in: *Laser-Surface Interactions for New Materials Production* (Springer, 2010).

[103] P. Wagener, S. Ibrahimkutty, A. Menzel, A. Plech, S. Barcikowski, Dynamics of silver nanoparticle formation and agglomeration inside the cavitation bubble after pulsed laser ablation in liquid, PCCP, **15** 3068-3074 (2013).

[104] O. Albert, S. Roger, Y. Glinec, J. Loulergue, J. Etchepare, C. Boulmer-Leborgne, J. Perrière, E. Millon, Time-resolved spectroscopy measurements of a titanium plasma induced by nanosecond and femtosecond lasers, Appl. Phys. A, **76** 319-323 (2003).

[105] R. Stoian, D. Ashkenasi, A. Rosenfeld, E. Campbell, Coulomb explosion in ultrashort pulsed laser ablation of Al 2 O 3, Physical Review B, **62** 13167 (2000).

[106] R. Stoian, A. Rosenfeld, D. Ashkenasi, I. Hertel, N. Bulgakova, E. Campbell, Surface charging and impulsive ion ejection during ultrashort pulsed laser ablation, Phys. Rev. Lett., **88** 097603 (2002).

[107] S. Amoruso, X. Wang, C. Altucci, C. De Lisio, M. Armenante, R. Bruzzese, N. Spinelli, R. Velotta, Double-peak distribution of electron and ion emission profile during femtosecond laser ablation of metals, Appl. Surf. Sci., **186** 358-363 (2002).

[108] S. Amoruso, R. Bruzzese, N. Spinelli, R. Velotta, M. Vitiello, X. Wang, G. Ausanio, V. Iannotti, L. Lanotte, Generation of silicon nanoparticles via femtosecond laser ablation in vacuum, Appl. Phys. Lett., **84** 4502-4504 (2004).

[109] T. Glover, G. Ackerman, A. Belkacem, P. Heimann, Z. Hussain, R. Lee, H. Padmore, C. Ray, R. Schoenlein, W. Steele, Metal-insulator transitions in an expanding metallic fluid: particle formation kinetics, Phys. Rev. Lett., **90** 236102 (2003).

[110] L. Zhigilei, Dynamics of the plume formation and parameters of the ejected clusters in short-pulse laser ablation, Appl. Phys. A, **76** 339-350 (2003).

[111] S. Barcikowski, J. Walter, A. Hahn, J. Koch, H. Haloui, T. Herrmann, A. Gatti, Picosecond and femtosecond laser machining may cause health risks related to nanoparticle emission, J. Laser Micro/Nanoeng., **4** 159-164 (2009).

[112] Z. Wu, H. Jiang, Q. Sun, H. Guo, H. Yang, Q. Gong, Micro-ablation at the front and rear surfaces of a fused silica window by using a femtosecond laser pulse in air, J. Opt. A: Pure Appl. Opt., **6** 671 (2004).

[113] J. Cheng, W. Perrie, S. Edwardson, E. Fearon, G. Dearden, K. Watkins, Effects of laser operating parameters on metals micromachining with ultrafast lasers, Appl. Surf. Sci., **256** 1514-1520 (2009).

[114] J. Lopez, C. Loumena, Y. Zaouter, E. Mottay, Micromachining of metal and silicon using high average power ultrafast fiber laser, Proc. of LPM2010-the 11th International Symposium on Laser Precision Microfabrication (2010).

[115] A. Kruusing, Underwater and water-assisted laser processing: Part 2—Etching, cutting and rarely used methods, Opt. Lasers Eng., **41** 329-352 (2004).

[116] A. Kruusing, Underwater and water-assisted laser processing: Part 1—general features, steam cleaning and shock processing, Opt. Lasers Eng., **41** 307-327 (2004).

[117] Y. Sano, N. Mukai, K. Okazaki, M. Obata, Residual stress improvement in metal surface by underwater laser irradiation, Nucl. Instrum. Methods Phys. Res., Sect. B, **121** 432-436 (1997).

[118] S. Zhu, Y. Lu, M. Hong, Laser ablation of solid substrates in a water-confined environment, Appl. Phys. Lett., **79** 1396-1398 (2001).

[119] A. Dupont, P. Caminat, P. Bournot, J. Gauchon, Enhancement of material ablation using 248, 308, 532, 1064 nm laser pulse with a water film on the treated surface, J. Appl. Phys., **78** 2022-2028 (1995).

[120] S. Koichi, N. Tetsutaro, S. Wafaa, T. Noriharu, Effect of Pressurization on the Dynamics of a Cavitation Bubble Induced by Liquid-Phase Laser Ablation, Applied Physics Express, **2** 046501 (2009).

[121] K. Sasaki, N. Takada, Liquid-phase laser ablation, Pure Appl. Chem., **82** 1317-1327 (2010).

[122] T. Tsuji, Y. Okazaki, Y. Tsuboi, M. Tsuji, Nanosecond time-resolved observations of laser ablation of silver in water, Japanese journal of applied physics, **46** 1533 (2007).

161

[123] B. Acherjee, S. Prakash, A.S. Kuar, S. Mitra, Grey relational analysis based optimization of underwater Nd: YAG laser micro-channeling on PMMA, Procedia Engineering, **97** 1406-1415 (2014).

[124] Y. Yan, L. Li, K. Sezer, W. Wang, D. Whitehead, L. Ji, Y. Bao, Y. Jiang, CO2 laser underwater machining of deep cavities in alumina, J. Eur. Ceram. Soc., **31** 2793-2807 (2011).

[125] M. Silvennoinen, J.J.J. Kaakkunen, K. Paivasaari, P. Vahimaa, Water spray assisted ultrashort laser pulse ablation, Appl. Surf. Sci., **265** 865-869 (2013).

[126] A. Couairon, E. Gaižauskas, D. Faccio, A. Dubietis, P. Di Trapani, Nonlinear X-wave formation by femtosecond filamentation in Kerr media, Physical Review E, **73** 016608 (2006).

[127] A. Jarnac, G. Tamosauskas, D. Majus, A. Houard, A. Mysyrowicz, A. Couairon, A. Dubietis, Whole life cycle of femtosecond ultraviolet filaments in water, Physical Review A, **89** 033809 (2014).

[128] S. Minardi, C. Milián, D. Majus, A. Gopal, G. Tamošauskas, A. Couairon, T. Pertsch, A. Dubietis, Energy deposition dynamics of femtosecond pulses in water, Appl. Phys. Lett., **105** 224104 (2014).

[129] S. Chin, F. Théberge, W. Liu, Filamentation nonlinear optics, Appl. Phys. B, **86** 477-483 (2007).

[130] R.W. Boyd, S.G. Lukishova, Y.R. Shen, *Self-focusing: Past and Present: Fundamentals and Prospects* (Springer Science & Business Media, 2008).

[131] R. Ackermann, K. Stelmaszczyk, P. Rohwetter, G. Méjean, E. Salmon, J. Yu, J. Kasparian, G. Méchain, V. Bergmann, S. Schaper, Triggering and guiding of megavolt discharges by laser-induced filaments under rain conditions, Appl. Phys. Lett., **85** 5781-5783 (2004).

[132] C. Amico, A. Houard, S. Akturk, Y. Liu, J. Le Bloas, M. Franco, B. Prade, A. Couairon, V. Tikhonchuk, A. Mysyrowicz, Forward THz radiation emission by femtosecond filamentation in gases: theory and experiment, New J. Phys., **10** 013015 (2008).

[133] W. Watanabe, T. Tamaki, Y. Ozeki, K. Itoh, *Filamentation in ultrafast laser material processing*, in: *Progress in Ultrafast Intense Laser Science VI* (Springer, 2010).

[134] S. Butkus, D. Paipulas, R. Sirutkaitis, E. Gaižauskas, V. Sirutkaitis, Rapid Cutting and Drilling of Transparent Materials via Femtosecond Laser Filamentation, Proc LAMP, **12** (2013).

[135] S. Butkus, E. Gaižauskas, D. Paipulas, Ž. Viburys, D. Kaškelyė, M. Barkauskas, A. Alesenkov, V. Sirutkaitis, Rapid microfabrication of transparent materials using filamented femtosecond laser pulses, Appl. Phys. A, **114** 81-90 (2014).

[136] G. Yang, *Laser ablation in liquids: principles and applications in the preparation of nanomaterials* (CRC Press, 2012).

[137] A.V. Kabashin, M. Meunier, Synthesis of colloidal nanoparticles during femtosecond laser ablation of gold in water, J. Appl. Phys., **94** 7941-7943 (2003).

[138] S. Barcikowski, A. Hahn, A. Kabashin, B. Chichkov, Properties of nanoparticles generated during femtosecond laser machining in air and water, Appl. Phys. A, **87** 47-55 (2007).

[139] S. Besner, A.V. Kabashin, M. Meunier, Two-step femtosecond laser ablation-based method for the synthesis of stable and ultra-pure gold nanoparticles in water, Appl. Phys. A, **88** 269-272 (2007).

[140] N. Bärsch, J. Jakobi, S. Weiler, S. Barcikowski, Pure colloidal metal and ceramic nanoparticles from high-power picosecond laser ablation in water and acetone, Nanotechnology, **20** 445603 (2009).

[141] S.Z. Khan, Y. Yuan, A. Abdolvand, M. Schmidt, P. Crouse, L. Li, Z. Liu, M. Sharp, K. Watkins, Generation and characterization of NiO nanoparticles by continuous wave fiber laser ablation in liquid, J. Nanopart. Res., **11** 1421-1427 (2009).

[142] F. Hajiesmaeilbaigi, A. Mohammadalipour, J. Sabbaghzadeh, S. Hoseinkhani, H. Fallah, Preparation of silver nanoparticles by laser ablation and fragmentation in pure water, Laser Phys. Lett., **3** 252 (2005).

[143] X. Zhu, T. Suzuki, T. Nakayama, H. Suematsu, W. Jiang, K. Niihara, Underwater laser ablation approach to fabricating monodisperse metallic nanoparticles, Chem. Phys. Lett., **427** 127-131 (2006).

[144] D. Shindo, T. Oikawa, *Energy Dispersive X-ray Spectroscopy*, in: *Analytical Electron Microscopy for Materials Science* (Springer, 2002).

[145] R. Van Grieken, A. Markowicz, *Handbook of X-ray Spectrometry* (CRC Press, 2001).

[146] D. Wollman, K.D. Irwin, G.C. Hilton, L. Dulcie, D.E. Newbury, J.M. Martinis, High-resolution energy-dispersive microcalorimeter spectrometer for X-ray microanalysis, Journal of Microscopy, **188** 196-223 (1997).

[147] U. Kramar, Advances in energy-dispersive X-ray fluorescence, J. Geochem. Explor., **58** 73-80 (1997).

[148] L.J. Allen, A.J. D'Alfonso, B. Freitag, D.O. Klenov, Chemical mapping at atomic resolution using energy-dispersive x-ray spectroscopy, MRS Bull., **37** 47-52 (2012).

[149] J.C. Russ, *Fundamentals of Energy Dispersive X-Ray Analysis: Butterworths Monographs in Materials* (Butterworth-Heinemann, 2013).

[150] "PHAROS" femtosecond laser, manufacturer datasheet. Online access: http://lightcon.com/upload/Product%20Catalogue%202015%20new.pdf (last accessed 2016.03.01).

[151] Femtosecond OPO, OPA and lasers supplier. UAB MGF "Šviesos konversija" (known as Light Conversion on international market) Online access: www.lightcon.com (last accessed 2014.05.10).

[152] "HIRO" laser harmonics generator, manufacturer datasheet. Online access: http://lightcon.com/upload/iblock/0b9/0b91a0cd98804455a2928acd96910ca1.pdf (last accessed 2015.05.06).

[153] Positioning solution and motion control development supplier. Aerotech, Inc., USA. Online access: https://www.aerotech.com/ (last accessed 2016.05.20).

[154] ALS130 direct-drive linear motor stage with crossed-roller mechanical bearings, noncontact linear encoder and 0.1 μm bi-directional repeatability. Supplier specification. Online access: https://www.aerotech.com/media/115408/als130.pdf (last accessed 2014.06.25).

[155] ANT-4V Vertical Translation direct drive positioning stage. Supplier specification. Online access: https://www.aerotech.com/media/117244/ant4v.pdf (last accessed 2013.05.26).

[156] Laser Micromachining Software SCA. User manual. Online access: http://wophotonics.com/wp-content/uploads/2015/10/SCA-v.-2.5.25-manual.pdf (last accessed 2015.02.02).

[157] Laser micromachining solutions supplier. Workshop of Photonics, Lithuania. Online access: http://wophotonics.com/ (last accessed 2012.02.05).

[158] MATRICAN. Online access: http://www.matrican.es/en (last accessed 2016.05.15).

[159] Müggler Engineering ApS. Online access: http://mueggler.dk/ (last accessed 2015.05.15).

[160] Sverker 21, No. 1.2379. Manufacturer datasheet. Online access: http://www.uddeholm.com/files/PB_Uddeholm_sverker_21_english.pdf (last accessed 2016.02.05).

[161] EN AW-5083 aluminium alloy. Manufacturer datasheet. Online access: http://gleich.de/en/products/aluminium-rolled-plates/al-rolled-plates-en-aw/en-aw-5083?pdf (last accessed 2016.05.09).

[162] C.-W. Cheng, X.-Z. Tsai, J.-S. Chen, Micromachining of stainless steel with controllable ablation depth using femtosecond laser pulses, Int. J. of Adv. Man. Techn., 1-8 (2016).

[163] J. Krüger, P. Meja, M. Autric, W. Kautek, Femtosecond pulse laser ablation of anodic oxide coatings on aluminium alloys with on-line acoustic observation, Appl. Surf. Sci., **186** 374-380 (2002).

[164] Galvanometer beam tilting system supplier. Scanlab AG. Online access: http://www.scanlab.de/ (last accessed 2015.02.09).

[165] Intelliscan 10 galvanometer scanner supplier specification. Online access: http://www.scanlab.de/sites/default/files/PDF-Dateien/Produktblaetter/Scan-Systeme/intelliSCAN%2BintelliSCANde_DE_0.pdf (last accessed 2015.05.30).

[166] Synchronous, real-time controlling electronics in form of PCIe slot card for scan systems and lasers. RTC 4. Online access: http://www.scanlab.de/sites/default/files/PDF-Dateien/Data-Sheets/RTC-4-control-boards-SCANLAB-EN.pdf (last accessed 2013.12.31).

[167] Ophir SP620U CCD camera datasheet. Online access: http://www.ophiropt.com/laser--measurement/sites/default/files/SP503U-SP620U.pdf (last accessed 2016.05.06).

[168] Brochure for the BX51 Microscope - Olympus Micro. Online access: http://www.olympusmicro.com/brochures/pdfs/bx51.pdf (last accessed 2015.05.09).

[169] Sensofar profilometer manufacturer webpage. Online access: http://www.sensofar.com/ (last accessed 2015.06.03).

[170] W. Wang, X. Mei, G. Jiang, S. Lei, C. Yang, Effect of two typical focus positions on microstructure shape and morphology in femtosecond laser multi-pulse ablation of metals, Appl. Surf. Sci., **255** 2303-2311 (2008).

[171] Beam shapers manufacturer, TOPAG, GmbH. Online access: http://www.topag.de/en/laser-beam-shapers-en/top-hat-en/rectangular-smaller-than-100-me-n.html?sid=332:FBS-rectangular-smaller-than-100%C2%B5m- (last accessed 2015.10.10).

[172] G. Račiukaitis, E. Stankevičius, P. Gečys, M. Gedvilas, C. Bischoff, E. Jaeger, U. Umhofer, F. Voelklein, Laser Processing by Using Diffractive Optical Laser Beam Shaping, JLMN-Journal of Laser Micro/Nanoengineering, **6** (2011).

[173] Z. Ou, M. Huang, F. Zhao, The fluence threshold of femtosecond laser blackening of metals: The effect of laser-induced ripples, Opt. Laser Technol., **79** 79-87 (2016).

[174] H. Huang, L.-M. Yang, S. Bai, J. Liu, Blackening of metals using femtosecond fiber laser, Appl. Opt., **54** 324-333 (2015).

[175] J. Liu, *Method and apparatus for high speed surface blackening and coloring with ultrafast fiber lasers*, in: (Google Patents, 2015).

[176] A.Y. Vorobyev, C. Guo, Metallic light absorbers produced by femtosecond laser pulses, Advances in Mechanical Engineering, **2** 452749 (2010).

[177] M. Malinauskas, S. Rekštytė, L. Lukoševičius, S. Butkus, E. Balčiūnas, M. Pečiukaitytė, D. Baltriukienė, V. Bukelskienė, A. Butkevičius, P. Kucevičius, V. Rutkūnas, S. Juodkazis, 3D Microporous Scaffolds Manufactured via Combination of Fused Filament Fabrication and Direct Laser Writing Ablation, Micromachines, **5** 839-858 (2014).

[178] P.T. Mannion, J. Magee, E. Coyne, G.M. O'Connor, T.J. Glynn, The effect of damage accumulation behaviour on ablation thresholds and damage morphology in ultrafast laser micro-machining of common metals in air, Appl. Surf. Sci., **233** 275-287 (2004).

[179] A. Urniežius, N. Šiaulys, V. Kudriašov, V. Sirutkaitis, A. Melninkaitis, Application of time-resolved digital holographic microscopy in studies of early femtosecond laser ablation, Appl. Phys. A, **108** 343-349 (2012).

[180] K. Kuršelis, T. Kudrius, D. Paipulas, O. Balachninaitė, V. Sirutkaitis, Experimental study on femtosecond laser micromachining of grooves in stainless steel, Lith. J. Phys., **50** (2010).

[181] S. Butkus, A. Alesenkov, D. Paipulas, E. Gaižauskas, A. Melninkaitis, D. Kaškelytė, M. Barkauskas, V. Sirutkaitis, Analysis of the Micromachining Process of Dielectric and Metallic Substrates Immersed in Water with Femtosecond Pulses, Micromachines, **6** 2010-2022 (2015).

[182] S. Butkus, A. Alesenkov, D. Paipulas, D. Kaškelyė, V. Sirutkaitis, *Micromachining of transparent, semiconducting and metal substrates using femtosecond laser beams*, The 7th International Congress on Laser Advanced Materials Processing (LAMP2015), May 26 – 29, 2015, Kitakyushu, Fukuoka, Japan.

[183] E. Gaižauskas, A. Dubietis, V. Kudriašov, V. Sirutkaitis, A. Couairon, D. Faccio, P. Di Trapani, *On the role of conical waves in self-focusing and filamentation of femtosecond pulses with nonlinear losses*, in: *Self-focusing: Past and Present* (Springer, 2009).

[184] L. Keldysh, Ionization in the field of a strong electromagnetic wave, Sov. Phys. JETP, **20** 1307-1314 (1965).

[185] V. Sirutkaitis, V. Kudriasov, E. Gaizauskas, Beam transformation and permanent modification in fused silica induced by femtosecond filaments, Journal of the Optical Society of America B, Optical physic, 2619-2627 (2005).

[186] D. Majus, V. Jukna, G. Valiulis, A. Dubietis, Generation of periodic filament arrays by self-focusing of highly elliptical ultrashort pulsed laser beams, Physical Review A, **79** 033843 (2009).

[187] D.C. Montgomery, *Design and analysis of experiments* (John Wiley & Sons, 2008).

[188] R. Pannerselvam, *Design and analysis of experiments* (PHI Learning Pvt. Ltd., 2012).

[189] S.R. Schmidt, R.G. Launsby, *Understanding industrial designed experiments* (Air Academy Press, 1989).

[190] Interactive statistical discovery software, JMP. Online access: http://www.jmp.com/en_us/home.html (last accessed 2016.05.01).

[191] P. Maine, D. Strickland, P. Bado, M. Pessot, G. Mourou, Generation of ultrahigh peak power pulses by chirped pulse amplification, Quantum Electronics, IEEE Journal of, **24** 398-403 (1988).

[192] R. Brinkmann, C. Hansen, D. Mohrenstecher, M. Scheu, R. Birngruber, Analysis of cavitation dynamics during pulsed laser tissue ablation by optical on-line monitoring, Selected Topics in Quantum Electronics, IEEE Journal of, **2** 826-835 (1996).

[193] C. Young, Y.-D. Kim, K.-H. Kang, Ablation drilling of invar alloy using ultrashort pulsed laser, Int. J. Precis. Eng. Manuf., **10** 11-16 (2011).

[194] G. Dumitru, V. Romano, H. Weber, M. Sentis, J. Hermann, S. Bruneau, W. Marine, H. Haefke, Y. Gerbig, Metallographical analysis of steel and hard metal substrates after deep-drilling with femtosecond laser pulses, Appl. Surf. Sci., **208** 181-188 (2003).

[195] S. Valette, P. Steyer, L. Richard, B. Forest, C. Donnet, E. Audouard, Influence of femtosecond laser marking on the corrosion resistance of stainless steels, Appl. Surf. Sci., **252** 4696-4701 (2006).

Appendix 1

Prediction expression for the model described in the subchapter 5.6 (Influence of the laser pulse duration on the cutting speed of steel):

t(s) = 1 / (3.977·10^2 + 2.5446·10^{-5}·v - 1.493·10^{-6}·t - 5.655·10^{-8}·v_n·v_n - 8.173·10^{-3}·f_n·f_n + 1.0879·10^{-9}·v_n·f_n·t_n + 5.408·10^{-11}·t_n·t_n - 7.61·10^{-10}·v_n·t_n - 2.036·10^{-7}·f_n·t_n - 1.02·10^{-3}·f);

where $v_n = v - 520$; $f_n = f + 6.061·10^{-2}$; $t_n = t - 8.401·10^3$
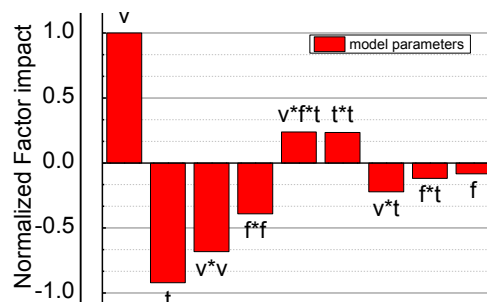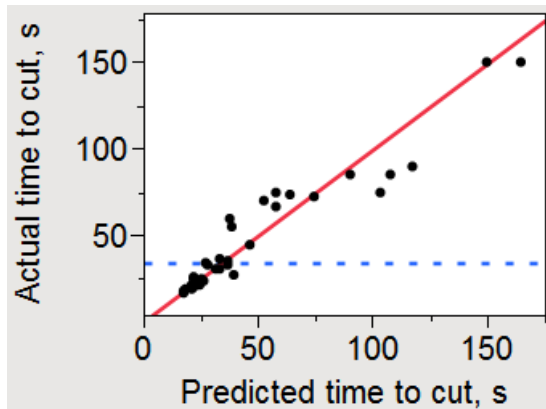
Actual by predicted plot showing the accuracy of the fitted model.

Normalized model parameters impact on the time to cut.